Observer Design for Non-Monotonic Nonlinear Systems and Interesting Contemporary Applications

A DISSERTATION
SUBMITTED TO THE FACULTY OF THE
UNIVERSITY OF MINNESOTA
BY

Hamidreza Movahedi

IN PARTIAL FULFILLMENT OF THE REQUIREMENTS
FOR THE DEGREE OF
DOCTOR OF PHILOSOPHY

Professor Rajesh Rajamani

August 2022

Acknowledgements

Above all, I would like to thank my advisor Prof. Rajesh Rajamani for his continuous support and guidance through the labyrinthine path of PhD studies. Beside innumerate hours of helpful and supportive discussions, his unparalleled dedication to research is the most important trait that I learned from him and aspire to imitate.

I am also grateful to Prof. Anna Stefanopoulou, Prof. Huazhen Fang, Dr. Jason Siegel, Dr. Ning Tian, and Dr. Miriam Figueroa-Santos for their collaborations in parts of this dissertation

My further gratitude goes to my past and current lab-mates: Dr. Ryan Madson, Dr. Ye Zhang, Dr. Woongsun Jeon, Dr. Corey Cruttenden, Dr. Mehdi Ahmadi, Dr. Gregg Johnson, Dr. Heng Wang, Dr. Yan Wang, Dr. Song Zhang, Zhenming Xie, Hamidreza Alai, Navaneeth Pushpalayam, and Ali Nouriani for the academic and non-academic experiences we shared.

Finally, I would like to thank my family for their support and love. I would like to thank my parents for their effort in accomplishing the arduous task of raising me as well as possible, and my little sister Matin who was a great support during turbulent times.

Abstract

This dissertation analyzes observer design for non-monotonic nonlinear systems and develops globally stable observer design techniques for such systems. Non-monotonic nonlinear systems are frequently encountered in many practical applications, including vehicle tracking, magnetic position estimation, robotics, state of charge (SoC) estimation in Li-ion batteries, and infectious disease spread dynamics. Very few papers in literature have recognized the special challenge that non-monotonic systems pose to the existing nonlinear observer design methods. This dissertation demonstrates that current LMI-based observer design methods often do not have feasible solutions for many non-monotonic systems. This motivates the need for new observer design techniques. Such techniques are used in three major applications in this thesis: state of charge estimation in Li-ion batteries, magnetic position estimation, and estimation in infectious disease spread dynamics.

First, a class of systems in which the process dynamics and output equations contain nonlinear functions of only scalar arguments are considered. A Lyapunov approach is utilized to develop an LMI-based observer design method for this class of nonlinear systems. Then, the failure of LMI-based methods to provide constant observer gains for non-monotonic systems is rigorously analyzed, and it is demonstrated that, no matter how small the Lipschitz constant or the Jacobian bounds of the involved nonlinear functions, these methods cannot provide a stabilizing constant observer gain if all the functions of the system are non-monotonic. Based on this theoretical result, a technique to extend the design method to include switched gain observers is presented and its global asymptotic stability is rigorously proven.

The developed observer design methodology is utilized to estimate the SoC in a lithium-ion battery, using measurements of terminal voltage and bulk force. The challenge in this application is that the bulk force applied to the casing of the battery, as a result of Lithium-ion intercalation and deintercalation, is a non-monotonic function of the SoC. Hence, a switched gain observer is devised and applied. Using detailed simulations of possible mismatches in the battery model, the robustness of the observer is compared with that of the extended Kalman filter, and the observer is shown to be less susceptible to these

model errors. Experimental results corroborate this finding.

Position estimation in electro-hydraulic actuators using non-contacting magnetic sensors is another subject that is considered. Magnetic measurements in this application are all non-monotonic, hence based on the theoretical findings of this dissertation it is clear that more than one magnetic sensor is needed for this estimation problem. Subsequently, the minimum singular values of the observability matrix are utilized as a metric for minimizing the number of sensors and optimizing sensor locations. Extensive experimental results are provided to demonstrate the optimality of the sensor locations and the accuracy of the switched gain observer designed for this application.

Next, the hysteresis in Li-ion batteries is analyzed. A nonlinear double capacitor model is used for this problem that contains a measurement equation with two nonlinear functions, one of them being significant hysteresis in voltage of the battery as a function of the SoC. Previously, researchers in this field used a differential equation to model the hysteresis. In this dissertation, it is shown that this popular method loses observability and a modified Preisach method is suggested as an alternative. Then a nonlinear Lipschitz observer is designed for this application, and it is shown that the observer provides accurate SoC estimates based on experimental data in the presence of hysteresis.

Another research application explored in this dissertation is centered around infectious disease spread dynamics and the real-time estimation problem of variables characterizing disease spread. The COVID-19 epidemic is studied for this purpose, and a new nonlinear dynamic model is developed to enhance the traditional SEIR epidemic model to include additional variables. Subsequently, a cascaded observer is developed to estimate the real-time values of the infection rate and the basic reproduction number of COVID-19 spread in Minnesota.

Finally, the use of the nonlinear observer design techniques for handling sensor noise and process disturbances is considered. A H_∞-based globally stable nonlinear observer design technique is explored to provide design flexibility equivalent to the popular locally stable extended Kalman filter which is based on linearization of plant dynamics. Furthermore, comparing with the performance of the extended and unscented Kalman filters in the presence of non-Gaussian pulse disturbances and through detailed simulations,

it is shown that the H_∞ nonlinear observer performs better and can provide a guaranteed upper bound on the estimation error.

Table of Contents

List of Tables

List of Figures

Citations of Published Work

Portions of this thesis have appeared in the following publications:

Journal Publications:

1) R. Rajamani, W. Jeon, H. Movahedi and A. Zemouche, "On the need for switched-gain observers for non-monotonic nonlinear systems," in *Automatica*, vol 114 , pp. 108814, Apr. 2019,
   DOI: 10.1016/j.automatica.2020.108814.
2) H. Movahedi, MA. Figueroa-Santos, JB. Siegel, AG. Stefanopoulou and R. Rajamani, "Hybrid nonlinear observer for battery state-of-charge estimation using nonmonotonic force measurements," in *Advanced Control for Applications: Engineering and Industrial Systems*, vol 2, no 3, pp. e38, Sep. 2020,
   DOI: doi.org/10.1002/adc2.38.
3) H. Movahedi, N. Tian, H. Fang and R. Rajamani, "Hysteresis compensation and nonlinear observer design for state-of-charge estimation using a nonlinear double-capacitor Li-ion battery model," in *IEEE/ASME Transactions on Mechatronics,* vol. 27, no. 1, pp. 594-604, Feb. 2022,
   DOI: 10.1109/TMECH.2021.3068982.
4) H. Movahedi, A. Zemouche and R. Rajamani, "Magnetic position estimation using optimal sensor placement and nonlinear observer for smart actuators," in *Control Engineering Practice,* vol. 112, pp. 104817, Jul. 2021,
   DOI: 10.1016/j.conengprac.2021.104817.

Conference Publications:

1) H. Movahedi, A. Zemouche and R. Rajamani, "Linear position estimation on smart

actuators using a nonlinear observer," *2019 American Control Conference (ACC)*, 2019, pp. 453-458,
DOI: 10.23919/ACC.2019.8814729.

2) R. Rajamani, W. Jeon, H. Movahedi and A. Zemouche, "Vehicle motion estimation using a switched gain nonlinear observer," *2020 American Control Conference (ACC),* 2020, pp. 3047-3052,
DOI: 10.23919/ACC45564.2020.9147225.

3) H. Movahedi, A. Zemouche and R. Rajamani, "Estimation of the basic reproduction number for the COVID-19 pandemic in Minnesota," *2021 Modeling, Estimation and Control Conference (MECC),* 2021, in *Ifac-papersonline*, vol. 54, no. 20, pp. 251-257,
DOI: 10.1016/j.ifacol.2021.11.183.

4) H. Movahedi, N. Tian, H. Fang and R. Rajamani, "Hysteresis compensation in state-of-charge estimation with a nonlinear double-capacitor Li-ion battery model," *2021 American Control Conference (ACC),* 2021, pp. 3108-3113,
DOI: 10.23919/ACC50511.2021.9482791.

Chapter 1
Introduction

This thesis focuses on the design of state estimation algorithms or "observers" for nonlinear dynamic systems. A new LMI-based observer algorithm for a class of nonlinear systems is developed and its use is demonstrated for three major applications.

Observer design for nonlinear systems continues to be a topic of significant research interest in the control systems community. Two major approaches to nonlinear observer design in the literature include

i) the high gain observer approach [1], and

ii) the LMI-based design approach [2].

The high gain observer approach requires the nonlinear system to be in the "normal" canonical form and typically is utilized only for single-output systems [3]. While this approach guarantees the existence of a stable observer gain, there are challenges associated with transforming any given dynamic system to the normal form. The viability of high-gain observers in output feedback control has been demonstrated [4], and due to the use of large gains, this type of observers can achieve fast convergence [5]. However, using large observer gains can result in some disadvantages. The large gains can cause numerical issues for high dimensional systems [6], result in overshoot or undershoot of the estimation error in transient phases (also known as peaking phenomenon) [7], and generally make the estimation very susceptible to noise and high frequency model uncertainties [6].

The LMI-based observer design approach is more broadly applicable with less requirements on the form of the dynamic system model. However, this approach relies on

finding a feasible solution to a LMI in order to find the observer gain, and there are often no guarantees about the existence of a feasible solution. As will be seen in this thesis, many practical real-world applications encounter a situation where there is no feasible solution to the observer design LMI. Previously, there was no understanding of why the observer design LMI did not have a feasible solution for a particular application, with the blame for infeasibility often being assigned to the Lipschitz constant or the Jacobian bounds of the nonlinear functions being too large.

This thesis sheds a new light on one of the major causes of infeasibility of observer design LMIs. It shows the importance of monotonicity of nonlinear functions for observer design feasibility, and develops an observer design approach to handle non-monotonic nonlinear functions. The developed approach is utilized for three major real-world applications and its performance evaluated extensively using both simulations and experimental data. The three major applications studied in the thesis are:

a) State of charge estimation in Li-ion batteries using new types of sensor measurements and in the presence of significant hystersis in the measurement equation,
b) Position estimation in pneumatic hydraulic actuators using magnetic sensors, and
c) Estimation of infection spread states and parameters for analysis of the COVID-19 pandemic health data .

1.1 LMI-based Observer Design Methods

LMI-based observer design methods have previously been developed for systems with Lipschitz nonlinearities [8, 9], differentiable nonlinear systems with locally bounded Jacobians [10], systems with nonlinearities satisfying an incremental quadratic inequality [11], and for monotonic nonlinear systems [12].

1.1.1 Lipschitz Based Observer Design

One group of the LMI-based design methods assume Lipschitz bounded conditions for

the nonlinearity. Two of these methods are discussed here in order to show the type of LMIs that are used for observer design.

Consider a dynamic system with nonlinear dynamics and a linear output equation represented as

$$\dot{x} = Ax + Bu + f(x) \tag{1.1}$$
$$y = Cx$$

where $x \in \mathbb{R}^n$ is the state vector, $y \in \mathbb{R}^m$ is the measurement of the system and the function $f(x)$ satisfies the Lipschitz condition

$$\|f(x) - f(\hat{x})\|_2 \leq \gamma \|x - \hat{x}\|_2 \tag{1.2}$$

with γ being the Lipschitz constant. Consider the following Luenberger-like observer

$$\dot{\hat{x}} = A\hat{x} + f(\hat{x}) + L(y - C\hat{x}) \tag{1.3}$$

where $\hat{x}$ is the estimates state vector.

Theorem 1.1. The observer (1.3) is asymptotically stable if $L \in \mathbb{R}^{m\times 1}$ and P exist such that the LMI (1.4) is feasible.

$$\begin{bmatrix} A^T P + PA - C^T L^T P - PLC + \gamma^2 I & P \\ P & -I \end{bmatrix} < 0 \tag{1.4}$$
$$P > 0$$

Proof: [8].

For the second Lipschitz type system, assume the same general dynamic system, but without the linear state term in the process dynamics:

$$\dot{x} = \Psi(Ex) \tag{1.5}$$
$$y = Cx$$

where $\Psi: \mathbb{R} \longrightarrow \mathbb{R}^n$ is a nonlinear function and $E \in \mathbb{R}^{1\times n}$. Consider the observer

$$\dot{\hat{x}} = \Psi(E\hat{x}) + L(y - C\hat{x}) \tag{1.6}$$

Define the set of functions $\psi_i: \mathbb{R} \longrightarrow \mathbb{R}$

$$\psi_i(Ex, E\hat{x}) = \begin{cases} \dfrac{\Psi_i(Ex) - \Psi_i(E\hat{x})}{E\tilde{x}} & for\ E\tilde{x} \neq 0 \\ 0 & for\ E\tilde{x} = 0 \end{cases} \tag{1.7}$$

where $\tilde{x} = x - \hat{x}$ is the estimation error and Ψ_i is the ith element of $\Psi(Ex)$. If $\Psi(Ex)$ is a Lipschitz function of Ex, it is easy to show that the following constant bounds exist on

each ψ_i :

$$\underline{\gamma_i} \leq \psi_i \leq \overline{\gamma_i} \tag{1.8}$$

where $\underline{\gamma_i}$ and $\overline{\gamma}_i$ are constants related to the one-sided Lipschitz constants of $\Psi_i(Ex)$. Hence $\psi_i\ (E\,x)$ is bounded by constants and belongs to a convex set with vertices:

$$\mathcal{V} = \left\{v \in R^{n\,\mathrm{x}\,1} \colon v_i \in \left\{\underline{\gamma_i}\,, \overline{\gamma_i}\right\}, i = 1, \dots, n\right\} \tag{1.9}$$

Theorem 1.2. [9] The observer (1.6) is asymptotically stable if there exists a positive definite matrix P and an observer gain L such that the following LMI-transformable inequality is satisfied at each vertex of the convex set $\mathcal{V}$

$$\sum_{i=1}^{n}\left(PEv_i e_i^T + e_i v_i\, E^T P\right) - C^T L^T P - PLC < 0\,, \qquad \forall v \in \mathcal{V} \tag{1.10}$$

where $e_i = \left[0\,, \dots, \overset{i\text{th}}{\overset{\frown}{1}}\,, \dots, 0\right]^T \in \mathbb{R}^n$ is a unit vector.

1.1.2 Jacobian Based Observer Design

The other popular observer design methods assume that the nonlinearities have bounded Jacobians. Two of these methods are presented here. Consider the system

$$\dot{x} = Ax + B_f f(x) + g(y,u) \tag{1.11}$$
$$y = Cx$$

Assume (A, C) is observable and $f(x)$ is a vector differentiable nonlinear functions with a bounded Jacobian

$$K_1 \preccurlyeq \frac{\partial f}{\partial x} \preccurlyeq K_2 \tag{1.12}$$

where the operator "$\preccurlyeq$" indicates an element-wise inequality.

Theorem 1.3. The Luenberger-like observer for system (1.11) is globally asymptotically stable if there exist matrices L and P such that the following LMI-transformable inequality is feasible [10]:

$$\begin{bmatrix} \bar{A}^T P + P\bar{A} & PB_f \\ B_f^T P & 0 \end{bmatrix} - \begin{bmatrix} 0 & -\frac{K_2^T - K_1^T}{2} \\ -\frac{K_2 - K_1}{2} & I \end{bmatrix} \leq 0$$
$$P \geq 0 \tag{1.13}$$

where $\bar{A} = A + B_f K_1 - LC$.

Another Jacobian based design method uses a 2-DoF observer. Consider a system with linear process dynamics and nonlinear output functions

$$\dot{x} = Ax + Bu \tag{1.14}$$
$$y = Cx + h(x)$$

Consider the following 2-DoF observer

$$\dot{\hat{x}} = A\hat{x} + Bu + L_1[y - C\hat{x} - h\left(\hat{x} + L_2\big(y - C\hat{x} - h(\hat{x})\big)\right)] \tag{1.15}$$

Assume $h(x)$ has bounded Jacobian matrix and satisfies the element-wise inequality

$$K_1 \preccurlyeq \frac{\partial h}{\partial x} \preccurlyeq K_2 \tag{1.16}$$

Then we define $\overline{K} = K_2 - K_1$. It can be shown that the set of $\tilde{x}$ and the function $\phi(t, \tilde{x}) = h(x) - h\left(\hat{x} + L_2\big(y - C\hat{x} - h(\hat{x})\big)\right)$ is covered by the sector condition (1.17).

$$\phi^T(t, \tilde{x})[\phi(t, \tilde{x}) - \overline{K}\big(I - L_2\overline{\overline{K}}\big)\tilde{x} \leq 0 \tag{1.17}$$

where I is the identity matrix and the element-wise inequality $C \preccurlyeq \overline{\overline{K}} \preccurlyeq C + \overline{K}$ is satisfied.

Theorem 1.4. The 2-DoF observer (1.15) is globally asymptotically stable if matrices P, L_1, and L_2 can be found in such a way that the LMI
(1.18) is satisfied.

$$\begin{bmatrix} (A - L_1C)^T P + P(A - L_1C) & -PL_1 \\ -L_1^T P & 0 \end{bmatrix} - \begin{bmatrix} I - \overline{\overline{K}}^T L_2^T & 0 \\ 0 & I \end{bmatrix} \begin{bmatrix} 0 & -\frac{\overline{K}}{2} \\ -\frac{\overline{K}^T}{2} & I \end{bmatrix} [*] < 0 \tag{1.18}$$
$$P > 0$$

where * can be inferred from symmetry.

Proof: [13].

1.2 Stochastic Filters

Another group of estimation methods that are very popular are used for stochastic systems affected by Gaussian disturbance noise. The extended Kalman Filter (EKF) is one of these methods and is widely used for estimation in nonlinear systems. This method is based on linearization of the linear Kalman filter (KF). The algorithm for the EKF [14] is briefly mentioned below in Table 1-1.

Table 1-1. Algorithm for Extended Kalman filter

Dynamic model	$\dot{x} = f(x,u) + B\,w(t), w(t) \sim \mathcal{N}(0,Q)$
	$y_k = h(x_k) + v_k, v_k \sim \mathcal{N}(0,R)$
Initialization of estimates and covariance matrix	$\hat{x}_0 = \hat{x}(t_0)$
	$\mathcal{P}_0 = E\{(x_0 - \hat{x}_0)(x_0 - \hat{x}_0)^T\}$
Gain	$K_k = \mathcal{P}_k^- H_k^T(\hat{x}_k^-)[H_k(\hat{x}_k^-)\mathcal{P}_k^- H_k^T(\hat{x}_k^-) + R]^{-1}$
	$H_k(\hat{x}_k^-) \equiv \frac{\partial h}{\partial x}\Big\|_{\hat{x}_k^-}$
Update step for estimates	$\hat{x}_k^+ = \hat{x}_k^- + K_k[\tilde{y}_k - h(\hat{x}_k^-)]$
	$\mathcal{P}_k^+ = [I - K_k H_k(\hat{x}_k^-)]\mathcal{P}_k^-$
Propagation step for estimates	$\dot{\hat{x}}_k = f(\hat{x}_k, u)$
	$\dot{\mathcal{P}}(t) = F(\hat{x})\mathcal{P}(t) + \mathcal{P}(t)F^T(\hat{x})BQB^T$
	$F(\hat{x}(t),t) \equiv \frac{\partial f}{\partial x}\Big\|_{\hat{x}_k}$

where w and v are Gaussian noise with covariance matrices of Q and R respectively and the matrix $\mathcal{P}$ represents the covariance of estimated states. As it can be seen in Table 1-1, the EKF uses the first order Taylor expansion around the estimated states, and as it will be shown later, this simplification negatively impacts the robustness of this method.

Another method using the probabilistic approach is the Unscented Kalman Filter (UKF). In this method, instead of linearizing the nonlinear functions, the mean and covariance of the states are directly approximated when they go through a nonlinear mapping [15]. This

is done by choosing a number of sample points, known as sigma points, around the estimated state with the help of the covariance matrix from the last time step. The algorithm for UKF is briefly presented in Table 1-2 [16].

Table 1-2. Algorithm for Unscented Kalman filter

Dynamic model	$\dot{x} = f(x(t), u, t) + G(t)w(t), w(t) \sim \mathcal{N}(0, Q)$
	$y_k = h(x_k) + v_k, v_k \sim \mathcal{N}(0, R)$
Initialization of estimates and covariance matrix	$\hat{x}(t_0) = \hat{x}_0$
	$\mathcal{P}_0 = E\{(x_0 - \hat{x}_0)(x_0 - \hat{x}_0)^T\}$
Calculating the sigma points	$\hat{x}_\sigma^{(i)} = \hat{x} \pm (\sqrt{n\mathcal{P}_{k-1}})_i^T \quad i = 1, \dots, n$
	$x_{k-1}^\sigma = [\hat{x}_{k-1}, \hat{x}_\sigma^{(1)}, \dots, \hat{x}_\sigma^{(n)}]$
	$x_{k\|k-1} = f(x_{k-1}^\sigma)$
Mapping sigma points through dynamics	$\hat{x}_k^- = \sum_{i=0}^{2n} W_i^{(m)} x_{k\|k-1}$
	$\mathcal{P}_k^- = \sum_{i=0}^{2n} W_i^{(c)} [x_{k\|k-1} - \hat{x}_k^-][x_{k\|k-1} - \hat{x}_k^-]^T + Q$
Mapping sigma points through output functions	$\mathcal{Y}_{k\|k-1} = h(x_{k-1}^\sigma)$
	$\hat{y}_k^- = \sum_{i=0}^{2n} W_i^{(m)} \mathcal{Y}_{k\|k-1}$
Covariance and cross-covariance approximation	$\mathcal{P}_{yy\|k} = \sum_{i=0}^{2n} W_i^{(c)} [\mathcal{Y}_{k\|k-1} - \hat{y}_k^-][\mathcal{Y}_{k\|k-1} - \hat{y}_k^-]^T + R$
	$\mathcal{P}_{xy\|k} = \sum_{i=0}^{2n} W_i^{(c)} [x_{k\|k-1} - x_k^-][\mathcal{Y}_{k\|k-1} - \hat{y}_k^-]^T$
Update step for estimates	$K_k = \mathcal{P}_{xy\|k} {\mathcal{P}_{xy\|k}}^{-1}$
	$\hat{x}_k = K_k(y_k - \hat{y}_k^-)$
	$\mathcal{P}_k = \mathcal{P}_k^- - K_k \mathcal{P}_{yy\|k} K_k^T$

Since the method of approximating states and covariance matrix is more accurate than

the first order Taylor expansion in the EKF, the UKF generally performs better than the EKF for many applications. However, as will be explained in detail later in this dissertation, subjecting the system to non-Gaussian disturbances can deteriorate the estimation of this technique [15].

1.3 Thesis Contributions

The major contributions of this doctoral dissertation research are as follows:

1) Showing the non-existence of constant gain LMI-based observers for systems with non-monotonic nonlinear outputs: This work led to the recognition of the importance of monotonicity for nonlinear observer design. It has been known that LMI-based observer design methods, some of which were presented in this chapter, cannot find stabilizing solutions for many applications. The reason behind the infeasibility of these methods had not been clear. This thesis clarifies that the non-existence of solutions is often due to non-monotonicity of the systems; it shows that systems that only involve non-monotonic nonlinear functions cannot have constant gain LMI-based solutions. This is done by presenting an observer design method for systems involving nonlinear functions of linear combinations of the states. Since the nonlinear functions are defined to have scalar arguments, it is straightforward to describe the monotonicity or the non-monotonicity of a function. This leads to clarification of circumstances where observer design LMIs are not feasible. Before this realization, an inordinate amount of resources would be spent trying to solve LMI problems that we now know do not have feasible solutions.
2) Application of nonlinear observer design to magnetic position estimation: Since the output functions for this application are non-monotonic, existing nonlinear observer designs could not be applied here. Hence, based on the previous contribution, a new approach was chosen to design observers based on switched gains. Here the domain of non-monotonic functions is divided into separate monotonic regions and different gains are designed for each piecewise

monotonic region. Furthermore, by using observability measures, optimized sensor locations are found to minimize the estimation error with the fewest number of sensors.

3) Development of a nonlinear observer for state of charge estimation in Li-ion batteries using bulk force measurements: A switched gain observer is used to handle non-monotonic nonlinear measurement of bulk force exerted on the casing of Li-ion batteries. The robustness of the devised observer is contrasted with that of the EKF in case of different types of possible model mismatch.
4) Development of modified Preisach method to model hysteresis in Li-ion batteries: It is shown that previous methods for modeling hysteresis in Li-ion batteries suffered from either lack of observability or from being non-Lipschitz. Then, a modified Lipschitz model is introduced in this research and an appropriate nonlinear Lipschitz observer is used to estimate the state of charge of Li-ion batteries in presence of considerable hysteresis.
5) Development of a cascaded nonlinear observer design for infectious disease spread dynamics: A nonlinear dynamic model is developed which enhances the traditional SEIR epidemic model to include additional states of hospitalizations, ICU admissions, and deaths. A six-month data set from Minnesota is used to find the parameters of the model. Subsequently, a cascaded observer consisting of a bilinear nonlinear observer and a linear parameter varying observer is used to estimate the states and rate of the spread of the disease.
6) Comparison of the performance of a H_∞ nonlinear observer with the Extended and Unscented Kalman filters: This thesis extensively compares the performance of a developed H_∞ nonlinear observer with those of the EKF and the UKF for various disturbances in the system. It is shown that the developed observer performs almost as well as the UKF in case of Gaussian disturbances, while outperforming both the EKF and the UKF in systems with pulse disturbances. Furthermore, a bound on the estimation error is found for the nonlinear observer. The calculation of this bound can be used to guarantee the stability of the observer in systems that have limited domains of stability.

Chapter 2
Hybrid Observer for Non-Monotonic Nonlinear Dynamic Systems

2.1 Introduction

While the topic of observer design is analogous to that of controller design for linear time invariant systems, this is no longer the case for nonlinear systems. Observer design for nonlinear systems continues to be a topic of significant research interest. Two major approaches to nonlinear observer design include the high gain observer approach [4], [17] and the LMI-based design approach [2]. The high-gain observer approach is used for systems in triangular form or any system that can be transformed into a triangular structure. The advantage of the high gain methodology is that it always guarantees the existence of an exponentially convergent observer, thanks to the tuning of only one parameter that should be chosen large enough [18]. Although the practicability of high-gain observer in output feedback control has been nicely demonstrated by Khalil's work [1], the use of a large gain and the consequent sensitivity to noise as well as high frequency model uncertainty remains a drawback. To overcome this obstacle, many research papers have addressed high-gain observers with time-varying parameter adaptation, and a number of different switched-gain schemes [19].

The LMI based observer design approaches have been developed in the literature by a

number of different authors for different classes of nonlinear systems. For example, LMI-based observer design methods have been developed for systems with Lipschitz nonlinearities [2], [8] differentiable nonlinear systems with locally bounded Jacobians [10], systems with nonlinearities satisfying an incremental quadratic inequality [11], and for monotonic nonlinear systems [12]. Each new LMI technique aims to provide a better way to get less conservative LMI conditions compared to previous results for the class of systems under consideration. Despite recent theoretical advances in this field [2] [20], the search for a single widely-applicable powerful observer design method still remains open. One of the recent observer results of importance develops a design method which is a bridge between the LMI-based and the high-gain observer design methods [21].

While the above results from literature represent significant progress in developing viable observer design techniques for nonlinear systems, this chapter demonstrates that the design techniques fall short when it comes to actual application to practical nonlinear systems. In particular, this chapter shows that when the nonlinear functions are non-monotonic in the process dynamics, none of the existing observer design methods yield feasible solutions. This constitutes a major shortcoming of all existing nonlinear observer design methods that has not been explicitly recognized in literature.

Since this chapter specifically addresses the question of observer feasibility for non-monotonic systems, the chapter must address all system representations in which the elements of the vector nonlinear functions are functions of scalar combinations of states. The terms “monotonic” and “non-monotonic” do not have any meaning unless each involved nonlinear function is a function only of a scalar combination of variables. Hence, observer design techniques need to be formulated for the nonlinear functions being functions only of a scalar combination of states.

The contributions of this chapter are: the presentation of observer design LMIs for nonlinear systems with representation in the form of functions of scalar state combinations, the demonstration of infeasibility when the nonlinear functions happen to be non-monotonic, the development of hybrid observer design methods that provide global stability for non-monotonic systems, and the application of the developed hybrid observer technique for piston position estimation in industrial actuators.

2.2 Observer Design for Systems with Nonlinear Functions of Scalar Variables

In this section, we develop an observer design method for a class of nonlinear systems in which the process dynamics and outputs both have vector nonlinear functions, with their components being functions of scalar variables. The class of systems is given by the following plant equations

$$\dot{x} = Ff(x) + g(y,u) \tag{2.1}$$

$$y(x) = h(x) \tag{2.2}$$

with

$$f(x) = \begin{Bmatrix} f_1(E_1x) \\ \vdots \\ f_r(E_rx) \end{Bmatrix} \text{ and } h(x) = \begin{Bmatrix} h_1(C_1x) \\ \vdots \\ h_m(C_mx) \end{Bmatrix} \tag{2.3}$$

where $x \in R^n$, $y \in R^m$, $F \in R^{n\,x\,r}$, $E_i^T \in R^n$, $f_i: R \to R$, $i = 1,2,\dots,r$ and $g(y,u): R^{m\,x\,q} \to R^n$. Thus, each of the f_i functions is a function of different scalar variables E_ix. Also, $C_j^T \in R^n$, $h_j: R \to R$ and $j = 1,2,\dots,m$. There are m outputs, but all of them are functions of different scalar variables C_jx. Note that the control input u is decoupled from $f(x)$, although the control input could be coupled to the state by replacing $f(x)$ with $f(x,u)$ if the control input and the Jacobian $\partial f/\partial x$ are both bounded, in spite of the presence of the control input in $f(x,u)$, as done for example in [11].

We also assume that the functions $f(x)$ and $h(x)$ satisfy the following conditions:

$$-\infty < M_j \le \frac{\partial h_j}{\partial(C_jx)} \le N_j < +\infty, \quad j = 1,\dots.,m \tag{2.4}$$

$$-\infty < U_i \le \frac{\partial f_i}{\partial(E_ix)} \le V_i < +\infty, \quad i = 1,2,\dots.,r \tag{2.5}$$

Define the diagonal matrices of the bounds as: $M = diag(M_1, M_2, \dots, M_m)$, $N = diag(N_1, N_2, \dots, N_m)$, $U = diag(U_1, U_2, \dots, U_r)$ and $V = diag(V_1, V_2, \dots, V_r)$.

Note that equation (2.1) can certainly represent nonlinear systems in which each function $f_i(E_ix)$ is a nonlinear function of a scalar linear combination of the states. Further, $Ff(x)$

can represent linear combinations of nonlinear functions $f_i(E_i x)$. The reason it is necessary to consider functions of only scalar variables (and combinations of such functions) is because a monotonic function is properly defined in this manuscript as being either a non-decreasing or non-increasing function of its scalar argument.

Let the state observer be given by

$$\dot{\hat{x}} = Ff(\hat{x}) + g(y,u) + L[y - h(C\hat{x})] \tag{2.6}$$

where $C \in R^{m\,x\,n}$, and $C^T = [C_1^T \quad \ldots \quad C_m^T]$. Note that there is a minor abuse of notation in using $h(Cx)$ instead of $h(C_1x, C_2x, \ldots, C_mx)$, but provides more compact writing.

Let the estimation error be $\tilde{x} = x - \hat{x}$. Then the estimation error dynamics obtained by subtracting (2.6) from (2.1) are given by:

$$\dot{\tilde{x}} = F\tilde{f}(x,\hat{x}) - L\tilde{h}(x,\hat{x}) \tag{2.7}$$

for $\tilde{f}(x,\hat{x}) = f(x) - f(\hat{x})$ and $\tilde{h}(x,\hat{x}) = h(Cx) - h(C\hat{x})$.

Theorem 2.1. If the LMI (2.8) has a feasible solution that yields an observer gain L and a symmetric positive definite matrix $P > 0$, then the observer of equation (2.6) using this observer gain is globally exponentially stable with a convergence rate of at least $\sigma/2$.

$$\begin{bmatrix} -\frac{1}{2}C^T(M^TN + N^TM)C - \frac{1}{2}E^T(V^TU + U^TV)E + \sigma P & PF + \frac{1}{2}(E^TU^T + E^TV^T) & -PL + \frac{1}{2}(C^TM^T + C^TN^T) \\ F^TP + \frac{1}{2}(VE + UE) & -I & 0 \\ -L^TP + \frac{1}{2}(NC + MC) & 0 & -I \end{bmatrix} \leq 0 \tag{2.8}$$

Proof: Consider the Lyapunov function candidate $V = \tilde{x}^T P\tilde{x}$, with $P > 0$. Substituting from equation (2.7), $\dot{V} = \tilde{f}^T F^T P\tilde{x} - \tilde{h}^T L^T P\tilde{x} + \tilde{x}^T PF\tilde{f} - \tilde{x}^T PL\tilde{h}$, or

$$\dot{V} = \begin{bmatrix} \tilde{x} \\ \tilde{f} \\ \tilde{h} \end{bmatrix}^T \begin{bmatrix} 0 & PF & -PL \\ F^TP & 0 & 0 \\ -L^TP & 0 & 0 \end{bmatrix} \begin{bmatrix} \tilde{x} \\ \tilde{f} \\ \tilde{h} \end{bmatrix} \tag{2.9}$$

Using the differential mean value theorem, the output function difference is

$$\tilde{h}(x,\hat{x}) = \begin{Bmatrix} \vdots \\ h_i(C_i x) - h_i(C_i \hat{x}) \\ \vdots \end{Bmatrix} = \begin{bmatrix} \left.\frac{\partial h_1}{\partial (C_1 x)}\right|_{z_1=\bar{z}_1} & 0 & 0 & 0 \\ \vdots & \ddots & \ddots & 0 \\ 0 & & \ddots & 0 \\ 0 & \cdots & 0 & \left.\frac{\partial h_m}{\partial (C_m x)}\right|_{z_m=\bar{z}_m} \end{bmatrix} (Cx - C\hat{x}) \tag{2.10}$$

where $z_i = C_i x$. Then, using the lower and upper Jacobian bounds of $\frac{\partial h_j}{\partial (C_j x)}$ in equation (2.10),

$$\tilde{h}(x,\hat{x}) - MC\tilde{x} = diag\left\{ \left.\frac{\partial h_1}{\partial (C_1 x)}\right|_{z=z_1} - M_1, \ldots, \left.\frac{\partial h_m}{\partial (C_m x)}\right|_{z=z_m} - M_m \right\} C\tilde{x} \tag{2.11}$$

and

$$\tilde{h}(x,\hat{x}) - NC\tilde{x} = diag\left\{ \left.\frac{\partial h_1}{\partial (C_1 x)}\right|_{z=z_1} - N_1, \ldots, \left.\frac{\partial h_m}{\partial (C_m x)}\right|_{z=z_m} - N_m \right\} C\tilde{x} \tag{2.12}$$

From (2.11) and (2.12), due to M_i being a lower bound and N_i being an upper bound in each of the diagonal terms in the diagonal matrices, it follows that

$$\left[\tilde{h}(x,\hat{x}) - MC\tilde{x}\right]^T \left[\tilde{h}(x,\hat{x}) - NC\tilde{x}\right] \leq 0 \tag{2.13}$$

Equation (2.13) can be rewritten in matrix form as

$$[\tilde{x}^T \quad \tilde{h}(x,\hat{x})^T] \begin{bmatrix} C^T M^T NC & -C^T M^T \\ -NC & I \end{bmatrix}^T \begin{bmatrix} \tilde{x} \\ \tilde{h}(x,\hat{x}) \end{bmatrix} < 0 \tag{2.14}$$

Since M and N can also be switched in (2.14), a symmetric form of the constant matrix in (2.14) is

$$\begin{bmatrix} 0.5(C^T M^T NC + C^T N^T MC) & -0.5(C^T M^T + C^T N^T) \\ -0.5(MC + NC) & I \end{bmatrix} < 0 \tag{2.15}$$

Similarly, for the difference $\tilde{f}(x,\hat{x}) = f(x) - f(\hat{x})$, it can be shown that the corresponding symmetric matrix is

$$\begin{bmatrix} 0.5(E^T U^T VE + E^T V^T UE) & -0.5(E^T U^T + E^T V^T) \\ -0.5(UV + VE) & I \end{bmatrix} < 0 \tag{2.16}$$

Combining matrices (2.15) and (2.16) into a larger matrix form, the constraint

$$V_1 = \begin{bmatrix}\tilde{x}\\ \tilde{f}\\ \tilde{h}\end{bmatrix}^T \begin{bmatrix} C^T\left(\frac{M^TN+N^TM}{2}\right)C + E^T\left(\frac{V^TU+U^TV}{2}\right)E & -\left(\frac{E^TU^T+E^TV^T}{2}\right) & -\left(\frac{C^TM^T+C^TN^T}{2}\right) \\ -\left(\frac{VE+UE}{2}\right) & I & 0 \\ -\left(\frac{NC+MC}{2}\right) & 0 & I \end{bmatrix} \begin{bmatrix}\tilde{x}\\ \tilde{f}\\ \tilde{h}\end{bmatrix} \leq 0 \quad (2.17)$$

on the nonlinear functions $\tilde{f}(x,\hat{x})$ and $\tilde{h}(x,\hat{x})$ and their Jacobian bounds is obtained. Replacing the condition $\dot{V} \leq 0$ with the condition $\dot{V} + \sigma P < 0$ ensures that the estimation error has an exponential convergence rate of at least $\sigma/2$, as described in Chapter 4 of [22]. Using the S-procedure Lemma [23], $\dot{V} + \sigma P < 0$ if and only if there exists $\epsilon > 0$ such that $\dot{V} + \sigma P \leq \epsilon V_1$ where V_1 is defined in equation (2.17). Hence, equation

$$[\tilde{x}^T \quad \tilde{f}^T \quad \tilde{h}^T] \begin{bmatrix} \sigma P & PF & -PL \\ F^TP & 0 & 0 \\ -L^TP & 0 & 0 \end{bmatrix} \begin{bmatrix}\tilde{x}\\ \tilde{f}\\ \tilde{h}\end{bmatrix} \leq$$
$$\epsilon \begin{bmatrix} \frac{1}{2}C^T(M^TN+N^TM)C + \frac{1}{2}E^T(V^TU+U^TV)E & -\frac{1}{2}(E^TU^T+E^TV^T) & -\frac{1}{2}(C^TM^T+C^TN^T) \\ -\frac{1}{2}(VE+UE) & I & 0 \\ -\frac{1}{2}(NC+MC) & 0 & I \end{bmatrix} \quad (2.18)$$

is obtained. Absorbing ϵ into the P matrix on the left-hand side of equation (2.18), the LMI of equation (2.8) then follows. ■

It should be noted that Theorem 2.1 is an observer design method for global exponential stability and is only a *sufficient* condition.

The following corollary of Theorem 2.1 is presented below for the special case where only the output equations are nonlinear. In this case, lower dimensional LMI can be obtained in place of the LMI (2.8).

Corollary 2.1. Consider the case where the process dynamics are linear ($Ff(x) = Ax$) and the ouputs are nonlinear. In this case, if an observer gain L and a symmetric positive definite matrix $P > 0$ that satisfy equation (2.19) can be obtained, then the observer with this gain is globally exponentially stable.

$$\begin{bmatrix} A^TP + PA - \dfrac{C^TM^TNC + C^TN^TMC}{2} + \sigma P & -PL + \dfrac{C^TM^T + C^TN^T}{2} \\ -L^TP + \dfrac{MC + NC}{2} & -I \end{bmatrix} \leq 0 \qquad (2.19)$$

Proof: The estimation error dynamics in this case are

$$\dot{\tilde{x}} = A\tilde{x} - L\tilde{h}(x, \hat{x}) \qquad (2.20)$$

Using the same Lyapunov function as in Theorem 2.1,

$$\dot{V} = \dot{\tilde{x}}^T P\tilde{x} + \tilde{x}^T P\dot{\tilde{x}} = \tilde{x}^T A^T P\tilde{x} - \tilde{h}^T L^T P\tilde{x} + \tilde{x}^T PA\tilde{x} - \tilde{x}^T PL\tilde{h}, \text{ or}$$

$$\dot{V} = [\tilde{x}^T \quad \tilde{h}^T] \begin{bmatrix} A^TP + PA & -PL \\ -L^TP & 0 \end{bmatrix} \begin{bmatrix} \tilde{x} \\ \tilde{h} \end{bmatrix} \qquad (2.21)$$

The output difference function in matrix form is

$$V_1 = \begin{bmatrix} \tilde{x} \\ \tilde{h}(x, \hat{x}) \end{bmatrix}^T \begin{bmatrix} \dfrac{C^TM^TNC + C^TN^TMC}{2} & -\dfrac{C^TM^T + C^TN^T}{2} \\ -\dfrac{MC + NC}{2} & I \end{bmatrix} \begin{bmatrix} \tilde{x} \\ \tilde{h}(x, \hat{x}) \end{bmatrix} < 0 \qquad (2.22)$$

Using the S-Procedure Lemma [23] again, with $\dot{V} < \epsilon V_1$ yields the LMI

$$\begin{bmatrix} A^TP + PA & -PL \\ -L^TP & 0 \end{bmatrix} < \epsilon \begin{bmatrix} \dfrac{C^TM^TNC + C^TN^TMC}{2} & -\dfrac{C^TM^T + C^TN^T}{2} \\ -\dfrac{MC + NC}{2} & I \end{bmatrix}$$

Absorbing $1/\epsilon$ into the matrix P to define a new positive definite matrix and adding the term $+\sigma P$ to the (1,1) term above for a minimum convergence rate of $\sigma/2$, the final observer design LMI is obtained as equation (2.19) specified in the Corollary. ■

2.3 Non-Existence of a Constant Observer Gain for Non-Monotonic Systems

2.3.1 Non-Existence for All Non-Monotonic Functions

Theorem 2.2. If ALL of the output functions $h_j(C_j x)$, $j = 1,2, \dots, m$ as well as the process dynamic nonlinear functions $f_i(E_i x)$ $i = 1,2, \dots, r$ are non-monotonic, then a constant gain

observer that satisfies the observer design LMI (2.8) does not exist.

Proof: A necessary condition for (2.8) to be satisfied is that

$$-\frac{1}{2}C^T(M^TN + N^TM)C - \frac{1}{2}E^T(V^TU + U^TV)E + \sigma P < 0 \tag{2.23}$$

If all nonlinear functions are non-monotonic, then $M < 0$, $N > 0$, $U < 0$ and $V > 0$. Hence, a solution to equation (2.23), and therefore to equation (2.8), can never exist.

2.3.2 Non-Existence for Non-Monotonic Outputs

Consider the case where the process dynamics are linear and the output equations have non-monotonic nonlinear functions, as in Corollary 2.1.

Theorem 2.3. If ALL of the output functions $h_i(C_i x)$, $i = 1,2, \dots, m$ are non-monotonic, and if the open-loop system is not already asymptotically stable, then a constant gain observer that satisfies the design LMI (2.21) does not exist.

Proof: For this system where the process dynamics are linear and the outputs are described by nonlinear equations, Corollary 2.1 for observer design applies. Hence, if the LMI (2.21) were feasible, a globally exponentially stable observer would result. For (2.21) to be feasible, a necessary condition is that its (1,1) element be negative definite, or

$$A^TP + PA - \frac{C^TM^TNC + C^TN^TMC}{2} + \sigma P < 0 \tag{2.24}$$

If all the output functions are non-monotonic, then $M_i < 0$ and $N_i > 0$. This implies $M^TN < 0$ and $N^TM < 0$.

Since $C^TM^TNC + C^TN^TMC \leq 0$, and $P > 0$, this implies $A^TP + PA < 0$. For $A^TP + PA$ to be negative definite, A must exponentially stable, which contradicts the assumptions of the Theorem. Hence, a constant gain observer that satisfies (2.21) cannot exist.

2.3.3 Non-Existence for Non-Monotonic Process Dynamics

Consider the case where the process dynamics are nonlinear, and the output measurement equations are linear.

Corollary 2.2: If the system under consideration has nonlinear process dynamics and a linear output equation, and is a single output system, then a constant gain observer does

not exist if the output function is non-monotonic.

Interpretation and Relation to Unobservability: The proof of Corollary 2.2 follows directly from Theorem 2.3. Further, the non-existence result is easy to interpret in the case of the single output system. If the output nonlinear function is non-monotonic, then it has both positive and negative values of the derivative with respect to its argument. This implies that for $A - L\frac{\partial h}{\partial (Cx)}C$ to be asymptotically stable, L has to change signs with the sign of $\frac{\partial h}{\partial (Cx)}$, or else the open-loop matrix A must already be stable. Hence, the non-existence result can be easily understood for this single output system. Further, note that when $\frac{\partial h}{\partial (Cx)}$ changes sign, it also goes through a value of zero, implying local loss of observability at one point in the operating domain of the system. Thus, the lack of a stabilizing observer gain for this non-monotonic system agrees with the *loss of observability* that occurs at the zero-slope point of the output nonlinear function.

2.3.4 Non-Existence for Partially Non-Monotonic Outputs

The previous two sub-sections showed that a stabilizing constant observer gain does not exist for the cases where either all output functions, or all process dynamic functions are non-monotonic. This sub-section presents examples to show that a stabilizing observer gain may not exist even if only SOME of the outputs have non-monotonic functions.

Example 1. Consider the special case where the plant equations are

$$\dot{x} = Ax + Bu \tag{2.25}$$

$$y = h(C_0 x) \tag{2.26}$$

with $C_0^T \in R^n$ and $h: R \to R^m$. Thus, there are m outputs, but all of them are functions of the same single scalar variable $C_0 x$.

In this case, the observer design condition is

$$\begin{bmatrix} A^T P + PA - \dfrac{C^T M^T NC + C^T N^T MC}{2} + \sigma P & -PL + \dfrac{C^T M^T + C^T N^T}{2} \\ -L^T P + \dfrac{MC + NC}{2} & -I \end{bmatrix} \leq 0 \tag{2.27}$$

Now, since $C^T C$ is a rank one matrix (due to all rows of C being the same C_0),

$$\frac{C^T M^T N C + C^T N^T M C}{2} = \left(\sum_i M_i N_i\right) C_0^T C_0 \tag{2.28}$$

Now $\sum_i M_i N_i$ is a scalar and could be positive or negative, depending on how many output functions are non- monotonic and have negative values of M_i and positive values of N_i. If $\sum_i M_i N_i$ turns out to be negative, even if only some of the output functions are non-monotonic, then

$$\frac{C^T M^T N C + C^T N^T M C}{2} = \left(\sum_i M_i N_i\right) C_0^T C_0 \leq 0 \tag{2.29}$$

Hence

$$A^T P + P A - \frac{C^T M^T N C + C^T N^T M C}{2} + \sigma P < 0 \Rightarrow A^T P + P A < 0$$

which again would require A itself to be exponentially stable, which would contradict the assumptions of Theorem 2.3.

Hence, a constant observer gain may not exist, even if only some of the output functions are non- monotonic.

Example 2. Consider the 3rd order system with $C_1 = [a \quad b \quad c]$ and $C_2 = [d \quad e \quad f]$. Without loss of generality, let the first output function be monotonic with $m_1 = 0$ and $n_1 > 0$. Let the second output function be non-monotonic with $m_2 < 0$ and $n_2 > 0$, with $m_2 n_2 = -1$. Then

$$\frac{C^T M^T N C + C^T N^T M C}{2} = \begin{bmatrix} -d^2 & -de & -df \\ -de & -e^2 & -ef \\ -df & -ef & -f^2 \end{bmatrix}$$

It is easy to see that there are many values of d, e and f such that $\frac{C^T M^T N C + C^T N^T M C}{2} \leq 0$. This would again make the assumptions of Theorem 2.3 invalid, even though only one of the two output functions is non monotonic.

2.3.5 Non-Existence of a Constant Gain with Other LMI-Based Methods of Nonlinear Observer Design

It can be shown that the following popular methods of observer design for nonlinear systems from literature all fail to yield a solution with a constant observer gain for systems with all non-monotonic nonlinear functions:

a) Observer design method of Arcak and Kokotovic using the Circle Criterion [12]
b) Observer design method of Phanomcheong, et al for bounded Jacobian nonlinear systems [24]
c) High gain observer design method, when the output function is non-monotonic, as demonstrated in [18].

As for the extended Kalman filter (EKF), it is not related to the non-existence results as introduced in this chapter because the EKF uses a time-varying observer gain, instead of a constant one.

Another popular method of nonlinear observer design is through transformation to a normal form under which the observer design can be done simply with eigenvalue assignment with a constant observer gain. However, it is also important to note that in the original coordinates, the gain may not be constant because it depends on the (left) inverse of the state transformation Jacobian, which is not constant if the coordinate transformation is not constant.

Further, finding a nonlinear transformation to put the nonlinear system under a normal form is not an easy task in general, and sometimes requires solvability of a set of partial differential equations. We recognize that normal-form-based methods are useful for observer design, but the use of the switched gain approach proposed in this manuscript does not require any transformation of the system nor any changes to the structure of the LMI conditions obtained with a constant observer gain. We need only to switch between regions of monotonicity.

No Benefits from Conversion to Monotonicity by Linear Subtraction

A non-monotonic function that has a bounded Jacobian can be converted to a monotonic function by subtracting a linear function of the states from it. This conversion

aspect has been described in previous observer design results from literature [12]. This section shows that such a conversion does not help in observer design. Consider a system with nonlinear output functions and linear process dynamics as follows:

$$\dot{x} = Ax + Bu \tag{2.30}$$

$$y = h(Cx) \tag{2.31}$$

with $C \in R^{m \times n}$, and $h: R \to R$. Let the original nonlinear output functions be *non-monotonic* so that the diagonal matrices satisfy $M < 0$ and $N > 0$. The original observer design LMI (as derived in Corollary 2.1) is (2.19).

Conversion to a monotonic nonlinear function:

Let $\phi(Cx) = h(Cx) - MCx$. Then $\frac{\partial \phi}{\partial z} = \frac{\partial h}{\partial z}\Big|_{z=Cx} - M$. Then, it is easy to see that

$$0 \leq \frac{\partial \phi}{\partial z}\Big|_{z=Cx} \leq N - M \tag{2.32}$$

Therefore $\frac{\partial \phi}{\partial z} \geq 0$ and hence all the functions in $\phi(Cx)$ are monotonic. Can we use the new nonlinear function $\phi(Cx)$ to re-define the output? Rewrite the original output as

$$y = MCx + h(Cx) - MCx = MCx + \phi(Cx) \tag{2.33}$$

Rewrite the plant dynamics as

$$\dot{x} = (A - LMC)x + LMCx + Bu \tag{2.34}$$

and the observer as

$$\dot{\hat{x}} = (A - LMC)\hat{x} + LMC\hat{x} + Bu + L(h(Cx) - h(C\hat{x})) \tag{2.35}$$

Then, the estimation error dynamics are

$$\dot{\tilde{x}} = (A - LMC)\tilde{x} + L(\phi(Cx) - \phi(C\hat{x})) \tag{2.36}$$

with $\phi(Cx)$ being a monotonic function.

The new observer design LMI uses $(A - LMC)$ instead of A. Also, the lower Jacobian bound of $\phi(Cx)$ is 0 and the upper Jacobian bound is $N - M$ because of the monotonicity of the new output. Then the new observer design LMI, by applying equation (2.19) is

$$\begin{bmatrix} (A-LMC)^T P + P(A-LMC) + \sigma P & -PL + \dfrac{(N-M)C^T}{2} \\ -L^T P + \dfrac{(N-M)C}{2} & -I \end{bmatrix} \leq 0 \qquad (2.37)$$

This requires $(A-LMC)^T P + P(A-LMC) + \sigma P < 0$ as a necessary condition. Hence $(A-LMC)$ needs to be an asymptotically stable matrix, with $M < 0$.

Theorem 2.4. The observer design for the new system (2.33)-(2.34) in which the nonlinear function has been converted to a monotonic function continues to be infeasible, if it was infeasible for the original system before conversion.

Proof: By using the Schur complements Lemma, the observer LMI (2.37) for the system (2.33)-(2.34) is equivalent to

$(A-LMC)^T P + P(A-LMC) + \sigma P + \left(-PL + \frac{C^T(N-M)^T}{2}\right)\left(-L^T P + \frac{(N-M)}{2} C\right) \leq 0$, i.e.

$$\begin{aligned} A^T P + PA + PLL^T P - C^T \left(\frac{N+M}{2}\right)^T L^T P - PL\left(\frac{N+M}{2}\right) C \\ + \frac{1}{4} C^T (N-M)^T (N-M) C + \sigma P \leq 0 \end{aligned} \qquad (2.38)$$

On the other hand, the original observer design LMI for the untransformed system(2.30)-(2.31), using equation (2.19), is equivalent to

$$\begin{bmatrix} A^T P + PA - \dfrac{C^T M^T NC + C^T N^T MC}{2} + \sigma P & -PL + \dfrac{C^T M^T + C^T N^T}{2} \\ -L^T P + \dfrac{MC + NC}{2} & -I \end{bmatrix} \leq 0 \qquad (2.39)$$

$A^T P + PA - \frac{C^T M^T NC + C^T N^T MC}{2} + \sigma P + \left(-PL + \frac{C^T M^T + C^T N^T}{2}\right)\left(-L^T P + \frac{MC+NC}{2}\right) \leq 0$, i.e.

$$A^T P + PA + PLL^T P - C^T \left(\frac{N+M}{2}\right)^T L^T P - PL\left(\frac{N+M}{2}\right) C + \frac{1}{4} C^T (N-M)^T (N-M) C + \sigma P \leq 0 \qquad (2.40)$$

Thus, inequality (2.39) turns out to be completely equivalent to inequality (2.40). ■

Hence the conversion of the non-monotonic output function to a monotonic one by

subtracting a linear term did not help. A constant gain observer continues to be infeasible, if the original function is non-monotonic.

2.4 Hybrid Observer Design Using Switched Gains and Switched Lyapunov Functions

For the plant with nonlinear process dynamics and nonlinear output equations, as given in (2.1)-(2.2), consider a hybrid observer with two constant-gain regions, as shown in Figure 2-1, with no loss of generality. Let the observer be designed with an observer gain L_1 in region 1 and L_2 in region 2. Let the two observers be designed to be exponentially stable in each of the two regions using the following two LMIs:

$$\begin{bmatrix} -\frac{1}{2}C^T(M^TN+N^TM)C-\frac{1}{2}E^T(V^TU+U^TV)E+\sigma_1P_1 & P_1F+\frac{1}{2}(E^TU^T+E^TV^T) & -P_1L_1+\frac{1}{2}(C^TM^T+C^TN^T) \\ F^TP_1+\frac{1}{2}(VE+UE) & -I & 0 \\ -L_1^TP_1+\frac{1}{2}(NC+MC) & 0 & -I \end{bmatrix} \leq 0 \quad (2.41)$$

for all $y \leq y_{switch}+\epsilon$,

$$\begin{bmatrix} -\frac{1}{2}C^T(M^TN+N^TM)C-\frac{1}{2}E^T(V^TU+U^TV)E+\sigma_2P_2 & P_2F+\frac{1}{2}(E^TU^T+E^TV^T) & -P_2L_2+\frac{1}{2}(C^TM^T+C^TN^T) \\ F^TP_2+\frac{1}{2}(VE+UE) & -I & 0 \\ -L_2^TP_2+\frac{1}{2}(NC+MC) & 0 & -I \end{bmatrix} \leq 0 \quad (2.42)$$

for all $y \geq y_{switch}-\epsilon$. Here y_{switch} is the nominal switching point between the two regions and the variable ϵ is the hysteresis added to the switching to ensure a minimum dwell time after each switch.

Note that a nonlinear function on a compact set has finite local extrema and can always therefore be represented using piecewise monotonic functions. Hence, the observer can be designed using a finite set of piecewise regions with the monotonicity being ensured in each region.

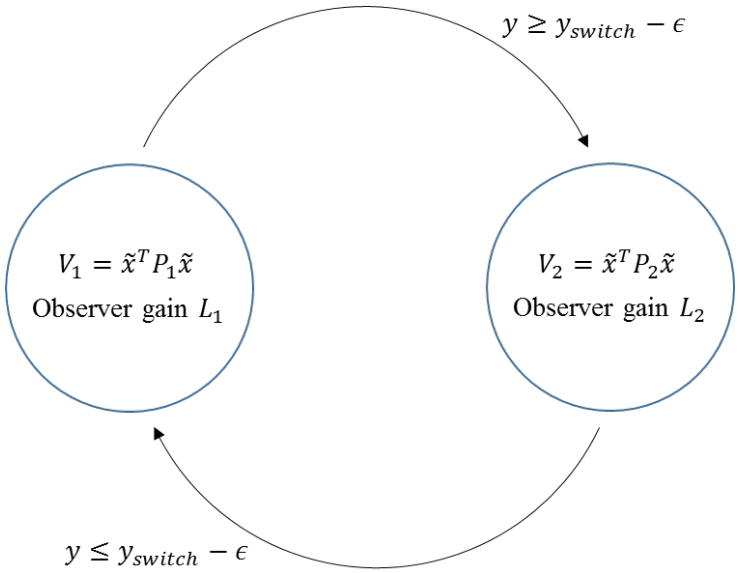

Figure 2-1. Hybrid observer

Theorem 2.5. Let P_1, L_1 and P_2, L_2 be the Lyapunov function matrices and observergain matrices in regions 1 and 2 respectively, chosen so as to satisfy equations(2.41), (2.42). Let σ_1 and σ_2 be the minimum exponential convergence constants in the two regions. Choose a value of τ such that the following equations are satisfied:

$$P_1 \geq P_2 e^{-\tau\sigma_2} \tag{2.43}$$

and

$$P_2 \geq P_1 e^{-\tau\sigma_1} \tag{2.44}$$

Then, if the switching between regions does not occur faster than τ, the hybrid observer system will be asymptotically stable.

Proof: Without loss of generality, consider a switching from region 1 to region 2. Let the switching occur at time t_s. Then, according to the assumption in the Theorem 2.5, the switch back cannot occur before $t_s + \tau$.

At the time of switching, the value of the Lyapunov function in region 1 is

$$V_1(t_s) = \tilde{x}(t_s)^T P_1 \tilde{x}(t_s) \tag{2.45}$$

and in region 2 is

$$V_2(t_s) = \tilde{x}(t_s)^T P_2 \tilde{x}(t_s) \tag{2.46}$$

Since region 2 has a minimum exponential convergence constant of σ_2,

$$\dot{V}_2(t) \leq -\sigma_2 V_2(t) \tag{2.47}$$

Rearrange (2.47), then

$$\frac{1}{V_2(t)} dV_2(t) \leq -\sigma_2 dt \tag{2.48}$$

Integrate both sides of (2.48) to obtain a relationship between $V_2(t_s + \tau)$ and $V_2(t_s)$:

$$\int_{V_2(t_s)}^{V_2(t_s+\tau)} \frac{1}{V_2(t)} dV_2(t) \leq -\int_{t_s}^{t_s+\tau} \sigma_2 dt \tag{2.49}$$

Then, (2.49) becomes

$$\ln\left\{\frac{V_2(t_s+\tau)}{V_2(t_s)}\right\} \leq -\sigma_2(t_s + \tau - t_s) \tag{2.50}$$

Using (2.50), the relationship between $V_2(t_s + \tau)$ and $V_2(t_s)$ can be obtained as

$$V_2(t_s + \tau) \leq V_2(t_s) e^{-\tau\sigma_2} \tag{2.51}$$

Equation (2.51) implies

$$\tilde{x}(t_s + \tau)^T P_2 \tilde{x}(t_s + \tau) \leq \tilde{x}(t_s)^T P_2 \tilde{x}(t_s) e^{-\tau\sigma_2} \tag{2.52}$$

According to (2.43), following inequality is satisfied:

$$\tilde{x}(t_s + \tau)^T P_2 \tilde{x}(t_s + \tau) \leq \tilde{x}(t_s)^T P_2 e^{-\tau\sigma_2} \tilde{x}(t_s) \leq \tilde{x}(t_s)^T P_1 \tilde{x}(t_s) \tag{2.53}$$

Hence, we have

$$V_2(t_s + \tau) \leq V_1(t_s) \tag{2.54}$$

Subsequently, for all $t \geq t_s + \tau$, $V_2(t)$ further keeps decreasing exponentially with an exponential time constant of at least σ_2, as long as the system remains in region 2.

After each switching between modes, the Lyapunov function always decreases to a value below the value at the time of transition and subsequently continues decreasing exponentially. Hence, the values of the Lyapunov function candidate at consecutive switching points t_{s_1} and t_{s_2} can be related by

$$V_2(t_{s_2}) \leq \alpha V_1(t_{s_1}) \tag{2.55}$$

where $0 \leq \alpha < 1$. Hence, after k switches with a minimum dwell time τ after each switch,

we have

$$V_j(t_{s_k}) \leq \alpha^{k-1} V_1(t_{s_1}) \tag{2.56}$$

where V_j can be V_1 or V_2, depending on whether k is even or odd respectively.

Equation (2.56) for the repeated decay of the Lyapunov function at consecutive switching points, together with the exponential decay that occurs in each region when there is no switching, ensures that the Lyapunov function converges to zero [25]. Hence the estimation error also converges asymptotically to zero. Literature on the design of switching observers and on the stability analysis of switched hybrid systems is available in [25, 26, 27, 28]. ■

Note that it is always possible to find a $\tau > 0$ sufficiently large such that both of the design equations (2.43) and (2.44) are satisfied.

2.5 Application to Magnetic Position Estimation in Industrial Actuators

This section focuses on a motion estimation problem, involving estimating the position of a moving piston inside an industrial piston-cylinder actuator. Magnetic position estimation offers an excellent inexpensive and non-contacting method of obtaining piston position on such actuators, including on pneumatic cylinders, hydraulic actuators and IC engines. In magnetic position estimation, a magnet is placed on the moving object, such as the moving piston shown in Figure 2-2 [29]. A sensor board containing one or more magnetic sensors is placed on the outside cylinder, again as shown in Figure 2-2. Such magnetic sensors are inexpensive (as low as $1 each when purchased in large quantities). At the same time, they enable non-contact estimation of position of the piston. Traditional sensors such as potentiometers and LVDTs require the sensor to be connected co-axially to the moving piston. This requires significant installation effort, results in contacting motion and in shear loads on the sensor during operation, often resulting in sensor failure. Furthermore, potentiometers and LVDTs can be significantly more expensive than the low-cost magnetic sensors considered in this chapter.

The variation of the magnetic field with piston position is shown in Figure 2-3 for an example electrohydraulic actuator with a magnet installed on its piston. The model for the position estimation dynamic system for the EHA when using two magnetic sensor outputs can be represented as:

$$\dot{x} = Ax + Bu$$
$$\begin{bmatrix} y_1 \\ y_2 \end{bmatrix} = \begin{bmatrix} h_1(C_1 x) \\ h_2(C_2 x) \end{bmatrix} \tag{2.57}$$

where $x = \begin{bmatrix} z \\ v \\ a \end{bmatrix}$, $A = \begin{bmatrix} 0 & 1 & 0 \\ 0 & 0 & 1 \\ 0 & 0 & 0 \end{bmatrix}$ and $C_1 = C_2 = [1\ 0\ 0]$.

with z, v and a being the position, velocity and acceleration of the piston. Note that the output equations in (2.57) are highly nonlinear functions of the position z. The functions $h_1(C_1 x)$ and $h_2(C_1 x)$ were defined using polynomial curves to fit the experimentally measured data of Figure 2-3. These functions are seen to be not only nonlinear but also non-monotonic with both positive and negative slopes.

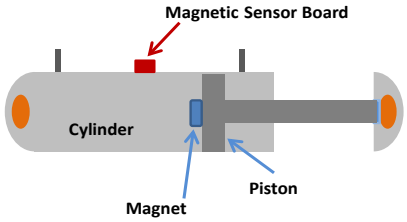

Figure 2-2. Sensor Configuration for position estimation of EHA

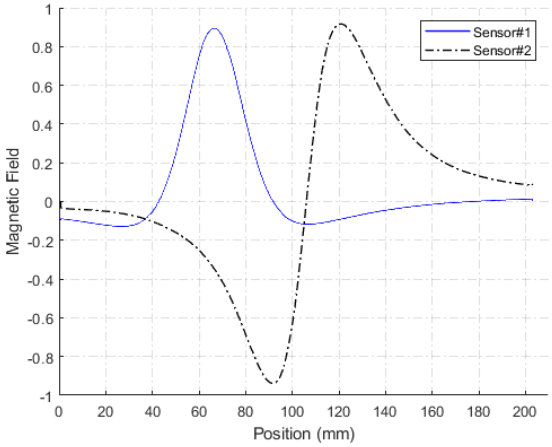

Figure 2-3. Non-monotonic measurement functions of magnetic sensors, after removal of hysteresis

From the theoretical results in section 2.2 (Corollary 2.1), we have seen that if both

output functions are non-monotonic, we cannot find a feasible solution to the observer design LMI (2.19). With the monotonicity requirement in mind, the position range of 0 – 203 mm can be divided piecewise into different regions in a manner that in each region at least one of the output functions is a monotonic function of position. Such a piecewise division of the position range into regions R_1 to $R_{11}$is shown in Figure 2-4. Note that the boundaries of the regions lie near the slope change points (of one or the other output function). For example, R_4 is a narrow region in which the slope of the output y_1 is close to zero. In this region, only the output y_2 will be used by the observer, since y_2 is monotonic in this region. Regions R_3 and R_5 lie on either side of R_4 and both of these regions can utilize both outputs y_1 and y_2, since they are monotonic in these regions.

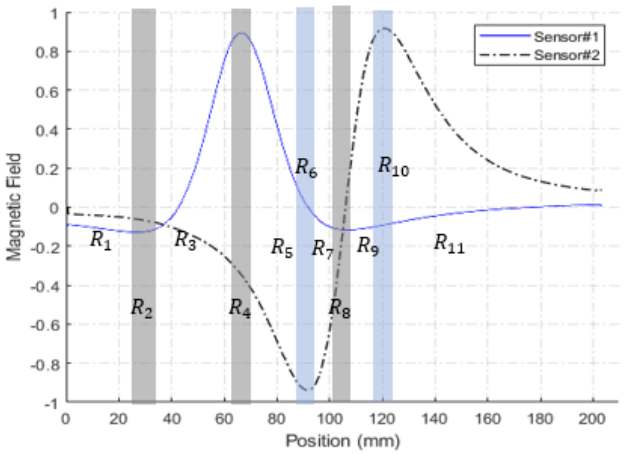

Figure 2-4. Creating regions around slope-change points of output functions

It should be noted that we have the liberty of relying on only one of the output measurements in the narrow regions with zero slope, because even with one output the system is still observable, although the results of estimation might not be as accurate as the case when we use both outputs. Hence, the width of these regions was kept narrow so as to minimize regions with use of only 1 output by the observer. It is ideal to have these regions to be as narrow as possible, but in practice their width is determined by the accuracy of the measurement models. For example, if we anticipate a considerable horizontal uncertainty or shift in the output functions, we are forced to sacrifice the estimation accuracy for the sake of stability by widening the low observability regions.

A switched gain observer can be developed using the regions defined in Figure 2-4 [29]. The switched gain observer uses different gains in each of the discrete piecewise regions. Since each region R_1 through R_{11} has monotonic output function properties, a constant stabilizing observer gain exists in each of these regions. As the operating region changes, the observer gains switch in value accordingly using a finite state machine of the type shown in Figure 2-1.

One obstacle that could affect the performance of this piecewise nonlinear observer is the initial condition. If we pick the initial condition to be in the wrong region (with the wrong observer gain), it might result in a divergence of the observer estimates. However, thanks to the specific shape of output functions for this application, there is an easy solution that can remedy this shortcoming. From Figure 2-4, since there is a one-to-one relationship between the position and the ordered pair that is constructed by the two output functions y_1 and y_2, we can identify the correct region for the initial condition accurately.

2.6 Conclusions

This chapter considered the design of observers for nonlinear systems and the aspect of how observers can be designed in nonlinear systems which are non-monotonic. The plant considered is one in which the process dynamics and output equations are both composed of nonlinear vector functions of scalar combinations of the states. The nonlinear functions are assumed to be differentiable with bounded derivatives. An observer design algorithm that requires solving just a single linear matrix inequality for exponentially convergent state estimation was developed. The developed algorithm worked effectively when the involved nonlinear functions were monotonic. Since each component of the nonlinear functions was a function of a scalar variable, it could be analyzed as being either monotonic or non-monotonic.

The developed observer design method was seen to fail in yielding an observer solution when all or sometimes even some of the system functions were non-monotonic. Analytical results were presented to show that no solutions exist to the observer design LMIs when either all output functions or all process dynamics functions are non-monotonic. Further,

other observer design methods from literature also fail when the involved nonlinear functions are non-monotonic. This relationship between the nonlinear functions being non-monotonic and the feasibility of solutions to the observer design LMIs has not previously been recognized in observer design literature. Previous observer design results in literature have focused on the size of the Lipschitz constant or on the size of the Jacobian bounds in influencing the existence of a stabilizing observer gain. The result in this chapter shows that these LMI-based observer design methods will not succeed for a full non-monotonic system, no matter how small the Lipschitz constant or the Jacobian bounds of the nonlinearity.

Finally, a hybrid observer technique that switches between multiple constant observer gains was developed that can provide global asymptotic stability for systems with non-monotonic nonlinear functions. The need for hybrid observers with switched gains becomes important for such non-monotonic systems. The global stability of the hybrid observer was established when there is sufficient dwell time in each locally stable constant gain observer region.

The application of the developed hybrid observer to a motion estimation problem was presented. This estimation problem involved position estimation for an industrial actuator using a magnetic sensor and handled a plant with nonlinear output equations.

Chapter 3

Hybrid Nonlinear Observer for Battery State-of-Charge Estimation Using Non-Monotonic Force Measurements

3.1 Introduction

3.1.1 Background

Lithium-ion cells dominate the battery market for automotive propulsion and for consumer electronics due to their advantages of high energy density and slow self-discharge [30], [31]. The state-of-charge (SOC) of a lithium ion battery is a basic indicator of the fraction of charge that remains in the battery cells. SOC needs to be estimated accurately in real-time, since it is indicative of the remaining range of operation of the battery, which is especially critical in the case of an electrical vehicle. SOC is typically estimated using a measurement of the terminal voltage, an electrical circuit model and by effectively inverting the voltage-SOC curves of the battery. In this regard, the sensitivity of the voltage curves to the SOC is very important in order to estimate SOC accurately [32]. In the case of the Lithium-ion-Iron-Phosphate (LFP) battery used in this chapter, the relationship between voltage and SOC has an almost-flat slope for most of the SOC range (30-70%), as seen in Figure 3-3. Hence the estimation of SOC from the voltage measurement is quite difficult under noisy measurements [32], [33], [34]. This chapter, therefore, considers the use of an additional sensor, namely a load cell force sensor, to

estimate SOC.

3.1.2 Review of State of Charge Estimation Methods

The state of charge (SOC) of a battery is an indicator of the remaining energy in it, and can be defined as:

$$SOC(t) = 1 - \frac{\int_0^t I\, dt}{C_n} \tag{3.1}$$

Here I is the current supplied by the battery and C_n is the nominal capacity of the battery. While C_n has the SI units of $A.secs$ in the above equation, the units of $A.hours$ is more typically used to describe a battery's capacity. In general,

$$0 \leq SOC(t) \leq 1 \tag{3.2}$$

Different methods for estimating the SOC have been explored in the literature. These include coulomb counting, open circuit voltage measurement, internal resistance measurement, bulk force measurement and electrochemical impedance spectroscopy. A few of these SOC estimation methods are briefly discussed below.

Coulomb Counting

The easiest method for estimation of SOC is coulomb counting which is essentially measuring and integrating the current from the battery over time, as in equation (3.1). Even though this method seems straightforward, an integrator is a marginally stable dynamic system and is highly prone to drift errors. For example, even a very small bias in current measurement will cause large cumulative errors in the estimator. To prevent drift or to manage drift for long time intervals, the current has to be measured very accurately and further the integral has to be reset each time the battery is fully charged (the only condition in which the SOC is accurately known).

Open Circuit Voltage

It has been observed that the open circuit voltage V_{OC} of the battery is an algebraic function of SOC, therefore the inverse of this function can be utilized in the estimation algorithm. There are three major problems associated with using V_{OC} for SOC estimation [35]:

1) The V_{OC} is quite a sensitive function of SOC at low and high SOC values. But there

are intermediate regions of SOC where V_{OC} is not a sensitive function of SOC, as seen in Figure 3-3.

2) A significant hysteresis in battery terminal voltage can be observed with respect to SOC [35]. In other words, V_{OC} is not accurately a one-to-one or even many-to-one function of SOC. The value of V_{OC} depends on the history or memory of the charging-discharging that has occurred up to that point.
3) V_{OC} itself cannot be directly measured, but must instead be estimated from the terminal voltage V_t of the battery. The relationship between V_t and OCV is described in the plant model equations in section II A.

Bulk Force

It has been known that the insertion of Lithium ions into the electrode host materials (intercalation and de-intercalation) during charging and discharging can cause expansion of the crystal lattice of the material. This expansion of the particles in the electrode results in a volume change of the battery. It was shown by Mohan et al. [36] that the force exerted on the casing of the battery as a result of this change in volume is an algebraic function of SOC. Hence, if the bulk force can be measured, the SOC could potentially be estimated from it in real-time. The use of bulk force measurements by some of the authors of this chapter and by others has been previously reported in [32], [36], [37], [38], [39] and [40]. Model development and validation can be seen in [38], [39] and [40]. In the case of the lithium iron phosphate (LFP) cathode battery chemistry used in this chapter and in [32], the relationship between the bulk force and SOC of the battery is quite nonlinear and non-monotonic, making the design of the estimation algorithm quite challenging. Previously, this has been handled by using piecewise linearization of the output nonlinear function and use of a traditional Kalman filter [32].

3.1.3 Chapter Outline

This chapter focuses on the use of the terminal voltage and the force sensor with the LFP battery for real-time estimation of the battery SOC. The design of a nonlinear observer which provides globally stable SOC estimation for the nonlinear system is demonstrated. It turns out that the non-monotonic nature of the nonlinear function prevents the existence

of a single constant observer gain that can provide stability over the entire operating regime of the battery. Hence a hybrid observer that uses a finite state machine to switch between a few constant gain nonlinear observers is utilized.

The clear advantages of the new nonlinear observer over a traditional estimation algorithm such as the extended Kalman Filter are demonstrated in this chapter. In particular, model errors in the output nonlinear function coupled with the non-monotonic nature can easily cause the EKF to diverge. While careful choice of the covariance characteristics for the EKF can be used to prevent divergence, these choices come with significant performance trade-offs. The hybrid nonlinear observer developed in this chapter, on the other hand, provides accurate and robust performance in the presence of model error, and does not need any careful tuning of parameters.

The outline of the chapter is as follows: Section 3.2 presents the dynamic plant model and output functions for the lithium-ion-battery used in this study. Section 3.3 presents the nonlinear observer design method proposed to be used for this plant and also provides an analytical proof that a single constant observer gain over the entire SOC range cannot exist for this system. Section 3.4 presents the design of a hybrid nonlinear observer that utilizes switched observer gains to obtain global stability. Section 3.5 presents extensive results from simulation using both the nonlinear observer and an extended Kalman filter (EKF). Section 3.6 discusses the influence of model error, especially at the zero-slope point for this non-monotonic system. Section 3.7 discusses the initial condition and initial gain determination. Section 3.8 presents experimental results which verify the robustness and performance of the nonlinear observer and its superiority over the EKF. Section 3.9 contains the conclusions.

3.2 Lithium-Ion Battery Dynamic Model

3.2.1 Plant Model for Observer Design

Models with different levels of complexity have been proposed in the literature for the electrical dynamics of lithium-ion batteries [41], [42], [43]. Here an equivalent circuit V_{OC}-R-RC-RC model will be used to model the electrical dynamics, as shown in Figure 3-1

[32].

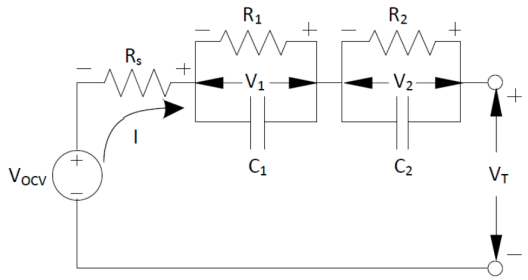

Figure 3-1. V_{OC}-R-RC-RC model for battery [32]

For the model in Figure 3-1, the dynamic equations of the battery can be represented as [32]:

$$\frac{dV_1}{dt} = \frac{-V_1}{R_1C_1} + \frac{I}{C_1} \tag{3.3}$$

$$\frac{dV_2}{dt} = \frac{-V_2}{R_2C_2} + \frac{I}{C_2} \tag{3.4}$$

$$\frac{d\,SOC}{dt} = -\frac{I}{C_n} \tag{3.5}$$

where V_1, V_2 and i are voltages and current, as seen in Figure 3-1, R_1, R_2, C_1, C_2 are electrical model parameters and C_n is the capacity of the battery.

Two output measurements will be considered here; first the terminal voltage y_1 which is a function of all three states and second, the bulk force y_2 which is assumed to be an algebraic function of the SOC.

$$y_1 = V_t = V_{OC}(SOC) - IR - V_1 - V_2 \tag{3.6}$$

$$y_2 = F = F(SOC) \tag{3.7}$$

Thus, considering equations (3.3)-(3.7), the plant model is of the following form:

$$\dot{x} = Ax + Bu \tag{3.8}$$

$$y = Cx + h(x) \tag{3.9}$$

where $x = [V_1 \quad V_2 \quad SOC]^T$, and $y = [y_1 \quad y_2]^T$. It can be seen that the process dynamics are linear while the output functions are nonlinear.

3.2.2 Simulation Model

While equations (3.3)-(3.7) will constitute the battery model that will be used to design

the observer, in order to evaluate the observer in simulations, the following modification were made to the model for purposes of the simulation:

- A small unknown bias was added to the current (the current was assumed to have a small bias error when its measurement is used in the observer).
- Gaussian noise was added to both measurement signals in the simulations.

The simulated outputs and current input are presented in Figure 3-2 This simulation scenario consists of multiple cycles of Dynamic Stress Testing (DST) which is a standard procedure to test the performance of a battery on electric vehicles [44], [45], [46]. The test consists of a long series of step charge/discharge current inputs with non-zero average that are used back-to-back to charge and discharge a battery. Here we see three rounds of battery charge and discharge in this simulation scenario.

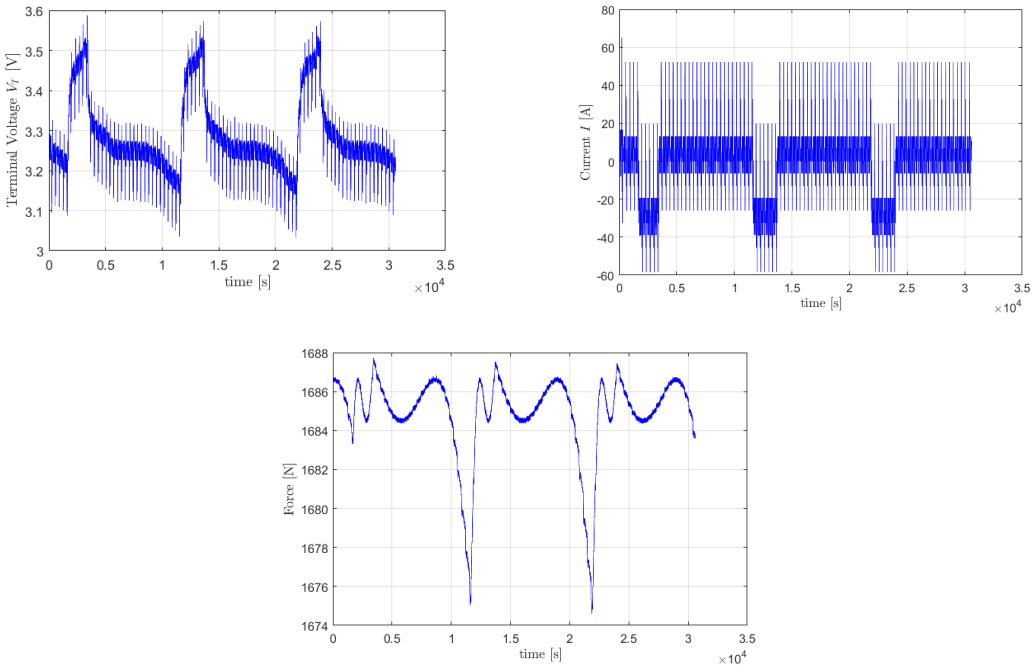

Figure 3-2. Measurements and the input current for simulation studies

3.2.3 Output Functions

The two functions $V_{OC}(SOC)$ and $F(SOC)$ involved in the output equations (3.6) and (3.7) are shown as curves in Figure 3-3. As seen in Figure 3-3, both these functions are

nonlinear functions of SOC. However, $V_{OC}(SOC)$ can be represented entirely using a monotonic polynomial curve while the bulk force $F(SOC)$ is clearly a non-monotonic function.

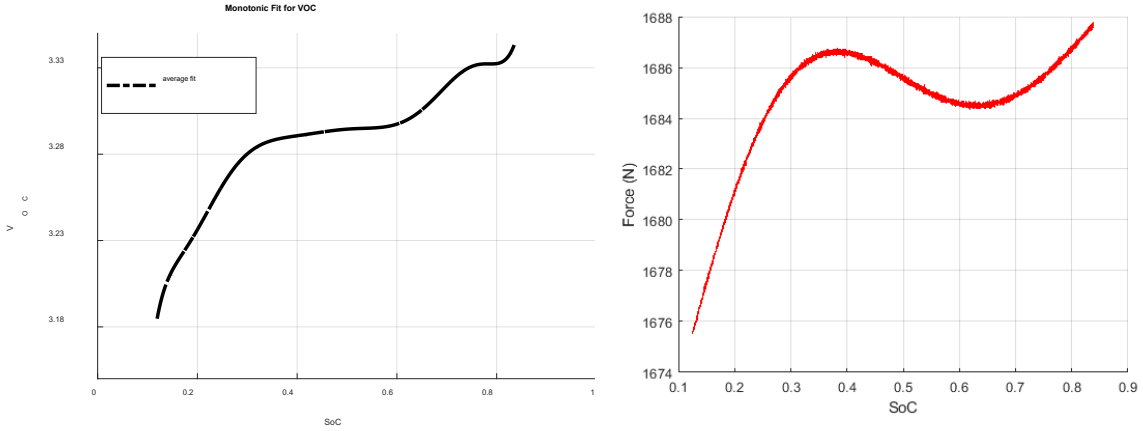

(a) Monotonic fitted curve for Voc (b) Bulk force based on SoC

Figure 3-3. Output functions for the battery system

3.3 Nonlinear Observer Design

3.3.1 Nonlinear Observer for Bounded Jacobian Output Functions

For the plant model given by equations (3.8)-(3.9), the following nonlinear observer is proposed:

$$\dot{\hat{x}} = A\hat{x} + Bu + L[y - C\hat{x} - h(\hat{x})] \tag{3.10}$$

Let the estimation error be $\tilde{x} = x - \hat{x}$. Then the estimation error dynamics obtained by subtracting equation (3.10) from (3.8) is

$$\dot{\tilde{x}} = (A - LC)\tilde{x} - L[h(x) - h(\hat{x})] \tag{3.11}$$

The presence of the nonlinear function $h(x) - h(\hat{x})$ in equation (3.11) means a linear observer cannot ensure globally stable estimation for this nonlinear system. It is clear that the system is linear in the process dynamics and has nonlinear measurement equations. Furthermore, the nonlinear functions in the output (measurement) equations are smooth and differentiable with bounded slopes at every operating point. Hence, a nonlinear observer design method that allows a nonlinear function in the output equations and uses the lower and upper bounds on the Jacobian of this nonlinear function is utilized [47]. The

key observer design result that will be utilized is as follows:

Theorem 3.1. Let K_1 and K_2 be the lower and upper bounds of the Jacobian of the nonlinear function $h(x)$ of equation (10), so that the (i,j)th elements of the matrices K_1 and K_2 satisfy

$$K_1(i,j) \leq \frac{\partial h_i}{\partial x_j} \leq K_2(i,j) \tag{3.12}$$

If the observer gain matrix L and a positive definite matrix P are determined such that they satisfy the following linear matrix inequalities

$$P > 0 \tag{3.13}$$

$$\begin{bmatrix} (A-LC)^T P + P(A-LC) + \sigma P & -PL \\ -L^T P & 0 \end{bmatrix} - \begin{bmatrix} \frac{K_1^T K_2 + K_2^T K_1}{2} & -\frac{K_1^T + K_2^T}{2} \\ -\frac{K_1 + K_2}{2} & I \end{bmatrix} < 0$$

Then the observer given by equation (3.10) is exponentially stable, with an exponential convergence time constant of at least σ.

Proof: This result is a straightforward use of a previous nonlinear observer design method from a theoretical publication of our research group [47]. From Theorem 2.1 of [47], if

a) the nonlinearity in the process dynamics is set to zero (i.e. $f(x) = 0$),
b) the output error injection in the output nonlinearity is removed (i.e. $L_2 = 0$) and
c) the Lyapunov asymptotic stability condition $\dot{V} < 0$ is replaced by the exponential convergence rate condition $\dot{V} < -\sigma V$,

then the observer design condition of equation (16) can be obtained quite easily.

3.3.2 Non-existence of a Stable Observer Due to Non-Monotonicity

Theorem 3.2. If the nonlinear functions in $h(x)$ are non-monotonic, then a constant observer gain L that satisfies equation (3.13) cannot exist.

Proof: Part 1: In this part, we show that the linear portion of the estimation error dynamics is NOT stable in this application and can never be stabilized, no matter how the observer gain L is chosen. Hence the nonlinear output functions are needed for stabilization. For applying Theorem 3.1, the system matrices in this application are

$$A = \begin{bmatrix} -\frac{1}{R_1C_1} & 0 & 0 \\ 0 & -\frac{1}{R_2C_2} & 0 \\ 0 & 0 & 0 \end{bmatrix}, \quad B = \begin{bmatrix} \frac{1}{C_1} \\ \frac{1}{C_2} \\ -\frac{1}{C_b} \end{bmatrix},$$

$$h(x) = \begin{bmatrix} V_{oc}(SOC) \\ F(SOC) \end{bmatrix}, \quad C = \begin{bmatrix} -1 & -1 & 0 \\ 0 & 0 & 0 \end{bmatrix}$$

Let the observer gain be

$$L = \begin{bmatrix} \ell_{11} & \ell_{12} \\ \ell_{21} & \ell_{22} \\ \ell_{31} & \ell_{32} \end{bmatrix}$$

Then

$$A - LC = \begin{bmatrix} -\frac{1}{R_1C_1} - \ell_{11} & -\ell_{11} & 0 \\ -\ell_{21} & -\frac{1}{R_2C_2} - \ell_{21} & 0 \\ -\ell_{31} & -\ell_{31} & 0 \end{bmatrix}$$

Hence $(A - LC)$ has one eigenvalue at 0 and is NOT asymptotically stable, no matter how L is chosen. It can also be easily checked that (A, C) is undetectable. Hence, the linear portion of the output cannot stabilize the dynamics and the nonlinear function in the output is needed for stabilization.

Part 2: If the nonlinear output function $F(SOC)$ is non-monotonic, then

$$K_1 = \begin{bmatrix} 0 & 0 & \left.\frac{\partial V_{oc}}{\partial (SOC)}\right|_{min} \\ 0 & 0 & \left.\frac{\partial F}{\partial (SOC)}\right|_{min} \end{bmatrix} \tag{3.14}$$

and

$$K_2 = \begin{bmatrix} 0 & 0 & \left.\frac{\partial V_{oc}}{\partial (SOC)}\right|_{max} \\ 0 & 0 & \left.\frac{\partial F}{\partial (SOC)}\right|_{max} \end{bmatrix} \tag{3.15}$$

Hence

$$K_1^T K_2 = K_2^T K_1$$

$$= \begin{bmatrix} 0 & 0 & & 0 \\ 0 & 0 & & 0 \\ 0 & 0 & \left\{\frac{\partial V_{oc}}{\partial(SOC)}\Big|_{min}\right\}\left\{\frac{\partial V_{oc}}{\partial(SOC)}\Big|_{max}\right\} + \left\{\frac{\partial F}{\partial(SOC)}\Big|_{min}\right\}\left\{\frac{\partial F}{\partial(SOC)}\Big|_{max}\right\} \end{bmatrix}$$

The force measurement nonlinear functions in $h(x)$ $F(SOC)$ is non-monotonic, so that $\frac{\partial F}{\partial(SOC)}\Big|_{min} < 0$ and $\frac{\partial F}{\partial(SOC)}\Big|_{max} > 0$.

Also, the $V_{oc}(SOC)$ curve has almost zero sensitivity in some portions of the SOC range, so that the minimum slope

$$\frac{\partial V_{oc}}{\partial(SOC)}\Big|_{min} = 0.$$

Further, $\frac{\partial V_{oc}}{\partial(SOC)}\Big|_{max} > 0$.

Hence, from (17) and (18), $K_1^T K_2 + K_2^T K_1 \leq 0$. This implies

$$\begin{bmatrix} (A-LC)^T P + P(A-LC) + \sigma P & -PL \\ -L^T P & 0 \end{bmatrix} - \begin{bmatrix} \frac{K_1^T K_2 + K_2^T K_1}{2} & -\frac{K_1^T + K_2^T}{2} \\ -\frac{K_1 + K_2}{2} & I \end{bmatrix} < 0$$

if and only if $\begin{bmatrix} (A-LC)^T P + P(A-LC) + \sigma P & -PL \\ -L^T P & 0 \end{bmatrix} < 0.$

In turn, this is possible if and only if

$$(A-LC)^T P + P(A-LC) + \sigma P < 0 \qquad (3.16)$$

But, if $(A-LC)$ is NOT asymptotically stable for any L (from part 1), then a solution to equation (3.16) can never exist.

Hence, this nonlinear observer cannot be stable with a constant observer gain, if the nonlinear function is non-monotonic.

3.4 Hybrid Nonlinear Observer Design

From the theoretical results in section 3.3 (Theorem 3.2), we have seen that since the output function $F(SOC)$ is non-monotonic, we cannot find a feasible solution to the

observer design Linear Matrix Inequality (LMI) (3.13). Attempts in MATLAB to find an LMI solution that works over the entire SOC range of the battery failed, i.e. no feasible solutions to (3.13) existed for the output functions shown in Figure 3-4. The MATLAB evaluations thus reconfirmed the theoretical result of the output functions being required to be monotonic.

With the monotonicity requirement in mind, the SOC range of the battery can be divided piecewise into different regions in a manner such that in each region the load cell force $F(SOC)$ function is a monotonic function. Such a piecewise division of the SOC range into regions R_1 to R_5 is shown in Figure 3-4. Note that the boundaries of the regions lie at the slope change points of the force output function. For example, R_4 is a narrow region in which the slope of the output y_2 is close to zero. In this region, only the output y_1 will be used by the observer, since y_2 is non-monotonic in this region. Regions R_3 and R_5 lie on either side of R_4 and both of these regions can utilize both outputs y_1 and y_2. Both y_1 and y_2 are monotonic in these regions.

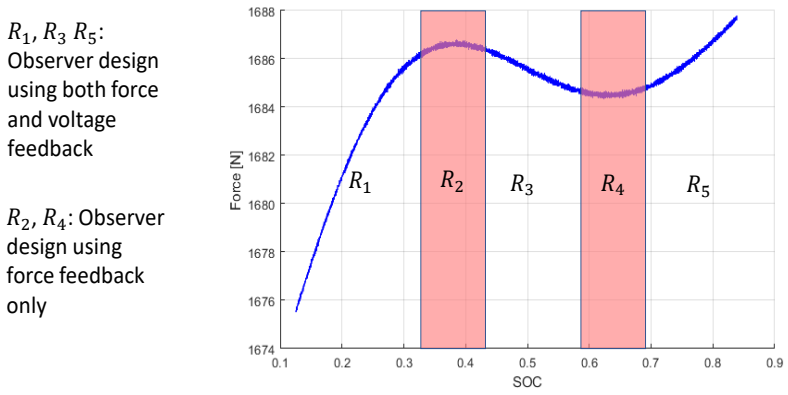

Figure 3-4. Creating regions around slope-change points of bulk force output function

It should be noted that we have the liberty of relying on only one of the output measurements in the narrow regions with zero slope, because even with one output the system is still observable, although the result of estimation will not be as accurate as the case when we use both outputs, due to the low sensitivity of $V_{oc}(SOC)$. Hence, the width of these regions was kept narrow so as to minimize regions in which only 1 output is used by the observer. While it is ideal to have these regions to be as narrow as possible, in practice their width is determined by the accuracy of the measurement models. For example, if we anticipate a considerable horizontal uncertainty or shift in the output

functions, we are forced to sacrifice the estimation accuracy for the sake of stability by widening the low observability regions.

A switched gain observer is developed using the regions defined in Figure 3-4. As shown in Figure 3-5, the switched gain observer uses different gains in each of the discrete piecewise regions. Since each region R_1 through R_5 has monotonic output function properties, a constant stabilizing observer gain exists in each of these regions. As the operating region changes, the observer gains switch in value accordingly using a finite state machine of the type shown in Figure 3-5.

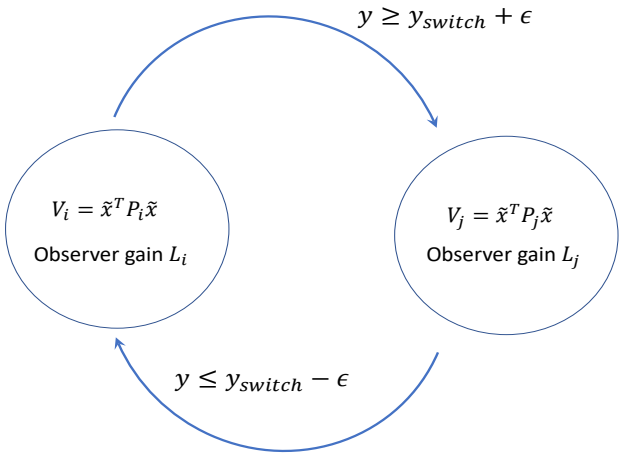

Figure 3-5. Creating regions around slope-change points of output functions

In Figure 3-5, region i has the observer gain L_i which has been designed using the LMI of equation (3.13) and the corresponding value of the Lyapunov positive definite matrix P_i. Likewise, region j has the observer gain L_j and the positive definite Lyapunov function matrix P_j.

The stability of the hybrid observer of Figure 3-5 consisting of different constant observer gain regions needs to be considered. It should be noted that inside each region, a single observer gain is used and therefore exponential stability is guaranteed inside this region using the Lyapunov function analysis of Theorem 3.2. However, different regions i may have different values of the matrix $P_i > 0$ in their individual Lyapunov functions. The stability of the overall switched system can be guaranteed if the system satisfies a minimum dwell time constraint in each region, according to results from hybrid system theory [48]. The minimum dwell time in region j when switching from region i to region j needs to be

greater than T where T is the amount of time needed for $V_j(x(t+T)) < V_i(x(t))$. This minimum dwell time guarantees global asymptotic stability.

This result can be understood as follows: In each individual region, the estimation error $\tilde{x}$ keeps decreasing due to the Lyapunov exponentially stable design in that region. In switching between regions, the P matrix may be different in the two regions. However, if the system remains in the same region for a minimum dwell time, the error will become smaller than the initial value at the time the region was entered (due to local exponential stability). Thus, if the system is constrained to remain in one region for a minimum dwell time, the value of the Lyapunov function after the dwell time in region j is less than its value in region i at the time the switch from i to j occurred. This guarantees overall asymptotic stability as was shown in Theorem 2.5.

In the case of the observer design application for the SOC estimation system, the values of y at which the region is entered and at which it switches back are different (as shown in Figure 3-5). This hysteresis between entering and switching back ensures that the minimum dwell time constraint is met.

One obstacle that could affect the performance of this piecewise nonlinear observer is the initial condition. If we pick the initial condition to be in the wrong region (with the wrong observer gain), it might result in a divergence of the observer estimates. However, thanks to the specific shape of output functions for this application, there is an easy solution that can remedy this shortcoming. From Figure 3-3, since there is a one-to-one relationship between the SOC and the ordered output pair that is constructed by the two output functions y_1 and y_2, we can identify the correct region for the initial condition accurately.

3.5 Simulation Results

3.5.1 Nominal Simulations (No model uncertainty in measurement equations)

The estimated SOC from the nonlinear observer is shown in Figure 3-6 along with the actual SOC for the charge-discharge cycles of Figure 3-2. As is clear in the figure, the estimated SOC follows the actual values very closely. There are regions in the estimation curve, however, with some apparent deviations from the real value; these are the regions

where the observer is only using the terminal voltage in the measurements equation and it is discarding the bulk force measurements that are available (regions R_2 and R_4 around the slope-change points in Figure 3-5). It is expected that neglecting one of the measurements will reduce the accuracy of the estimation, especially since the only measurement that's being used in these regions contains hysteresis.

Figure 3-8 shows the error in estimation defined as the difference between the estimated and actual SOC values. The regions where only the terminal voltage is being used is also visible here. The RMS of the error is 0.011 and, ignoring the initial condition, part the maximum error is seen to be 0.036.

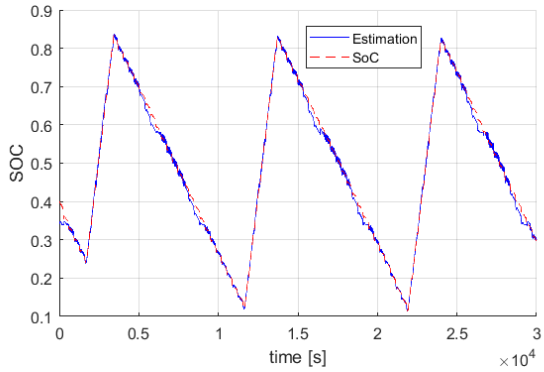

Figure 3-6. Estimated SOC from nonlinear observer along with actual SOC

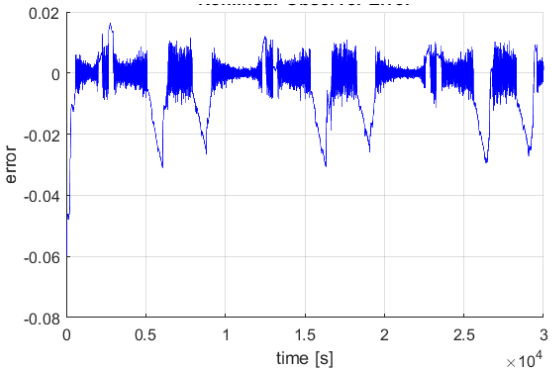

Figure 3-7. Estimation error of the observer

3.5.2 Alternative Observer with Open-loop Estimation within the Bands

As was stated earlier, the largest amount of error occurs in the bands where the

nonlinear observer relies solely on the terminal voltage. One simple solution to this problem is to ignore the measurement altogether in these regions, and instead just use the dynamic equations. This open loop observer is frequency referred to as the coulomb counting method in the literature. The results of using such a scheme are illustrated in Figure 3-8. It can be seen that using the open loop observer within the slope-change bands improves the estimation in these regions and the RMS of the error has been reduced to 0.007 and the maximum error to 0.02.

It is to be noted, however, that this result is achievable only because of the assumed high accuracy of the dynamic equations (since we are using synthetic measurements with miniscule added noise and bias). Had the bias in current measurement been bigger or were there some larger noise or model uncertainty within the data, this method would have provided deteriorated estimation. In addition, the stability of the observer is no longer guaranteed in this case.

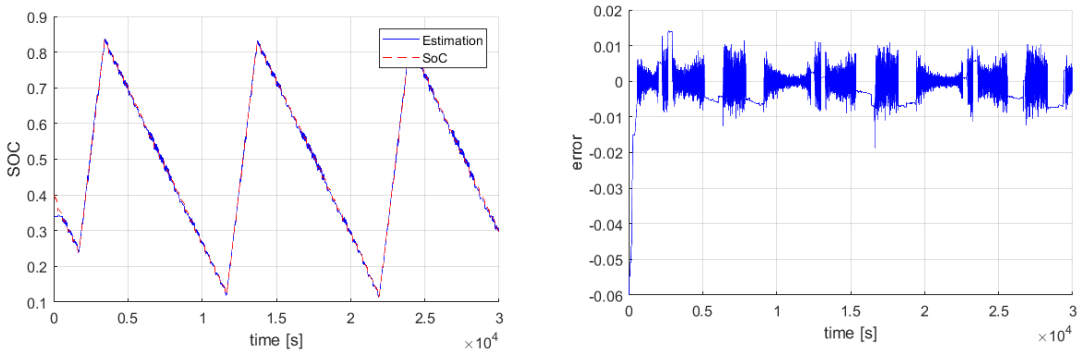

Figure 3-8. Estimated SOC and estimation error of observer where the estimation is done open loop within the slope-change regions

3.5.3 Estimation using an Extended Kalman Filter

The Extended Kalman Filter can also be used to estimate the SOC of the nonlinear lithium-ion battery system. The result is presented in Figure 3-9. The estimation is very accurate which is expected since the synthetic added noise is Gaussian and the extended Kalman filer is close to optimal in this situation. This will not be the case when actual experimental measurements are used and model uncertainty is present. The other issue is that, unlike nonlinear observers, there is no proof of global asymptotic stability in this case. As we will see later, the filter might become unstable with the introduction of model error.

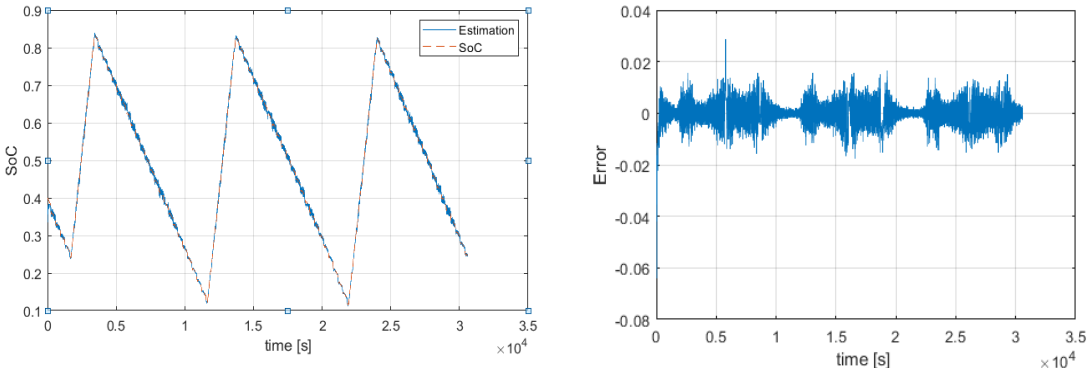

Figure 3-9. Results of EKF estimation

3.6 EKF Instability in the Presence of Model Error

This section describes the influence of model error on both the EKF and the nonlinear observer. It will be seen that even small model errors cause the EKF to become unstable due to the non-monotonic nature of the output functions. The nonlinear observer continues to be stable in all cases. The types of model errors used in the simulations here are exactly the variations that would be induced by aging in the battery [49], [50].

1) Gain Error in Force: Here the force-SOC curve was slightly scaled from the model value using F=F*1.0001. This is just a 0.1% error in the scaling factor of the output. It is an extremely small error in gain, as seen in Figure 3-10. However, this small error causes the EKF to diverge significantly from the real SOC values.

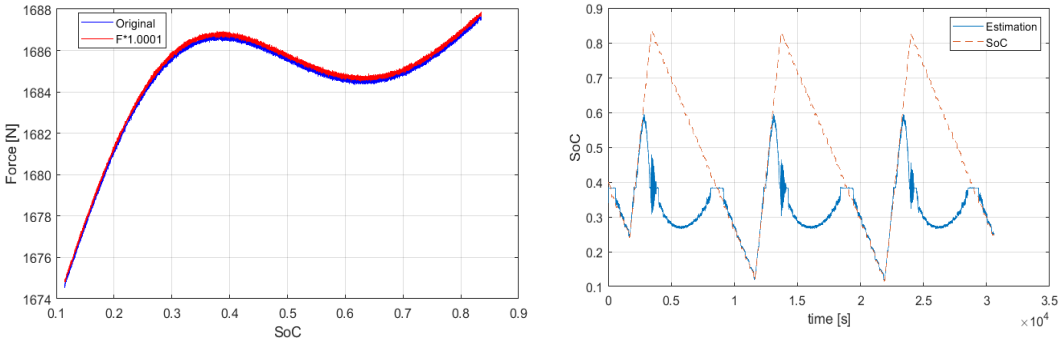

Figure 3-10. Results of EKF estimation with scaling factor error of 0.1%

It can be seen that the EKF diverges significantly as the SOC value approaches 0.6 (i.e. the slope change point) and then takes a very long time to converge back to the correct

estimates. The return to convergence happens after the slope changes again at a SOC of approximately 0.3. The nonlinear observer, on the other hand, never becomes unstable and continues to perform well through the entire range of SOC values, as seen in Figure 3-11.

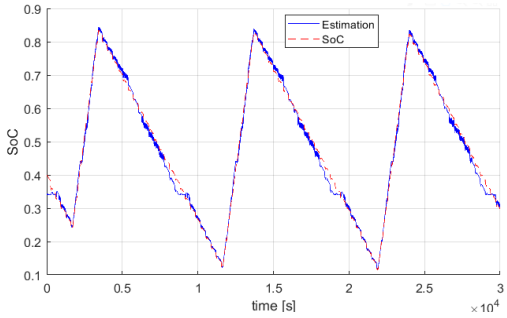

Figure 3-11. Results of nonlinear observer estimation with scaling factor error of 0.1%. The rms error is 0.015

2) Offset error in SOC: An offset of 0.05 is added to the force-SOC relationship, using F=f(SOC+0.05).

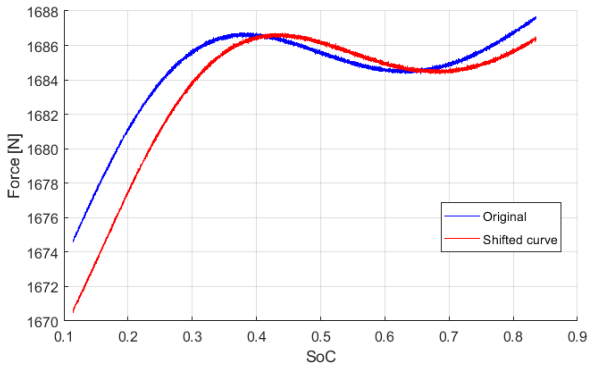

Figure 3-12. Force output curve with a lateral shift in SOC of 0.05

The resulting difference between the actual and modeled force-SOC curves is seen in Figure 3-12. Again, the EKF diverges for this model error scenario and never converges back. Hence its simulation results are not explicitly shown here. The performance of the nonlinear observer for this same model error scenario is shown in Figure 3-13 (a) and (b). Again, the nonlinear observer remains stable through the entire charging-discharging scenario (Figure 3-13(a)), and it rms error as seen in Figure 3-13(b) is only 0.0521, even with this model error.

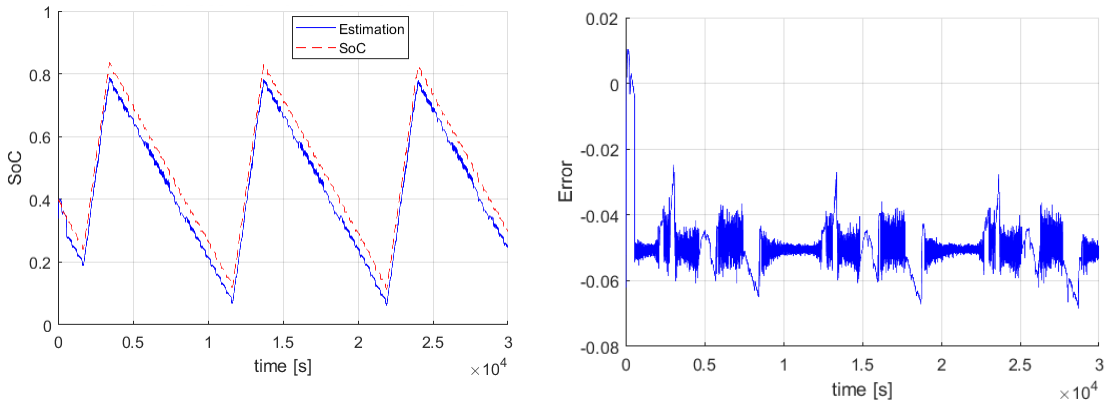

Figure 3-13. Results of nonlinear observer estimation with lateral offset in SOC

3) Model Error at Slope-Change Points: Minor errors in the slope change points were introduced by slightly modifying the polynomial models for the force-SOC curves. The errors introduced can be seen in Figure 3-14.

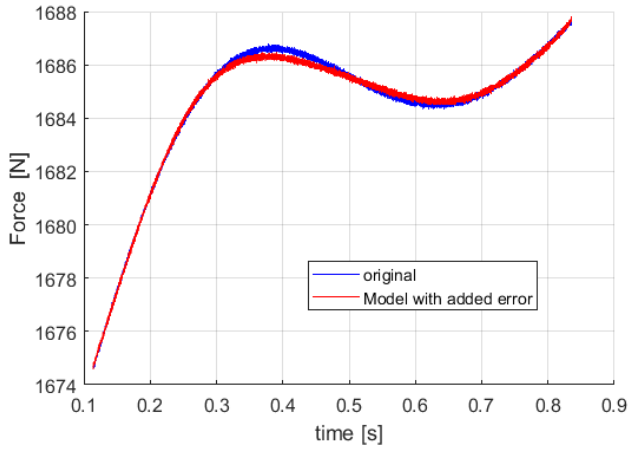

Figure 3-14. Error in slope-change points of force-SOC curve

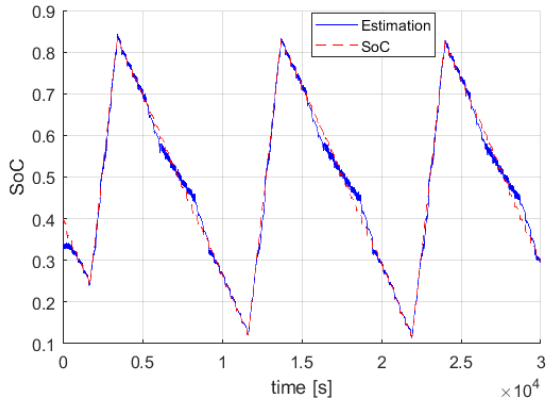

Figure 3-15. Results of nonlinear observer estimation with error in slope-change points

Again, the EKF estimates diverge significantly from the actual SOC values, and are therefore not shown. On the other hand, the nonlinear observer continues to remain stable and performs accurately, as seen in Figure 3-15.

3.7 Robustness to Initial Condition Errors

For the hybrid nonlinear observer to be guaranteed to remain stable, the region of the initial condition needs to be identified correctly, so that the correct initial observer gain is chosen. If the initial region is identified incorrectly, then the use of the wrong observer gain can lead to instability. One way to identify the initial region is based on the measured values of the two ordered outputs, i.e. force and terminal voltage. Figure 3-16 shows how the initial condition can be identified to be in one of 5 regions, based on the values of force and voltage. For simplicity and a test of robustness, the observer assumes that the initial condition is the midpoint of the region which has been identified as the initial region. Starting from this initial value, the estimates will converge to the correct values due to the stability of the observer. Two examples with different initial conditions are presented below in Figure 3-17. Note that due to the fast convergence of the observer, the initial condition error can only be seen as a very short spike at time zero in some of the plots. As can be seen, when the initial point is in one of the regions where the observer is using both output functions (Figure 3-17 a), the observer converges to the correct SOC value almost instantaneously. But when the simulation starts from a region where only the voltage is being used (Figure 3-17c), since the sensitivity of the output function is very limited, the convergence takes longer to happen. Even in this case the estimation error will always stay bounded within the region.

While the width of the regions (bands) with solely voltage output was broadly assumed to be 0.1 of SOC here, in practice it can be minimized based on the accuracy of the bulk force model in experimental data, and hence the convergence can be improved. Furthermore, gridding the domain, instead of picking the middle point of the entire region as the unknown initial condition, could further improve the convergence in the regions with limited sensitivity.

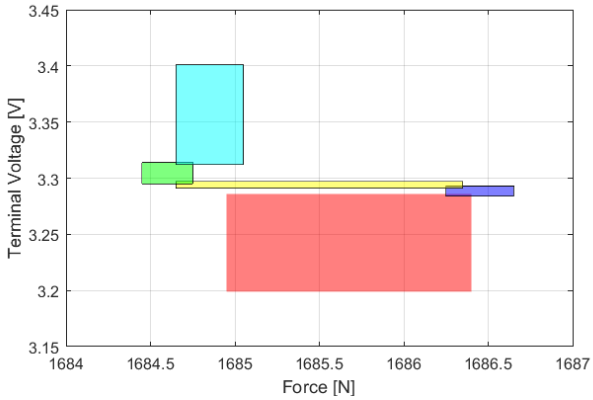

Figure 3-16. The values of force and terminal voltage determine operating region and the related initial condition. Depending on the accuracy of the force and voltage measurements there could be small areas which are shared between two regions and could have either of the initial conditions.

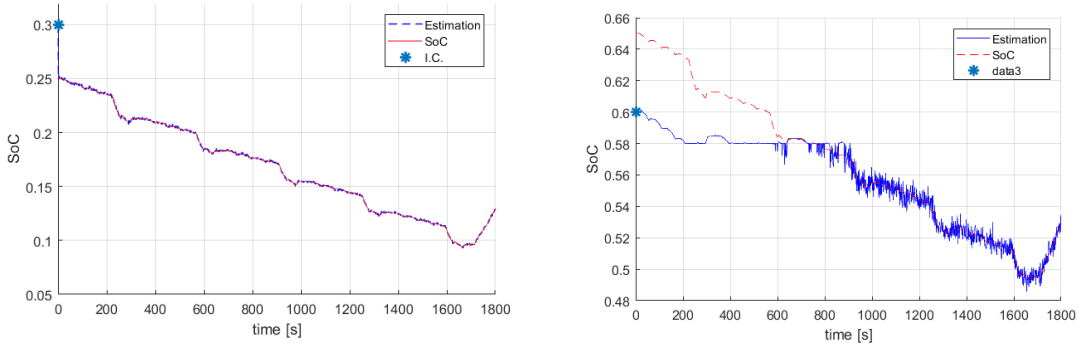

(a) (b)

Figure 3-17. SOC estimation and true value for different initial conditions. (a) Initial SOC=0.25, Initial observer guess=0.3 (b) Initial SOC=0.65, Initial guess: 0.6

Depending on the accuracy of measurement, we might have intervals in which the initial condition could belong to either of two neighboring regions (Figure 3-16). By picking the observer gains conservatively, we can ensure that choosing either of the regions would guarantee stability.

A more robust initial condition determination method can be obtained if the numerical first and second order derivatives of the outputs are used, in addition to their raw values. Since change in SOC happens very slowly, numerical values of first and second derivatives can be obtained accurately using a few time samples of data, if the sampling frequency is fast.

3.8 Experimental Performance

The developed nonlinear observer and the EKF were both evaluated using experimentally measured data from the University of Michigan battery test rig instrumented with sensors that measure terminal voltage, current and load cell force. A small bias error was added to the current signal to represent an inexpensive current sensor that would normally be available on a commercial battery.

Figure 3-18 shows the force as a function of SOC for the battery during a number of charge-discharge cycles. The charge-discharge cycles can be seen in Figure 3-19. While the experimental force-SOC curve in Figure 3-18 clearly shows a hysteresis type of phenomenon, the curve is modeled using just a single polynomial without hysteresis (shown by the dashed red curve in the figure).

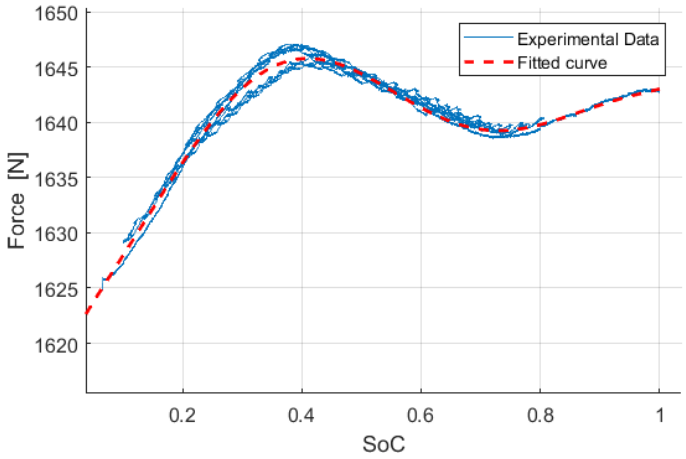

Figure 3-18. Measured experimental force-SOC curves and corresponding single polynomial model

Figure 3-19 shows the performance of the nonlinear observer in estimating the SOC. It can be seen that the SOC is estimated quite well in spite of the large hysteresis error in the force-SOC model (as well as in the $V_{oc}(SOC)$ model). The error is typically seen to be within 2% for most of the operation, but rises to have a spike of 6% at the points where a switch from charging to discharging, or vice-versa, occur (due to hysteresis).

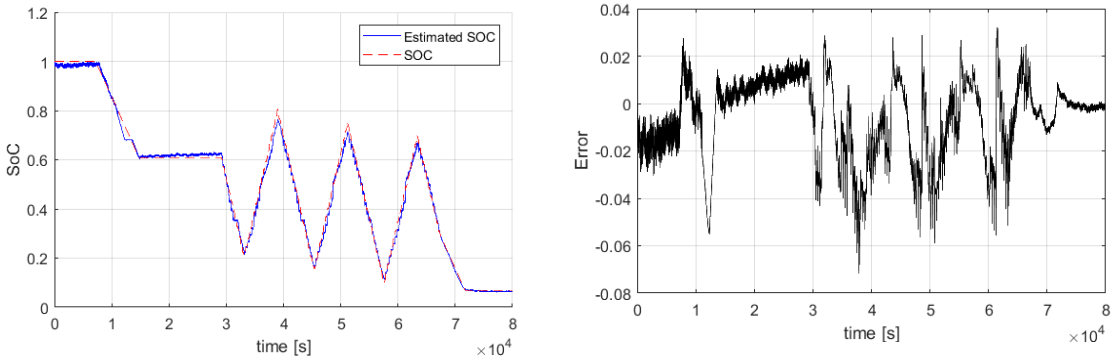

(a) (b)

Figure 3-19. Actual and estimated SOC with nonlinear observer during charge-discharge cycles

The performance of the nonlinear observer can be compared with that of the EKF which is seen in Figure 3-20. Due to the hysteresis and the error in the zero-slope points of the model versus the actual data, the EKF diverges completely from the actual SOC, just as it did in the simulations.

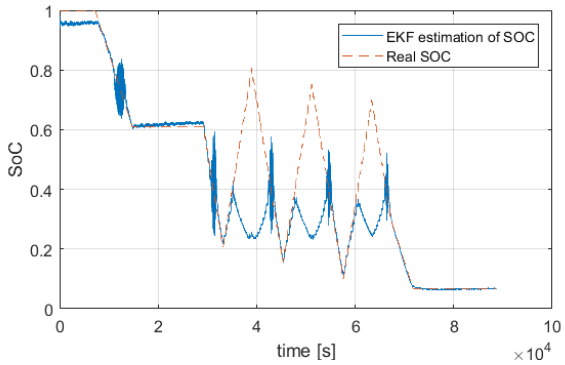

Figure 3-20. Divergence of EKF for the experimental data

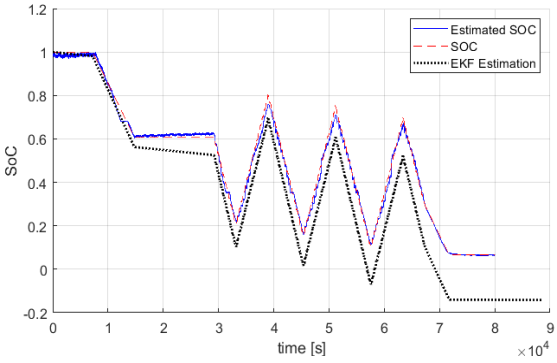

Figure 3-21. Estimates of the nonlinear observer and of the EKF in the presence of measurement bias, when sensor noise covariances are chosen to be extremely large for the EKF

To prevent the EKF from divergence, the sensor noise covariances during EKF design can be highly amplified so that the EKF feedback gain will be very small and the EKF estimation will largely rely on the model rather than on sensor feedback. This aspect is shown in Figure 3-21. Here it can be seen that the EKF estimates no longer diverge from the actual SOC values. However, they do suffer from a drift due to the small bias error in current measurement and no corrections from the output due to high sensor noise covariance. The nonlinear observer is not affected by the current bias error because it continues to use the voltage and force measurements and relies not only on the model but also on the sensor measurements.

3.9 Conclusions

This chapter developed a hybrid nonlinear observer for state of charge (SOC) estimation in a lithium ion battery, using measurements of terminal voltage and bulk force. While both outputs are nonlinear functions of SOC, the force is a highly non-monotonic function. The non-monotonicity of the force-SOC curves poses a special challenge for observer design.

The basic nonlinear observer for this system was designed using Lyapunov analysis relying on lower and upper bounds of the Jacobian of the nonlinear output function. Rigorous analysis showed that the proposed nonlinear observer can only have feasible design solutions when the output is monotonic (i.e. in each piecewise monotonic region of the output function). It has no constant feasible solution when the entire SOC range is considered. The non-monotonicity challenge was then addressed by designing a hybrid nonlinear observer that switches between several constant observer gains. In each constant-gain region, the observer is designed to be stable using a Lyapunov function and an LMI-based design technique. The overall stability of the switched system is guaranteed by ensuring overlap between regions and an adequate dwell time between switches.

The performance of the observer was evaluated first through simulations using a high-fidelity battery model and then through experiments. The performance of the nonlinear observer was compared with that of an extended Kalman Filter, which would traditionally

be used for SOC estimation. Simulation results with the high-fidelity model showed that with no model uncertainty and not accounting for hysteresis, the nonlinear observer provides estimates with an RMS error of 1.1% and a maximum error of 3.6%. The EKF performs better when there is NO model error, providing an RMS error less than 1% and a maximum error of only 2%. However, it has continuously varying gains, unlike the nonlinear observer which switches between only five constant gains.

The nonlinear observer shines when model error is introduced into the system. In the presence of model error in slope change points, the EKF becomes unstable for even very small errors in the output curves. The nonlinear observer, on the other hand, continues to perform very well, providing accurate estimates and never becoming unstable.

The experimental results verified the observations from simulation and the EKF was found to become unstable due to model errors even in the experimental data, while the hybrid nonlinear observer continued to work reliably for this SOC estimation problem.

Chapter 4
Magnetic Position Estimation Using Optimal Sensor Placement and Nonlinear Observer for Smart Actuators

4.1 Introduction

Magnetic position estimation offers an inexpensive and non-contacting method of obtaining piston position in many modern piston-cylinder systems, including pneumatic cylinders, hydraulic actuators and IC engines. In magnetic position estimation, a magnet is placed on the moving object, such as the moving piston shown in Figure 4-1. A sensor board containing one or more magnetic sensors is placed on the outside cylinder, again as shown in Figure 4-1. Such magnetic sensors enable non-contact estimation of position of the piston. Traditional sensors such as potentiometers and LVDTs require the sensor to be connected co-axially to the moving piston. This requires significant installation effort, results in contacting motion and in shear loads on the sensor during operation, often resulting in sensor failure. Furthermore, potentiometers and LVDTs can be much more expensive than the magnetic sensors considered in this chapter.

Humans have long used a magnetic compass for navigation for hundreds of years [51]. Currently, magnetic sensors are also widely used in a number of attitude estimation applications utilizing orientation with respect to the Earth's magnetic field [52], [53].

However, magnetic fields have mostly been utilized for linear position sensing only in the case where the movement between the magnet and magnetic sensor is very small (a few mm), using either hall-effect [54], or eddy current sensors [55].

While some magnetic sensors, such as AMR and TMR sensors, are highly sensitive and can measure magnetic fields at large distances from the magnet, there is an inherent problem due to the nonlinear and non-monotonic nature of the magnetic field [56]. The magnetic field of a magnet varies as a highly nonlinear function of position.

Nonlinear observer design is a topic of significant interest in the control systems community. Powerful observer design methods that have been developed for nonlinear systems include methods that assume that either the nonlinear dynamics are Lipschitz, sector bounded, or have lower and upper bounds on their Jacobians [24], [57], [11], [9].

A limitation of the previously developed observer design methods is that the output equation is typically assumed to be linear (even though the process dynamics are nonlinear). The argument cited by researchers in favor of this assumption is that a coordinate transformation can be used to convert algebraic nonlinear output equations into linear equations. However, a practical investigation shows that using coordinate transformations for the purpose of making output equations linear can be a complicated approach. This is especially because the nonlinear output equations may not be easily invertible. Further, it has not been recognized much in literature that when the output equation is both nonlinear and non-monotonic, then a constant observer gain for stabilization simply does not exist. This chapter focuses on developing an observer design method for the magnetic position estimation application which involves a nonlinear system with nonlinear output equations. In particular, the situation where the output is a non-monotonic nonlinear function is considered. A non-monotonic system poses a problem for observer design because a constant observer gain that stabilizes the system over the entire range of operating conditions may not exist for such a system, as discussed in this chapter. Non-monotonic nonlinear output equations are encountered in magnetic position estimation, in state-of-charge estimation [32] and in vehicle trajectory tracking applications [58].

After that, this chapter takes the question of optimal sensor placement into consideration and tries to address it by solving an optimization problem that maximizes the

minimum singular values of the observability matrix. Optimization of sensor position has been previously analyzed in different physical fields such as target tracking [59], system identification [60], and airfoil wake estimation [61].

Here we try to use the same philosophy for our position sensing magnetometers. In such problems, normally the goal is to improve position estimation accuracy, i.e. we need to minimize the estimation error in in the system. To minimize the estimation error, it is customary to minimize one of the measures of unobservability [62]. Among those measures the observability matrix, the Fisher information matrix, and the observability Gramian could be named. As is apparent, all of these measures are in matrix form and hard to work with, so normally a sacralization function like determinant or minimum eigenvalue is applied to them to make them more numerically accessible.

In this chapter we focus on the observability matrix and choose its minimum singular value as the sacralization function. After formulization of the optimization problem and solving it, we use experimental data to show the optimality of the found sensor placement. In a related conference paper [29], we presented the basic nonlinear observer design algorithm. However, extensive experimental results and the sensor location optimization results have now been added. Furthermore, the nonlinear observer design method has been generalized and more degrees-of-freedom introduced into the design algorithm.

The outline of this chapter is as follows. Section 4.2 summarizes the magnetic position estimation method. Section 4.3 describes the theoretical problem formulation and develops the improved theoretical results on the observer design procedure for the nonlinear output equations system. Section 4.4 describes the application of the developed theory to linear position estimation in smart piston-cylinder actuators. Section 4.5 presents a piecewise observer design methodology that enables stable observers for systems with non-monotonic output functions. Section 4.6 presents experimental results obtained using the developed theoretical tools. Section 4.7 addresses the optimization problem. Conclusions are presented in section 4.8.

4.2 Magnetic Position Estimation

For the estimation of linear position, we use the magnetic fields of a permanent magnet located on the piston, as shown in Figure 4-1. In electrohydraulic actuators there is typically already such a magnet attached to the piston which generates a magnetic field that can be sensed by reed switches (binary switches that detect if the piston has crossed a stroke limit point). The same magnet is now used by the nonlinear observer to continuously monitor the real-time position of the piston (not just whether it has reached the end of stroke). The magnet has a magnetic field which varies nonlinearly with position. By measuring the magnetic field with the magnetic sensors and using an observer, the position of the piston can be estimated.

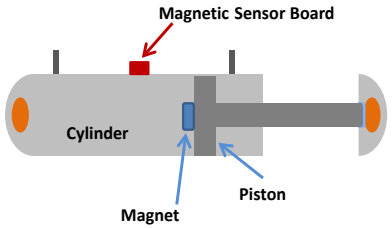

Figure 4-1. Sensor Configuration for position estimation of EHA

In this chapter, we thus utilize the effect of change in magnetic field with the change in distance from a magnet. For a simple dipole this effect is known and can be presented as (Figure 4-2):

$$B_r = \frac{B_0}{2\pi r^3}\cos\alpha$$

$$B_\alpha = \frac{B_0}{4\pi r^3}\sin\alpha$$

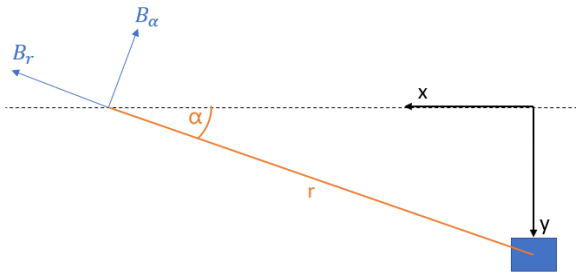

Figure 4-2. Magnetic field of a magnet

In our set up, however, the magnet and its magnetic field are more complicated due to the fact that magnet is not just a point dipole, but has a non-zero radius and thickness. Hence, empirical curve fits to the magnetic fields as functions of position are used for the output model. An illustration of these curves can be seen in Figure 4-5.

The next problem would be designing an observer to estimate the position. One could propose that by inverting the output functions the position could be found as an algebraic function of the two magnetic fields. In practice, however, there are two issues associated with this suggestion. First, finding the algebraic function that can convert the magnetic fields into position is non-trivial. Due to the complicated and non-monotonic nonlinear shape of the magnetic fields, the functions are not easily invertible. Second, and more importantly, directly inverting these nonlinear curves results in highly noisy position estimates due to portions of the curves having very low sensitivity of the magnetic field changes with position. An illustration of the attempt to estimate position by inverting the magnetic curves is shown in Figure 4-3. This method leads to many large spikes in the position estimates, as can be seen in Figure 4-3 . Therefore, we need to use a good estimation algorithm, such as a nonlinear observer, to achieve our purpose.

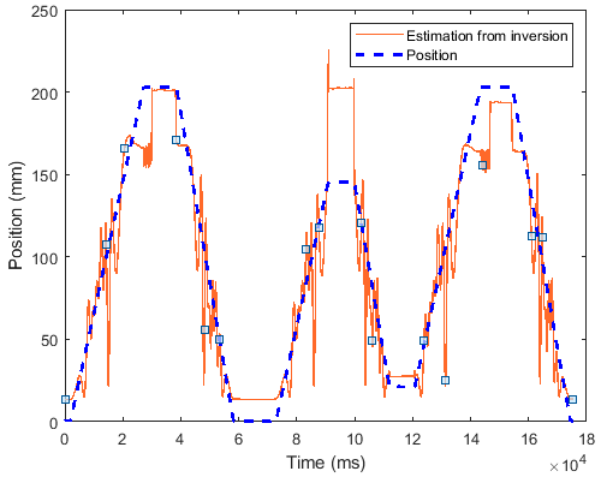

Figure 4-3. Estimated position from direct inversion method

4.3 Observer Design for Systems with Nonlinear Output Equations

4.3.1 Problem Formulation

Consider the class of systems described by the following equations (4.1)-(4.2)

$$\dot{x} = Ax + Bu \tag{4.1}$$

$$y_i = h_i(C_i x) \tag{4.2}$$

with $x \in R^n$ being the state vector, $u \in R^p$ representing the input, $C_i \in R^{1 \times n}$, $h_i: R \to R$, $i = 1,2, \dots, m$ signifying the output functions, and the other matrices being of appropriate dimensions. Thus, there are m outputs and all of them are nonlinear functions of different scalar variables $C_i x$. Each output is assumed to be a function of a scalar variable because the non-monotonicity of the output function is shown to provide a significant challenge in observer design. An output can be described as being a monotonic or non-monotonic function of its argument, only if the argument is a scalar, rather than being vector-valued. Now, define the matrix

$$C = \begin{Bmatrix} C_1 \\ \vdots \\ C_m \end{Bmatrix} \tag{4.3}$$

and define the output vector y using

$$y = Cx = \begin{Bmatrix} C_1 \\ \vdots \\ C_m \end{Bmatrix} x \tag{4.4}$$

with $C \in R^{m \times n}$ and $y \in R^{m \times 1}$.

Further, let $M = \text{diag}(M_1, M_2, \dots, M_m)$ be a diagonal matrix containing the lower bounds of the partial derivatives of $h_i(C_i x)$ and let $N = diag(N_1, N_2, \dots, N_m)$ be a diagonal matrix containing the upper bounds of the same partial derivatives:

$$M_i \leq \frac{\partial h_i}{\partial (C_i x)} \leq N_i \tag{4.5}$$

The nonlinear function will be considered to be monotonic if its derivative is always positive or always negative, i.e. M_i and N_i both have the same sign. If an output equation is non-monotonic, then the corresponding M_i and N_i have opposite signs.

Let the observer be given by

$$\dot{\hat{x}} = A\hat{x} + Bu + L(y - \hat{y}) \tag{4.6}$$

$$\hat{y}_i = h_i(C_i\hat{x}) \tag{4.7}$$

The estimation error dynamics, with the estimation error defined as $\tilde{x} = x - \hat{x}$, are given by

$$\dot{\tilde{x}} = A\tilde{x} - LH(x, \hat{x}) \tag{4.8}$$

where the vector $H(x, \hat{x})$ is given by

$$H(x, \hat{x}) = \begin{Bmatrix} \vdots \\ h_i(C_i x) - h_i(C_i\hat{x}) \\ \vdots \end{Bmatrix}.$$

4.3.2 Observer Design Results

Theorem 4.1. If an observer gain L , a diagonal matrix $\Gamma > 0$ and a symmetric positive definite matrix $P > 0$ that satisfy equation (4.9) can be obtained, then the observer (4.6) - (4.7) with this observer gain is globally exponentially stable.

$$\begin{bmatrix} A^T P + PA - \dfrac{C^T M^T \Gamma N C + C^T N^T \Gamma M C}{2} + \sigma P & -PL + \dfrac{C^T (M^T + N^T)\Gamma}{2} \\ -L^T P + \dfrac{\Gamma(M+N)C}{2} & -\Gamma \end{bmatrix} \leq 0 \tag{4.9}$$

Proof: Start with the Lyapunov function candidate:

$$V = \tilde{x}^T P \tilde{x} \tag{4.10}$$

Let $H(x, \hat{x}) = \begin{Bmatrix} \vdots \\ h_i(C_i x) - h_i(C_i\hat{x}) \\ \vdots \end{Bmatrix}$ be a vector function of the feedback error. Then

$$\dot{V} = \tilde{x}^T \{A^T P + PA\}\tilde{x} - H(x, \hat{x})^T L^T P\tilde{x} - \tilde{x}^T PLH(x, \hat{x}) \tag{4.11}$$

or

$$\dot{V} = [\tilde{x}^T \quad H(x, \hat{x})^T] \begin{bmatrix} A^T P + PA & -PL \\ -L^T P & 0 \end{bmatrix} \begin{bmatrix} \tilde{x} \\ H(x, \hat{x}) \end{bmatrix} \tag{4.12}$$

By using the differential mean value theorem, it can be shown that the bounded Jacobian nonlinear function $H(x, \hat{x})$ satisfies the following quadratic inequality:

$$V_1 = \begin{bmatrix} \tilde{x} \\ H(x,\hat{x}) \end{bmatrix}^T \begin{bmatrix} \frac{C^T M^T \Gamma N C + C^T N^T \Gamma M C}{2} & -\frac{C^T (M^T + N^T)\Gamma}{2} \\ -\frac{\Gamma(M+N)C}{2} & \Gamma \end{bmatrix} \begin{bmatrix} \tilde{x} \\ H(x,\hat{x}) \end{bmatrix} \leq 0 \qquad (4.13)$$

Using the S-Procedure Lemma, $\dot{V} < 0$, if and only if $\exists \epsilon > 0$, such that $\dot{V} < \epsilon V_1$. Hence the observer stability condition is

$$\begin{bmatrix} A^T P + PA & -PL \\ -L^T P & 0 \end{bmatrix} - \epsilon \begin{bmatrix} \frac{C^T M^T \Gamma N C + C^T N^T \Gamma M C}{2} & -\frac{C^T (M^T + N^T)\Gamma}{2} \\ -\frac{\Gamma(M+N)C}{2} & \Gamma \end{bmatrix} \leq 0 \qquad (4.14)$$

Absorbing $\frac{1}{\epsilon}$ into the matrix P and requiring a minimum exponential convergence rate of $\frac{\sigma}{2}$, the final observer stability condition is

$$\begin{bmatrix} A^T P + PA - \frac{C^T M^T \Gamma N C + C^T N^T \Gamma M C}{2} + \sigma P & -PL + \frac{C^T (M^T + N^T)\Gamma}{2} \\ -L^T P + \frac{\Gamma(MC + NC)}{2} & -\Gamma \end{bmatrix} \leq 0 \qquad (4.15)$$

4.3.3 Non-Existence of a Constant Observer Gain for Non-Monotonic Output Functions

Here we discuss the lack of a feasible solution to the observer design LMI (4.9) when all the output functions have non-monotonic behavior.

Remark 4.1: If all of the output functions $h_i(C_i x)$, $i = 1,2,\dots,m$ are non-monotonic, and if the A matrix is not already asymptotically stable, then a constant gain observer that satisfies equation (4.9) does not exist. The validity of the above remark can be seen as follows.

If all the output functions are non-monotonic, then, $\frac{\partial h_i}{\partial (C_i x)}$ takes both positive and negative values. Hence $M_i < 0$ and $N_i > 0$. This implies the diagonal matrices $M^T \Gamma N < 0$ and $N^T \Gamma M < 0$.

For equation (4.9) to be satisfied, a necessary condition is

$$A^T P + PA - \frac{C^T M^T \Gamma N C + C^T N^T \Gamma M C}{2} + \sigma P \leq 0 \tag{4.16}$$

Since $C^T M^T \Gamma N C + C^T N^T \Gamma M C \leq 0$, this implies $A^T P + PA + \sigma P < 0$.

This implies that the open-loop matrix A is already exponentially stable, which contradicts the assumptions of the remark. Hence, a constant gain observer that satisfies (4.9) cannot exist if all output functions $h_i(C_i x)$ are non-monotonic.

□

4.3.4 Increased Feasibility due to the Diagonal Matrix Γ

Theorem 4.1 has an additional degree of freedom compared to the conference paper [29] due to the use of the matrix Γ. In this section, through several examples of different lower and upper bounds on the nonlinear functions, it will be shown that the new observer design LMI has enhanced feasibility due to the extra degree-of-freedom provided by the matrix Γ. Consider the dynamic system in (4.1)-(4.2) where $B = 0$, $A = \begin{bmatrix} 0 & 1 & 0 \\ 1 & 0 & 0 \\ 0 & 0 & 0 \end{bmatrix}$ and, $C = \begin{bmatrix} 1 & 0 & 0 \\ 1 & 0 & 0 \\ 1 & 0 & 0 \\ 1 & 0 & 0 \end{bmatrix}$.

For each case in the table below, the bounds M and N in (4.5) are presented. In each example, the feasibility of the LMI from [29] and the feasibility of the current observer design LMI (4.15) was investigated and are shown in the table.

As can be seen from the table, the new observer design method increases the feasibility for solutions. In case I where all output functions are monotonic, both observer designs are feasible. In cases II, III, and IV the method provided in [29] is not feasible, but the LMI (4.15) of the current chapter is feasible. These cases exhibit the increased feasibility of the new observer design method and show the superiority of it compared to our conference paper [29]. The value of the matrix Γ in these cases shows the mechanism by which this observer works; the outputs that are non-monotonic (have negative lower bounds and positive upper bounds for Jacobian) get a smaller weight compared to the outputs that are monotonic, as demonstrated by the values of Γ determined by the LMI solver.

Moreover, the case V further shows that when all of the output functions are non-monotonic neither observer designs have a feasible solution.

Table 4-1. Feasibility analysis for the observer in [29] and the observer presented in this chapter

Case	Bound of the Jacobians of the output functions	[29]	New Observer
I	$N=\begin{bmatrix}1&0&0&0\\0&2&0&0\\0&0&3&0\\0&0&0&4\end{bmatrix}$, $M=\begin{bmatrix}0.1&0&0&0\\0&0.2&0&0\\0&0&0.3&0\\0&0&0&0.4\end{bmatrix}$	✓	✓
II	$N=\begin{bmatrix}1&0&0&0\\0&2&0&0\\0&0&3&0\\0&0&0&4\end{bmatrix}$, $M=\begin{bmatrix}0.1&0&0&0\\0&0.2&0&0\\0&0&0.3&0\\0&0&0&-0.4\end{bmatrix}$	✗	✓ $\Gamma=\begin{bmatrix}1.0&0&0&0\\0&1.2&0&0\\0&0&1.7&0\\0&0&0&0.5\end{bmatrix}$
III	$N=\begin{bmatrix}1&0&0&0\\0&2&0&0\\0&0&3&0\\0&0&0&4\end{bmatrix}$, $M=\begin{bmatrix}0.1&0&0&0\\0&0.2&0&0\\0&0&-0.3&0\\0&0&0&-0.4\end{bmatrix}$	✗	✓ $\Gamma=\begin{bmatrix}1.2&0&0&0\\0&3.4&0&0\\0&0&0.4&0\\0&0&0&0.3\end{bmatrix}$
IV	$N=\begin{bmatrix}1&0&0&0\\0&2&0&0\\0&0&3&0\\0&0&0&4\end{bmatrix}$, $M=\begin{bmatrix}0.1&0&0&0\\0&-0.2&0&0\\0&0&-0.3&0\\0&0&0&-0.4\end{bmatrix}$	✗	✓ $\Gamma=\begin{bmatrix}5.4&0&0&0\\0&0.3&0&0\\0&0&0.1&0\\0&0&0&0.1\end{bmatrix}$
V	$N=\begin{bmatrix}1&0&0&0\\0&2&0&0\\0&0&3&0\\0&0&0&4\end{bmatrix}$, $M=\begin{bmatrix}-0.1&0&0&0\\0&-0.2&0&0\\0&0&-0.3&0\\0&0&0&-0.4\end{bmatrix}$	✗	✗

4.4 Application of Observer Design Result to Linear Position Estimation

4.4.1 Measurement Setup

An electrohydraulic actuator (EHA) is considered in which a bidirectional DC motor is used to power a hydraulic actuator. This linear actuator is self-contained, compact and only needs electrical power.

Figure 4-4 shows an EHA test rig in which two TMR2305M magnetic sensors manufactured by MultiDimension Technology Co. with a sensitivity of $25mV/V/G$ are mounted on a breadboard on top of the hydraulic actuator. A high-accuracy sonar sensor mounted externally measures piston position by shining an ultrasound beam on the piston rod. This expensive ultrasound sensor serves as a reference measurement against which the position estimates of the nonlinear observer can be compared.

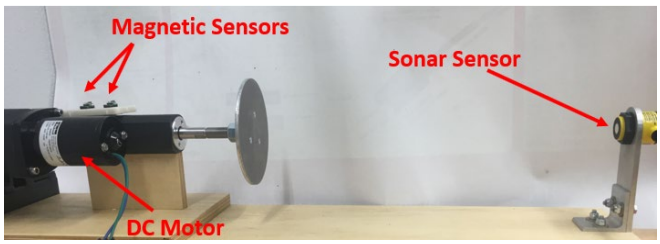

Figure 4-4. Sensor Configuration for position estimation of EHA

The variation of the magnetic field with piston position is shown in Figure 4-5 and Figure 4-6. In both of these figures, the magnetic fields read by the two magnetic sensors fixed on the cylinder are shown as a function of the position of the moving piston. It can be seen that Figure 4-5 has different curves for the two different directions of motion of the piston. This "hysteresis" effect has been removed in Figure 4-6, which shows only one curve as a function of position, irrespective of the direction of motion. The procedure used for removing the "hysteresis" effect is described below.

Since EHAs are made as a compact single device, the DC motor that runs the hydraulic pump is very close to the hydraulic actuator, so the magnetic field generated by the motor affects the measured magnetic field by the sensors.

In other words

$$B_{Hi} = B_i + B_{Mi} \tag{4.17}$$

where B_{Hi} is the measured magnetic field, B_i is the magnetic field of the permanent magnet on the piston and B_{Mi} is the magnetic effect of the DC motor current on each of the magnetometers. It was observed that B_{Mi} affects the measurement data in the form of the hysteresis seen in Figure 4-5. The sign of this magnetic field is determined by the sign of the current supplied to the motor, and the sign of that current also determines the movement direction of actuator.

By modeling the DC motor as a single coil, we can assume that the magnetic field of the motor is linearly dependent on the current supplied to the motor.

$$B_{Mi} = \alpha_i I \tag{4.18}$$

where I is the current and α_i is a constant that is dependent on the lateral position of the magnetic sensors relative to the DC motor, and could be experimentally estimated. By removing the magnetic effect of the DC motor, the hysteresis in the output functions largely disappears, as is shown in Figure 4-6.

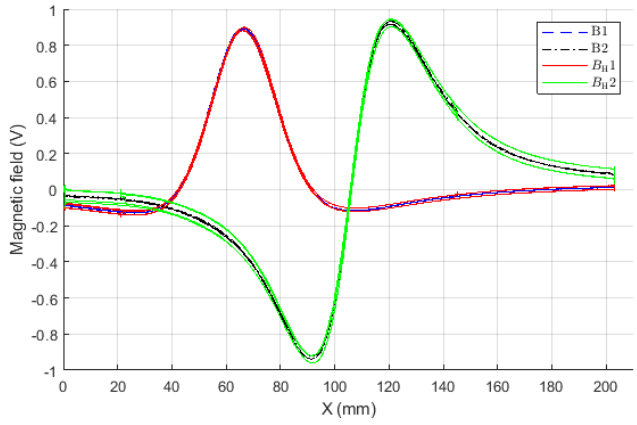

Figure 4-5. Measured magnetic field B_{Hi}, and magnetic field of permanent magnet B_i

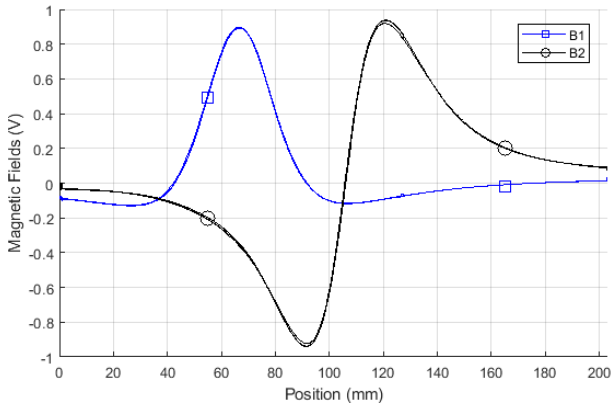

Figure 4-6. Non-monotonic measurement functions of magnetic sensors, after removal of hysteresis

4.4.2 State Estimation procedure

The model for the position estimation dynamic system for the EHA when using two magnetic sensor outputs can be represented as:

$$\dot{x} = Ax + Bu$$
$$\begin{bmatrix} y_1 \\ y_2 \end{bmatrix} = \begin{bmatrix} h_1(C_1 x) \\ h_2(C_2 x) \end{bmatrix} \tag{4.19}$$

where $x = \begin{bmatrix} z \\ v \\ a \end{bmatrix}$, $A = \begin{bmatrix} 0 & 1 & 0 \\ 0 & 0 & 1 \\ 0 & 0 & 0 \end{bmatrix}$ and $C_1 = C_2 = [1\ 0\ 0]$.

Here z, v and a are the position, velocity and acceleration of the piston. Note that the output equations in (4.19) are highly nonlinear functions of the position z, as shown by the curves of Figure 4-6.

These functions are seen to be not only nonlinear but also non-monotonic with both positive and negative slopes for the derivatives. It was shown in Remark 4.1 that in this situation with non-monotonic nonlinear functions, a single observer gain that guarantees exponentially stable estimation over the entire operating range cannot be found. In other words, when the upper and lower bounds of the Jacobian in (4.5) have different signs, the Linear Matrix Inequality (4.9) is not feasible. Hence, a switched-gain observer with a constant observer gain in each piecewise monotonic region is presented next.

4.4.3 High-Gain-Observer

One might consider the possibility of the high-gain-observer for this application. The potential use of the high-gain observer is discussed below using two possible design approaches:

a) The standard high-gain-observer requires the nonlinear function to be only in the process dynamics of the system and the output to be just a linear function of the states. It should be noted that our system in the chapter, on the other hand, has the nonlinear function in the output, instead of the process dynamics. One way to deal with this problem, if the nonlinear output is smooth, is to use a coordinate transformation (a change of variables as mentioned in [4]:

$$z_1 = h(x_1)$$
$$z_2 = \dot{z}_1$$
$$z_3 = \dot{z}_2$$

This coordinate transformation would theoretically transform the system in (4.1)-(4.2) into:

$$\dot{z}_1 = z_2$$
$$\dot{z}_2 = z_3$$
$$\dot{z}_3 = \xi(z)$$

where

$\xi(z) = 3(z_3 g' + z_2 g'')(z_2 g')h'' + \quad (z_2 g')^3 h'''$ with $g(z_1) = h^{-1}(z_1)$.

The problem, however, here is that the output function $h(x_1)$is non-monotonic and therefore not invertible. Thus, $g(z_1)$ is not available. Hence, the standard high-gain observer cannot be utilized for this application.

b) Another way to deal with the nonlinearity in the output, as presented again [4], is to use the nonlinear function directly in the observer and construct the observer as:

$$\dot{\hat{x}}_i = \hat{x}_{i+1} + \frac{\alpha_i}{\beta \epsilon^i}[y - h(\hat{x}_1)], \qquad 1 \le i \le 2$$

$$\dot{\hat{x}} = \frac{\alpha_3}{\beta \epsilon^3}[y - h(\hat{x}_1)]$$

where $\epsilon > 0$ is a small constant and α_i is appropriately selected. However, as a result

of a sector condition, $\beta > 0$ has to be picked to satisfy:

$$\frac{\partial h}{\partial x_1}(x_1) \geq \beta$$

It can be readily seen that this condition implies that the output function needs to be strictly increasing. In this chapter, however, the output functions are non-monotonic. Hence, again, this approach fails and so the high gain observer cannot be utilized for this application.

4.5 Piecewise Observer Design

From the theoretical results in section 4.3 , we have seen that if both output functions are non-monotonic, we cannot find a feasible solution to the observer design LMI (4.9). Attempts in MATLAB to find an LMI solution that works over the entire 203 mm stroke of the EHA cylinder failed, i.e. no feasible solutions to (4.9) existed for the output functions shown in Figure 4-6. The MATLAB evaluations thus reconfirmed the theoretical result of the output functions being required to be monotonic.

With the monotonicity requirement in mind, the position range of 0 – 203 mm can be divided piecewise into different regions in a manner that in each region at least one of the output functions is a monotonic function of position.

The separation of the operating range into piecewise regions is done in a manner so as to make each region have only monotonic output functions. The break-points for the piecewise regions are therefore located at the zero-slope points of the outputs, since a zero-slope point is the transition from an increasing to a decreasing function or vice-versa. By having the break-point at the zero-slope point, the outputs are maintained to be monotonic in each piecewise region.

Such a piecewise division of the position range into regions R_1 to R_{11} is shown in Figure 4-7. Note that the boundaries of the regions lie at the slope change points (of one or the other output function). For example, R_4 is a narrow region in which the slope of the output y_1 is close to zero. In this region, only the output y_2 will be used by the observer, since y_2 is monotonic in this region. Regions R_3 and R_5 lie on either side of R_4 and both

of these regions can utilize both outputs y_1 and y_2, since both y_1 and y_2 are monotonic in these regions.

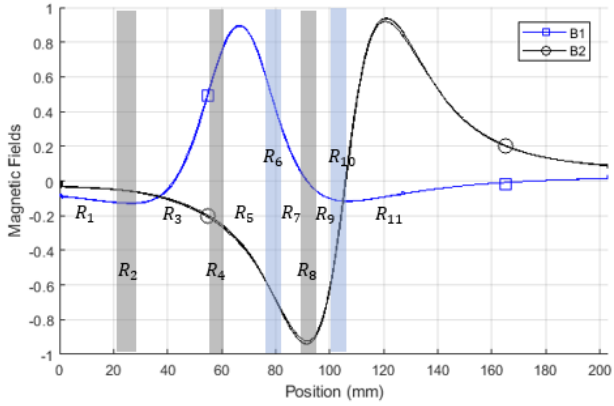

Figure 4-7. Creating regions around slope-change points of output functions

It should be noted that we have the liberty of relying on only one of the output measurements in the narrow regions with zero slope, because even with one output the system is still observable, although the result of estimation might not be as accurate as the case when we use both outputs. Hence, the width of these regions was kept narrow so as to minimize regions with use of only 1 output by the observer. It is ideal to have these regions to be as narrow as possible, but in practice their width is determined by the accuracy of the measurement models. For example, if we anticipate a considerable horizontal uncertainty or shift in the output function models, we are forced to sacrifice the estimation accuracy for the sake of stability by widening the width of the zero slope (single output) regions.

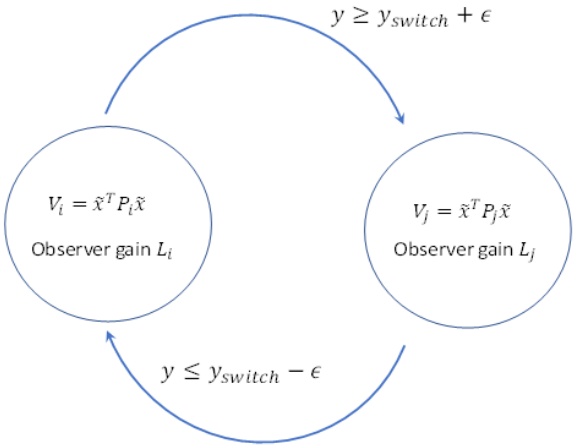

Figure 4-8. Creating regions around slop-change points of output functions

A switched gain observer is developed using the regions defined in Figure 4-7. As shown in Figure 4-8, the switched gain observer uses different gains in each of the discrete piecewise regions. Since each region R_1 through R_{11} has monotonic output function properties, a constant stabilizing observer gain exists in each of these regions. As the operating region changes, the observer gains switch in value accordingly using a finite state machine of the type shown in Figure 4-8 [29].

The stability of the hybrid observer of Figure 4-8 consisting of different constant observer gain regions needs to be considered. It should be noted that inside each region, a single observer gain is used and therefore exponential stability is guaranteed inside this region using the Lyapunov function analysis of Remark 4.1. However, different regions i may have different values of the matrix $P_i > 0$ in their individual Lyapunov functions. The stability of the overall switched system can be guaranteed if the system satisfies a minimum dwell time constraint in each region [28]. The minimum dwell time in region j when switching from region i to region j needs to be greater than T where T is the amount of time needed for $V_j\big(x(t+T)\big) < V_i\big(x(t)\big)$. This minimum dwell time guarantees global asymptotic stability.

This result can be understood as follows: In each individual region, the estimation error $\tilde{x}$ keeps decreasing due to the Lyapunov exponentially stable design in that region. In switching between regions, the P matrix may be different in the two regions. However, if the system remains in the same region for a minimum dwell time, the error will become smaller than the initial value at the time the region was entered (due to local exponential stability).

Thus, if the system is constrained to remain in one region for a minimum dwell time, the value of the Lyapunov function after the dwell time in region j is less than its value in region i at the time the switch from i to j occurred. This guarantees overall asymptotic stability [28].

To sum it up, it was proven in Theorem 4.1 that the observer is asymptotically stable when the observer operates within one monotonic region. In this section we showed that by constraining the observer to remain in a monotonic region for a minimum dwell time, the observer remains asymptotically stable even when the switch in gain and region

happens. Putting these two results together maintains global asymptotic stability.
One obstacle that could affect the performance of this piecewise nonlinear observer is the initial condition. If we pick the initial condition to be in the wrong region (with the wrong observer gain), it might result in a divergence of the observer estimates. However, thanks to the specific shape of output functions for the EHA application, there is an easy solution that can remedy this shortcoming. In Figure 4-7, we can see a one-to-one relationship between the position and the ordered pair that is constructed by the two output functions y_1 and y_2, hence we can identify the correct region for the initial condition accurately.

4.6 Experimental Results

The estimated position using the nonlinear observer is compared to the actual position of the piston measured with an expensive sonar sensor in Figure 4-9. As can be seen in the results in Figure 4-9, the estimates closely follow the actual measured reference values of the position.

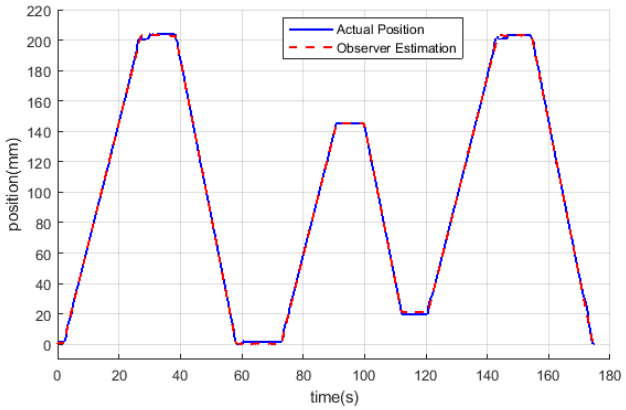

Figure 4-9. Estimated position along with the actual position using a reference sensor.

The estimation error of the nonlinear switched observer is presented in Figure 4-10 by computing the difference between the reference and estimated values of piston position. The estimation error has a root mean square (rms) value of 0.9 mm and a maximum value of 4 mm. The maximum errors occur at the two ends of the stroke. At the ends of the stroke, both the output functions have their lowest sensitivity. The slope of each of the output curves at the ends of the stroke are low and around 0.02 V/cm (0.16 Gs/cm). This

makes the position estimation task difficult, since the magnetic field changes very little with position at the ends of the stroke.

Along with the error signals of the nonlinear observer, the errors in estimate of an Extended Kalman Filter estimator is also shown in Figure 4-10. The error of the nonlinear observer (max error < 2%) is considerably smaller than that of the EKF (max error of 6%). The nonlinear observer performs better because by dividing the domain into piecewise sections, the observer has more freedom for tuning of the gains compared to the EKF. We can change the convergence rate of the observer and the weight of each of the measurement functions in each region, based on the accuracy and sensitivity of them in that region but standard EKF is stuck with the same Q and R matrix through the whole domain.

4.6.1 Stability of EKF and Piecewise Observer in the Presence of Model Mismatch

The superiority of the switched nonlinear observer compared to the EKF can be further illustrated by introducing a small amount of model mismatch in the regions involving a change in slope of the outputs. One instance of such a model mismatch is presented in Figure 4-11. The curves for the two outputs $y_1 = B_1$ and $y_2 = B_2$ were slightly scaled by 2% to introduce a difference between the assumed model and the actual measured signals.

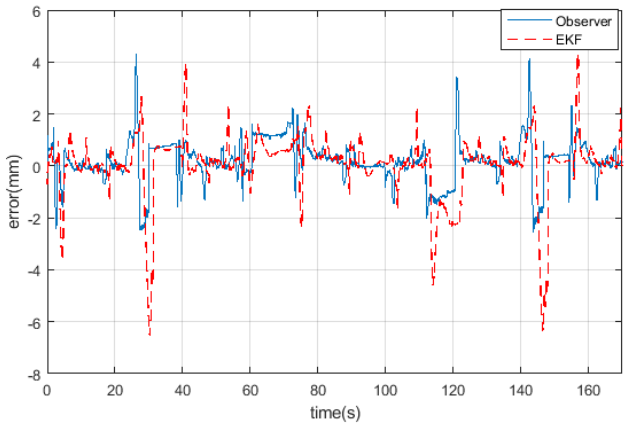

Figure 4-10. Comparison between the estimation errors of the piecewise nonlinear observer and of the EKF

The results of EKF estimation using the wrong model is presented in Figure 4-12 and the position estimation using the switched nonlinear observer is shown in Figure 4-13. It is

obvious that EKF struggles in the presence of this mismatch and has significant error due to wrong (destabilizing) filter gains which also lead to subsequent wrong estimates of position leading further to incorrect filter gains. On the other hand, the switched nonlinear observer exhibits good performance, as seen in Figure 4-13. This is because the nonlinear observer does not use the specific output which has zero slope in the entire region where the zero slope occurs.

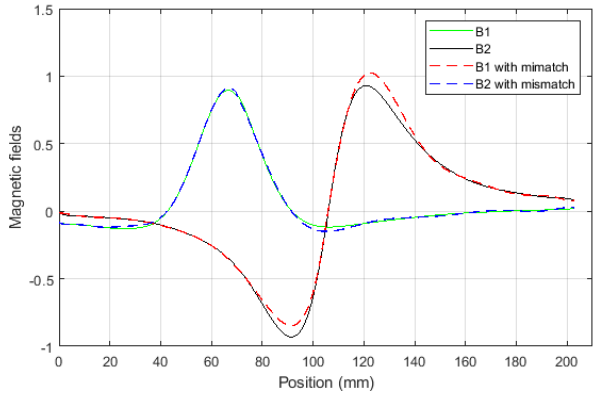

Figure 4-11. Mismatch in the output models near the slope-change points

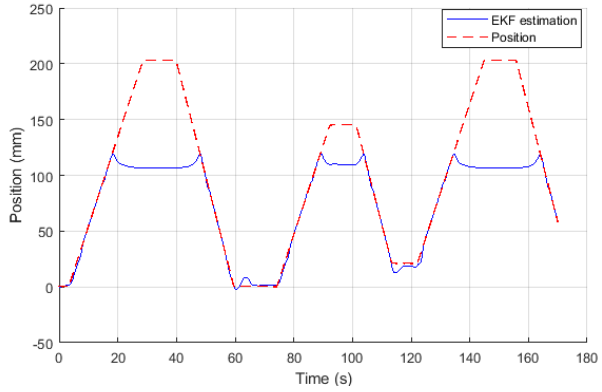

Figure 4-12. EKF estimation in the presence of model mismatch

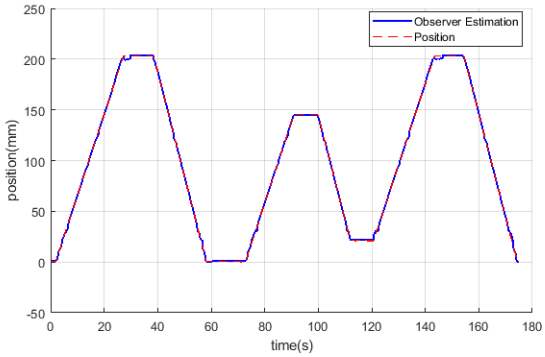

Figure 4-13. Piecewise observer in the presence of model mismatch

4.7 Sensor Location Optimization

In this part of the chapter, we seek to find the best placement of magnetic sensors out of a set of possible sensor locations to find the best estimate of the piston position and reduce estimation error. We will be using two axes (along and perpendicular to cylinder axis) of each magnetic sensor and will be choosing the placements out of 17 possible locations for the sensors.

Figure 4-14. Schematic of 17 choices for sensor placement

In our system where the output of the system is $y_i = h_i(z)\ for\ i = 1 \dots p$ the output matrix at each point in the operating range can be obtained as follows from linearization:

$$C(z) = \begin{bmatrix} h_1'(z) & 0 & 0 \\ \vdots & \vdots & \vdots \\ h_p'(z) & 0 & 0 \end{bmatrix} \tag{4.20}$$

Assuming the A matrix is the one given in (19), the observability matrix can be calculated as:

$$\mathcal{O}(z) = \begin{bmatrix} h_1' & 0 & 0 \\ \vdots & \vdots & \vdots \\ h_p' & 0 & 0 \\ 0 & h_1' & 0 \\ \vdots & \vdots & \vdots \\ 0 & h_p' & 0 \\ 0 & 0 & h_1' \\ \vdots & \vdots & \vdots \\ 0 & 0 & h_p' \end{bmatrix} \tag{4.21}$$

Hence the square of (all three) singular values of the observability matrix for p sensors can be obtained from:

$$\sigma^2 = \sum_{1}^{p} h_i'^2 \tag{4.22}$$

where p is the number of sensors. As can be seen from (4.22), the square of singular value of observability matrix, in our problem, has additive characteristic over outputs.

4.7.1 Optimization Problem

Here, we use the minimum singular value of the observability matrix as the metric for the sensitivity of each output to position and seek to find the minimum number of sensors which could deliver a certain desired accuracy. Hence the optimization problem can be stated as:

$$\begin{aligned} &\min_{w} \|w\|_0 \\ &s.t. \sum_{m=1}^{17} w_m \, {h_m'}^2(z) - \lambda_{min} I_N \succcurlyeq 0\,,\ 0 \le x \le l \\ &w \in \{0,1\}^{17} \end{aligned} \tag{4.23}$$

where $\|.\|_0$ is the zero norm of the vector w with weights given to each sensor; $w_i = 1$ means we pick the ith sensor and $w_i = 0$ means the sensor is removed. Hence, the objective function will be the number of sensors; a quantity we are interested to minimize. Note that the 0-norm corresponds to the total number of non-zero elements in the vector.

The constraint guarantees a higher bound on the worst-case estimation error, by making sure that the minimum singular value of the observability matrix is larger than a predetermined amount λ_{min}.

The zero-norm function is non-convex and requires integer solvers which are computationally very expensive. Therefore, we need to relax the objective function and use the one-norm as a compromise. The relaxed form of the problem then can be specified as:

$$\min_{w} \|w\|_1$$

$$s.t. \sum_{m=1}^{17} w_m {h'_m}^2(z) - \lambda_{min} I_N \succcurlyeq 0\,, \tag{4.24}$$

$$0 \leq z \leq l$$

$$0 \leq w_m \leq 1$$

The resulting optimized solution for this problem will be a vector with $0 \leq w_i \leq 1$. We will be using a randomized rounding algorithm to turn the elements of this solution into $w_i \in \{0,1\}$.

Were the output functions *h(z)* linear, we would have been able to solve the problem at this stage. Because the singular value of the observability matrix could have been easily attained. However, as it was seen in this case, the magnetic field outputs are highly nonlinear and non-convex. So, the singular value for each sensor will be a function of position z. To address this issue, the z domain needs to be gridded and the observability matrix be calculated for each node and the minimum singular value constraint must be satisfied on those nodes. So if for sensor *m* on node *n*, by local linearization we have $y_m^n = \mathcal{H}_m^n z$ the square of singular value on that node could be presented as:

$$\Sigma^n = \sum_{1}^{17} w_m \mathcal{H}_m^n {\mathcal{H}_m^n}^T \tag{4.25}$$

Now if we define Σ as:

$$\Sigma = \begin{bmatrix} \Sigma^1 & 0 & 0 \\ 0 & \ddots & 0 \\ 0 & 0 & \Sigma^n \end{bmatrix} \tag{4.26}$$

then we can present the final form of the problem as:

$$\min_{w} \|w\|_1$$
$$s.t.\ \Sigma - \lambda_{min} I_N \succcurlyeq 0 \tag{4.27}$$
$$0 \leq w_m \leq 1$$

4.7.2 Optimization Results

The minimum square singular value $\lambda_{min} = 1e-4$ was chosen at first, by using the YALMIP LMI Toolbox and the sdpt3 solver, the following optimal vector was found.

$$w^{*T} = [0.000, 0.008\ , 0.006, 0.006, 0.007, 0.006, 0.006, 0.006, 0.008, 0.010, 0.007,$$
$$0.012, 0.012, 0.067, 0.008, 0.008, 0.000]$$

One way to proceed is to normalize this weight vector and then round the elements to acquire a weight vector consisting of zero and ones. But there is an issue with this approach; there is no guarantee that the rounded weights actually will satisfy the minimum singular value requirement.

Another method could be picking the largest weights, until the singular value requirement is satisfied. The problem with this approach is that it neglects the raison d'etre of this optimization problem, which was minimizing the number of used sensors for a predefined accuracy.

To illustrate more clearly, consider a simple example where we have three possible sensor positions where the first and second sensor positions each are extremely sensitive in different halves of the domain and the third one is less, however acceptably, sensitive for the whole domain. It's obvious that solving the relaxed optimization problem will result in weights $w_1, w_2 \gg w_3$, because the required sensitivity can be achieved with small weights of first and second sensor and there won't be any need for relatively larger weight of third sensor. Picking the largest weights will result in choosing the first and second sensors, while the correct solution to this problem is choosing the third sensor which can single handedly satisfy our condition.

Therefore, we will follow the proposed ***Randomized Rounding algorithm*** [63] with some adjustments:

1. *Assuming* $w^* = [w_1^* \quad \dots \quad w_m^*]^T$

2. Define a random vector

$$\varpi_m = [0,\ 1,\ 0,\ 0\ , 1, \dots, \varpi_{m,l}] \in \mathbb{R}^L,\ \ with\ probabiliy\quad p(\varpi_m) = w_m^*$$

3. *Create the set that satisfies the constraint* $\Omega = \{l|\lambda_{min}\{F(\varpi_{l,x})\} \geq \lambda_{eig}$
4. *Find the* $\widehat{w} = \underset{l\in\Omega}{min}\|w_l\|_0$
5. *Create the set* $\Psi = \{\varpi_s|s \in\ \Omega, \|\varpi_s\|_0 = \widehat{w}\ \}$
6. *Find* $W^*\ s.t.\lambda_{min}(W^*) = max\,\lambda_{min}(\varpi_s), where\ \varpi_s \in \Psi$

Applying this algorithm makes sure that the solution satisfies the minimum accuracy constraint, has the minimum possible sensors, and among those minimum possible sensor placements it has the best performance.A truncated Poisson distribution was used to create the random vectors; the resulting weight vector from this algorithm in this case turned out to be:

$$W^{*^T} = [0, 0,0, 1, 0, 0, 0, 0, 0, 0, 0, 0, 0,0,0,0, 1,0]$$

This means two sensors at locations of 80-180.5 mm are picked. The output result of the sensors is presented in Figure 4-15. To use the hybrid observer, we need to divide the domain into 20 piecewise monotonic regions. Each zero-slope point on the figure is where the observer gain needs to switch in value, since the operating region moves from one monotonic region to another.

If we change the minimum square singular value to $\lambda_{min} = 3e - 4$ the optimal vector will change to

$$W^{*^T} = [0.000, 0.024, 0.018, 0.019, .020, 0.017, 0.018, 0.017,$$
$$0.024, 0.030, 0.020, 0.035,0.035,0.201,0.025, 0.024,0.000]$$

And after applying the randomized rounding algorithm the resulting weight vector will be

$$W^{*^T} = [0, 0,1, 0, 0, 0, 0, 0, 1, 0, 0, 0,1,0,0, 0,0]$$

This means three sensors at the positions of 55-117.5-195.5 mm are picked. The output result of the sensors is presented in Figure 4-16. The output functions need to be divided into 27 monotonic regions to be used in hybrid observer. As was described earlier, the number of monotonic regions is dictated by the number of zero-slope points in the magnetic sensor output functions. As can be seen in the figure, the magnetic outputs have a total of 13 zero-slope points within the total position range. This generates 26 regions in each of

which the outputs are monotonic (no zero-slope points). There is also an overlap between two of the bands around 85 mm which creates the 27th region.

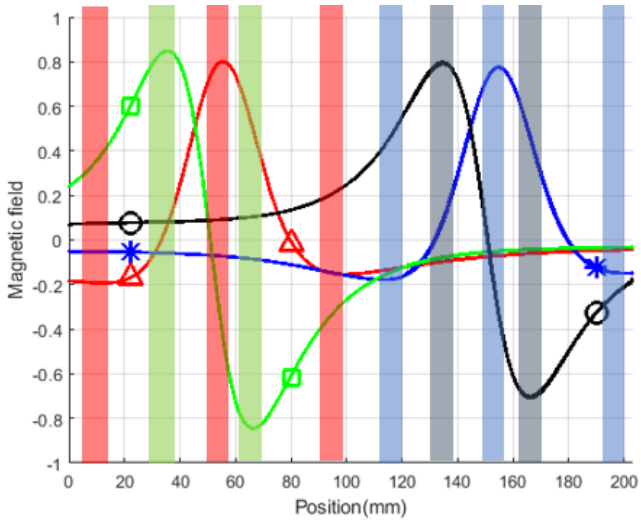

Figure 4-15. The output functions for optimum sensor positioning for two sensors. □ and ○ signify the B_x components and △ and ∗ represent the B_y components of magnetic field of each of the two sensors

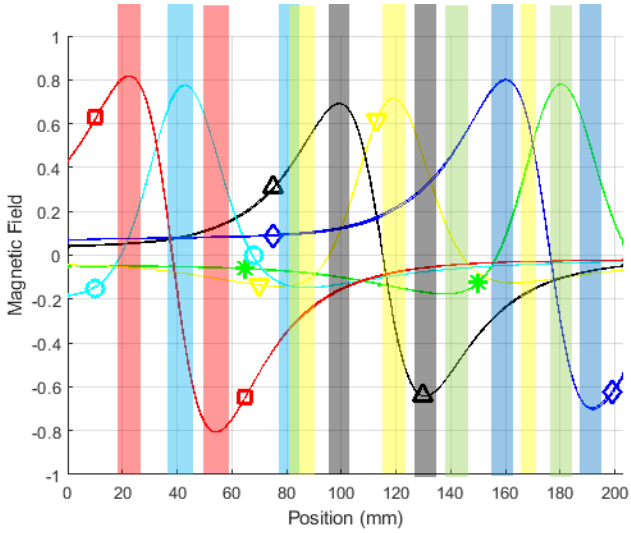

Figure 4-16 . Dividing the domain into 27 regions of monotonic outputs for three sensors. □, △, and ◊ signify the B_x components and ○, ▽, and ∗ represent the B_y components of magnetic field of each of the three sensors

4.7.3 Experimental Results

Next, we will be implementing the attained sensor placements and find the error estimation and compare to some other placements. The resulting observer estimation for two sensors is presented in Figure 4-17.

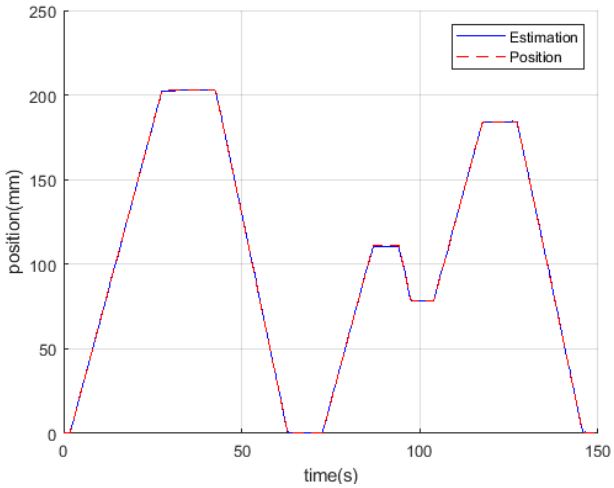

Figure 4-17. Position estimation using the optimum positioning of two sensors

The estimation error for this case is illustrated in Figure 4-18. It can be seen that the peak error is of the order of 1.2 mm, which translates into a percentage error of 0.6% over the 203 mm stroke of the actuator. Thus, with two optimally placed sensors, the position estimation system is already able to meet the performance specification of better than 1% accuracy.

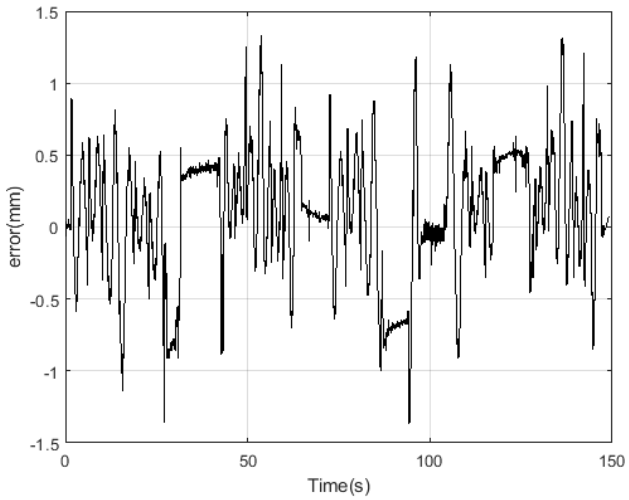

Figure 4-18. Position estimation error using the optimum positioning of two sensors

The resulting observer estimation for three sensors is presented in Figure 4-19.

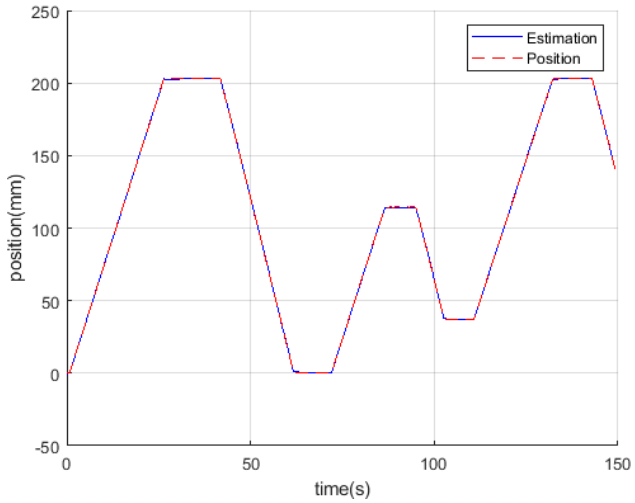

Figure 4-19. Position estimation using the optimum positioning of three sensors

For the three sensors case, to check the optimality of sensor positioning, we take two other possible sensor positionings into account and compare the resulting estimation error with the optimum case. For one of these suboptimal cases the sensors were placed further away from each other and were put at 5-105-220.5. For the other case the sensors were brought closer to center with 80-130-170.5 placement. The resulting error for each case is compared with the optimal error in Figure 4-20.

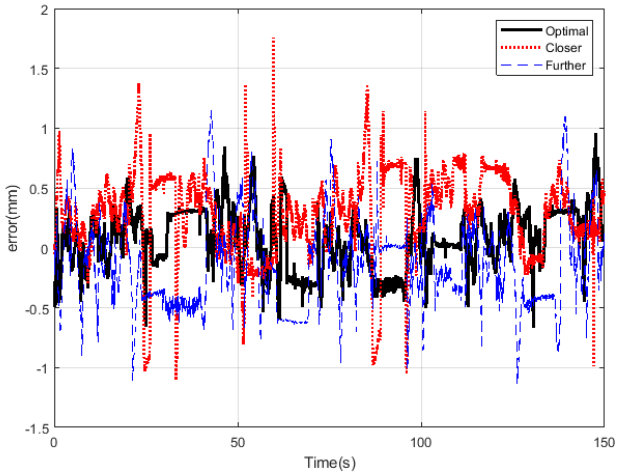

Figure 4-20. Error comparison for optimal and suboptimal sensor positioning for three sensors

The resulted error in each case is presented in Table 4-2.

Table 4-2. Estimation error for optimal and suboptimal cases

Sensor position	rms error (mm)	Max error (mm)
optimal	0.27	0.96
Further away from each other	0.40	1.15
Closer to center	0.47	1.76

As can be deduced from the table of errors, the optimal sensor placement resulted in lower rms and maximum error compared to two suboptimal cases.

4.8 Conclusions

This chapter focused on observer design for a dynamic system with linear process dynamics and non-monotonic nonlinear measurement equations. A Lyapunov-analysis-based observer design method for exponentially stable state estimation and a corresponding LMI for computing the observer design gains were developed. A result showing that a stable observer gain cannot exist if the output functions are all non-monotonic was presented

The developed observer design method was applied to linear position estimation using magnetic sensors for piston position in smart industrial actuators. The output equations for magnetic field as a function of position are nonlinear and non-monotonic in such applications. A single constant observer gain that can satisfy the observer stability condition over the entire range of operating conditions does not exist, but a constant stabilizing gain does exist in each piecewise monotonic region. A methodology for discretizing the operating range into piecewise regions and using a finite state machine for switching between piecewise regions was developed.

Experimental results were presented on the performance of the observer in accurately estimating linear position. An rms error of 0.5% and a maximum error of 2% were demonstrated. The experimental results show that the switched nonlinear observer performs considerably better than an EKF due to its superior use of appropriate outputs

and gains in different regions.

Furthermore, an optimization problem was formulized and solved to find the best sensor locations for the magnetic sensors. Experimental data was presented to show the optimality of the location solutions which resulted in a further reduction of the rms error to 0.1% and of the maximum error to 0.5%.

Chapter 5

Hysteresis Compensation and Nonlinear Observer Design for State-of-Charge Estimation Using a Nonlinear Double-Capacitor Li-Ion Battery Model

5.1 Introduction

Lithium-ion cells dominate the battery market for automotive propulsion and for consumer electronics due to their advantages of high energy density and slow self-discharge [30]. Estimating the state-of-charge (SoC) of a battery in real time is important in order to gauge the remaining time of operation available for the vehicle or the electronic gadget. Hence, SoC estimation has received a lot of attention in the literature [31]. A majority of the studies are concerned with model-based estimation, which exploits the descriptive ability of a battery model to make better sense of the measurement data for more accurate estimation. Two types of models have gained much popularity in this regard: electrochemical models that can characterize the electrochemical reactions and associated physical phenomena inside a battery during charging/discharging, and equivalent circuit models that simulate a battery's electric behavior using electric circuits [44]. While the former can paint a detailed picture of a battery's dynamics, the latter is arguably more

advantageous in terms of computational efficiency and real-time estimation. Based on both types of models, Kalman filters for estimation have found wide use in SoC estimation, e.g., [64], [65], [66], [67], [68], [69], [70]. More recently, nonlinear filtering approaches such the unscented Kalman filter (UKF) and the ensemble Kalman filter have shown good performance for battery state estimation [34], [71]. Meanwhile, nonlinear observers represent another critical means of performing state estimation, having drawn much interest in the past decade due to their generally lower computational complexity and amenability to global convergence analysis [4], [21]. The literature has reported SoC observer designs based on nonlinear adaptive or discrete-time observer [35], [72], [43], [73], [74], [75], sliding-mode observer [76], inter-connected observer [77], PDE observers [78], [79], and moving horizon estimation [50].

Among the battery models in the literature, a newly proposed equivalent circuit model, named nonlinear double-capacitor (NDC) model, distinguishes itself as an appealing choice [80]. Though parsimonious in structure, the NDC model can well capture a battery's nonlinear voltage dynamics and has excellent predictive capability and thus is adopted in this chapter as the battery model. However, SoC estimation based on the NDC model is challenging due to the nonlinearity rooted to this model. Motivated by this issue, this chapter utilizes a Lipschitz nonlinear observer design method that provides a single observer gain with globally stable performance for this model. Compared to linearization and varying gain observers, such as the extended Kalman Filter (EKF), the developed observer has two advantages: lower computational effort and superior convergence performance.

An additional contribution of this chapter is the development of a modified Preisach model to compensate for the hysteresis in the terminal voltage versus SoC relationship as the modeling in [80] does not consider this effect. By using a modified Preisach model to represent the hysteresis, a weighted sum of hysterons with the weights obtained from experimental data-based training is utilized. This yields a high-fidelity match with the experimentally observed hysteresis behavior.

The outline of the rest of this chapter is as follows. Section 5.2 presents the NDC model for a lithium-ion battery. The modified Preisach model for hysteresis representation is

introduced. The observer design problem is formulated in Section 5.3. This is followed by development of a Lyapunov analysis-based observer design method. In Section 5.4, the application of the observer design method to the SoC estimation problem is presented. Experimental data is utilized to verify the performance of the observer. A comparison of performance with the EKF and the UKF is presented. Section 5.5 presents the conclusions of the chapter.

5.2 Battery System and Hysteresis Model

5.2.1 Battery Model

The NDC model, as shown in Figure 5-1, consists of a nonlinear voltage source U, a resistor R_0, an RC circuit $R_1 - C_1$, and a hysteresis voltage component V_h. Here, different from existing equivalent circuit models, the voltage source U is designed as a nonlinear mapping from a double-capacitor circuit (see the left-hand side of Figure 5-1). This circuit, comprising two parallel capacitors ($C_b \gg C_s$) and resistors ($R_b \gg R_s$), can simulate a battery's electrode, and the charge transfer between $C_b$and C_s, comparable to the lithium-ion diffusion between the bulk inner part and surface of an electrode. Further, the voltage source U nonlinearly depends on the voltage across C_s, say V_s. This configuration makes the NDC model better capture the influence of the charge state on the terminal voltage, which makes the model physically more reasonable and more accurate in predicting a battery's voltage behavior [80], [81]. The NDC model is provably a streamlined approximation of the single particle model, further justifying its soundness.

The dynamic equations of the NDC model can be represented as:

$$\dot{x} = Ax + BI \tag{5.1}$$

where the state vector is $x = [V_b\ ,\ V_s\ , V_1]^T$ and consists of the voltages across the capacitors C_b, C_s and C_1, respectively, with the constraint $0 \leq V_b, V_s \leq 1$. The variable I is the input current, with $I > 0$ representing charging of the battery and $I < 0$ signifying discharging of the battery.

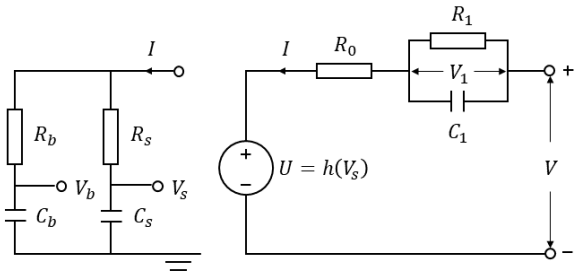

Figure 5-1. NDC equivalent circuit model

The matrices A and B are given by

$$A = \begin{bmatrix} -\frac{1}{C_b(R_b+R_s)} & \frac{1}{C_b(R_b+R_s)} & 0 \\ \frac{1}{C_s(R_b+R_s)} & -\frac{1}{C_s(R_b+R_s)} & 0 \\ 0 & 0 & -\frac{1}{R_1C_1} \end{bmatrix}, B = \begin{bmatrix} \frac{R_s}{C_b(R_b+R_s)} \\ \frac{R_b}{C_s(R_b+R_s)} \\ -\frac{1}{C_1} \end{bmatrix} \tag{5.2}$$

The sole output function of the system is the terminal voltage which is modeled as:

$$V = f(V_s) + IR_0 - V_1 + V_h \tag{5.3}$$

where the nonlinear function $f(V_s)$ represents the open-circuit voltage source U and V_h represents a hysteresis term. Here, $f(V_s)$ can be expressed as a monotonically increasing polynomial function of V_s. Note that the function $f(\cdot)$ also characterizes the SoC-OCV relation, because $V_s = \mathrm{SoC}$ in the open-circuit equilibrium state.

In this model, SoC can be calculated from the following relationship:

$$SoC = \frac{C_bV_b + C_sV_s}{C_b + C_s} \tag{5.4}$$

Note also that, differing from the original model in [80], [81], we add a new term V_h in (5.3) to account for the voltage hysteresis in charging and discharging, further improving the model accuracy. Further details are offered below.

5.2.2 Hysteresis in Batteries

Li-ion batteries normally suffer from a considerable amount of hysteresis [31], [82]. Figure 5-2 shows an example of the hysteresis in the open circuit voltage (OCV) as a

function of SoC, as the battery undergoes charging and discharging. It should be noted that the hysteresis function cannot just be represented using two different curves for charging and discharging, since the curves will differ each time when there is a switch from charging to discharging or vice-versa at various values of SoC.

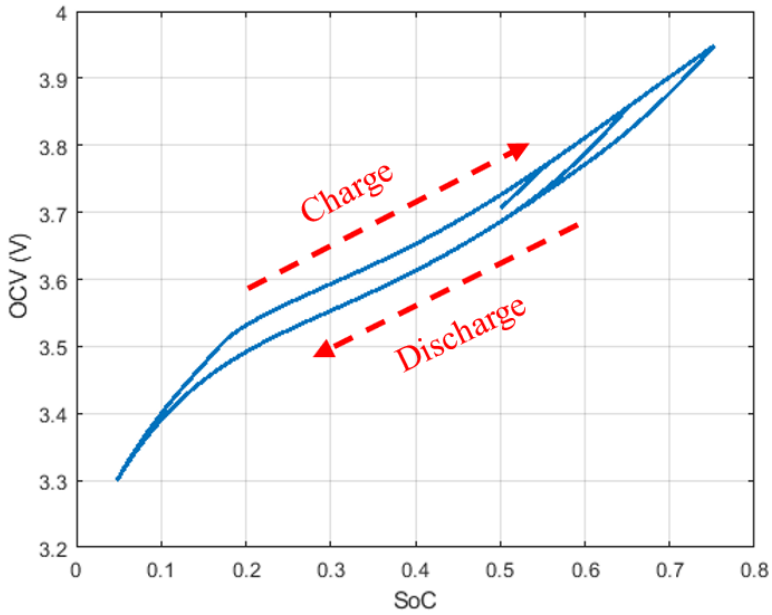

Figure 5-2. Hysteresis in open circuit voltage

5.2.3 Hysteresis Models

Numerous methods have been previously utilized in literature to model the phenomenon of hysteresis. In this sub-section the most popular modeling methods will be described and the need for a new model suitable for observer design will be justified.

One modeling method that has previously been used in battery systems [44] is a dynamic differential equation form of model:

$$\frac{dV_h(t)}{dt} = \gamma \left|\frac{I(t)}{Q_t}\right| \left(M\, sgn\big(I(t)\big) - V_h(t)\right) \tag{5.5}$$

where γ and M are constants and Q_t is the total capacity of the battery. The problem with using this model is that the system loses observability when $I(t) = 0$. This fact can be seen in Figure 5-3 below. In this figure, the minimum singular value of the observability matrix [58] is calculated for different values of current and different values of $df(V_s)/dV_s$, and

as it can be seen, the observability matrix loses rank when the current is equal to zero. Hence, this model does not work for the SoC state estimation problem. Note that when there is loss of observability for zero current, it will not be possible to know the SoC of the system if a battery has idled for some time. Any slow leakages that have occurred and have changed the SoC will not be compensated for and the SoC will be unknown. The observability result in Figure 5-3 holds for the nonlinear model described in (5.3) including the hysteresis term of (5.5).

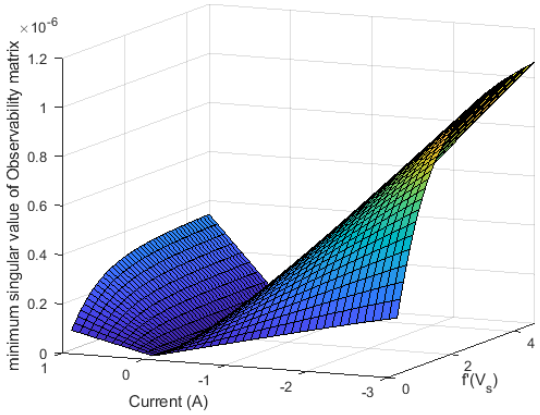

Figure 5-3. Minimum singular value of the observability matrix based on current and $f'(V_s) = df(V_s)/dV_s$

The Preisach model is another method that has previously been used for hysteresis representation, especially in magnetic and piezoelectric applications [56]. The Preisach model is physically intuitive and consists of a summation of hysterons, each of which gets switched on or off as the SoC changes. Unfortunately, the traditional Preisach model is discontinuous at the switching points [83]. Hence, a nonlinear observer that depends on a plant model with the Preisach hysteresis representation cannot be designed to ensure stability using Lyapunov analysis.

The discontinuity problem in the Preisach model has been previously addressed using Krasnoselskii-Pokrovskii (KP) kernels [84]. The problem with the KP kernels method is that the kernel is a function of the derivative of the argument, and this makes it not desirable for observer design.

In light of the above, this chapter develops and utilizes a modified Preisach model for hysteresis representation. This modified Preisach model, as described later, is Lipschitz

continuous and therefore suitable for use in nonlinear observer design. A conference version of this chapter presents preliminary results on the modified Preisach model [85].

5.2.4 Modified Preisach Model for Hysteresis Compensation

In the proposed modified Preisach model, the hysteresis voltage is presented as an explicit function of estimated states. Compared to other models, the proposed modified Preisach does not have any unobservability issues.

In the modified Preisach model, a superposition of several weighted relay operators is employed to replicate the hysteresis behavior of a function.

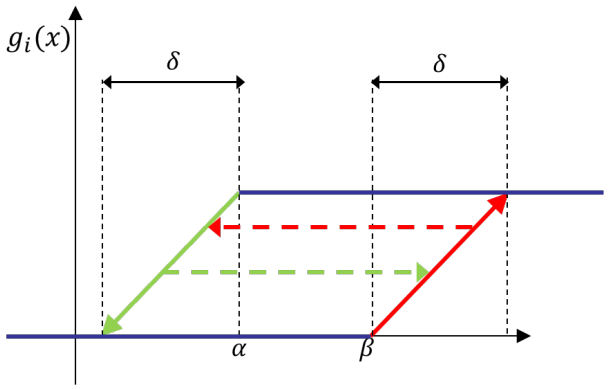

Figure 5-4. One single relay in modified Preisach hysteresis model

Figure 5-4 shows one of these relays (hysterons). Each relay has an ON region and a different OFF region. Thus, the relay switches ON and switches OFF at different values, yielding a hystersis behavior. If x is larger than the ON point β, the relay will be turned on. Similarly, if x is lower than the OFF point α, the relay will be turned off. For the interval between the OFF and the ON region, the relay output is modeled as a function of its output from the last time step. Within ON and OFF regions the output is modeled in such a way that there are no discontinuities in it and therefore the function as a whole remains Lipschitz. Hence, the output function of each Preisach relay can be mathematically defined as:

$$g_i(x) = \begin{cases} 1 & if\ x \geq \beta + \delta \\ max\left(k, \frac{x-\beta}{\delta}\right) & if \beta + \delta \geq x > \beta \\ k & if\ \beta \geq x > \alpha \\ min\left(k, \frac{x-(\alpha-\delta)}{\delta}\right) & if\ \alpha \geq x > \alpha - \delta \\ 0 & if\ \alpha - \delta \geq x \end{cases} \tag{5.6}$$

where k is the output of the relay from the last time step. Each relay then will be assigned a weight w_i and the relays summed together to create the desired hysteresis output.

$$g(x) = \sum_{i=1}^{N} w_i g_i(x) \tag{5.7}$$

where N is the number of relays that evenly divide the domain.

In this application, the hysteresis in voltage is assumed to be a function of SoC. It is to be noted that the relays have overlaps, implying that, for each amount of SoC, multiple relays get activated. Moreover, a polynomial function is used as a nominal base $p(SoC)$for the model (Figure 5-5):

$$V_h = p(SoC) + \sum_{i=1}^{201} w_i g_i(SoC) \tag{5.8}$$

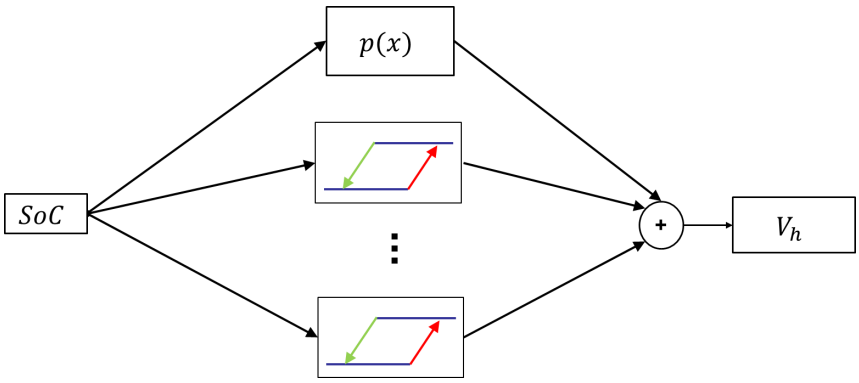

Figure 5-5. Preisach hysteresis model

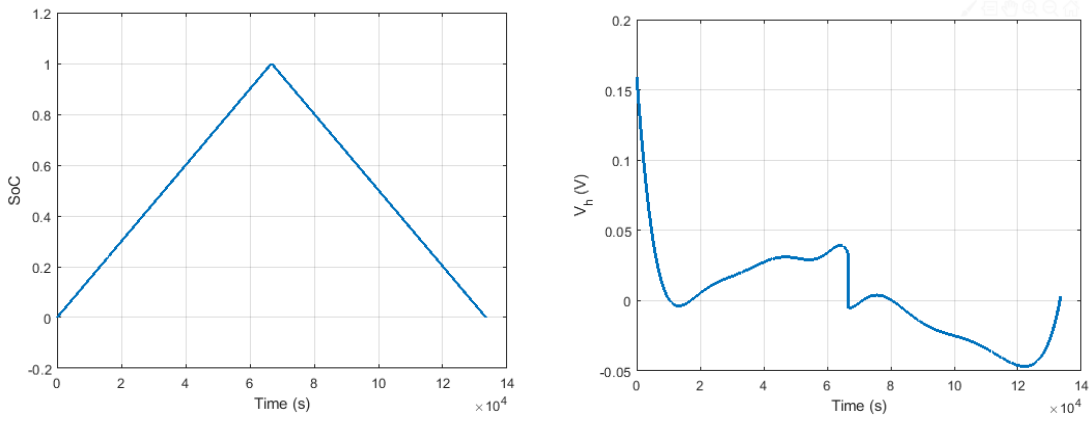

(a) (b)

Figure 5-6. Hysteresis voltage for training the modified Preisach model

By increasing the number of hysterons for representing the nonlinear hysteresis term, we can more accurately recreate the hysteresis profile and decrease the estimation error. However, that increases the computational burden. Hence the procedure adopted was to increase the number of hysterons until we had an acceptable amount of low error in the hysteresis model. Thus, the number of hysterons was increased to 201 until the root mean square (rms) error between the hysteresis model and the observed hysteresis data was reduced to 5 mV.

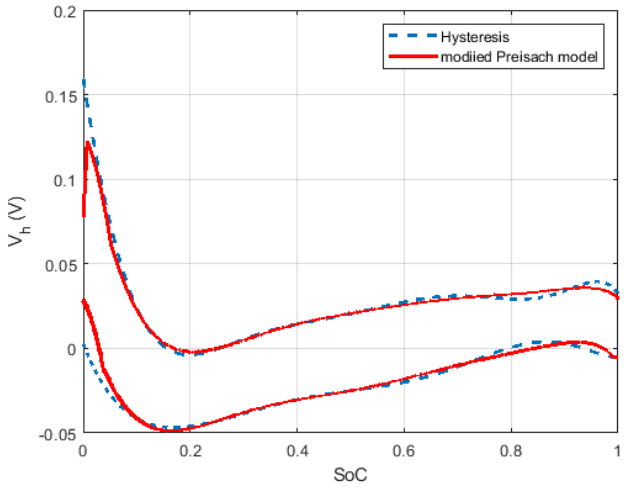

Figure 5-7. The final modified Preisach model after training

The values of the hysteron parameters α, β and δ are determined by uniformly distributing the hysterons over the operating range of the SoC. To ensure that the modified

Preisach model is both accurate and smooth in the entire operating range of SoC all the way to the upper limit of 1, the extended range of 0 - 1.5 of SoC was divided into 201 hysteron relays which makes the values of alpha and beta for a hysteron equal to 0.0075 and 0.0150. It is to be noted that since there is no physical data for values of SoC > 1, some artificial data was used to extend the model to the range 1< SoC < 1.5, even though this range is never used in the actual real-time estimation. To ensure symmetry in the hysterons, the parameter δ is chosen as the difference between β and α and is equal to 0.0075.

A constrained least square method is used to find the weights w_i and the coefficients of $p(SoC)$. The YALMIP toolbox is used so as to minimize the 2-norm of the error between the hysteresis model and the modified Preisach model while keeping the possible weights within the range of [-0.05,0.05]. Here a training data set with SoC profile of Figure 5-6(a) was used, and the resulting hysteresis voltage is presented in Figure 5-6(b). This training data set was obtained from a slow-discharge experiment (Figure 5-9) and a slow-charge experiment (Figure 5-12). The hysteresis voltage is taken to be the difference between OCV and the charge voltage in Figure 5-12 and the discharge voltage in Figure 5-9, where the OCV is extracted from the data in Figure 5-15 [80].

The output of this model can be seen in Figure 5-7, demonstrating an accurate match between the model and the experimental hysteresis values.

5.3 Observer Design Results

Consider the system

$$\begin{aligned} \dot{x} &= Ax + Bu \\ y &= C\,x + h_1(e_1 x) + h_2(e_2 x) \end{aligned} \tag{5.9}$$

with $x \in R^n$, $u \in R^p$, $C, e_i \in R^{1\,x\,n}$, $h_i : R \to R$, and the rest of the matrices having appropriate dimensions. Here $h_1(e_1 x)$ represents the nonlinear function $f(V_s)$ discussed in the battery model, and $h_2(e_2 x)$ represents the hysteresis which is a nonlinear function of SoC. Both these nonlinear functions are functions of scalar variables $e_1 x$ and $e_2 x$

respectively. Assume $h_i(e_i x)$ is continuous and Lipschitz which is true for both the battery NDC model and the modified Preisach model. Note that (5.8) is an algebraic function of SOC and hence the output representation in (5.9) is correct for the hysteresis function of (5.8).

Consider the observer:

$$\dot{\hat{x}} = A\hat{x} + Bu + L(y - \hat{y}) \tag{5.10}$$
$$\hat{y} = C\hat{x} + h_1(e_1\hat{x}) + h_2(e_2\hat{x})$$

Defining the estimation error as $\tilde{x} = x - \hat{x}$, the dynamics of the estimation error can be derived as:

$$\dot{\tilde{x}} = (A - LC)\tilde{x} - L\{\tilde{h}_1(e_1 x, e_1\hat{x}) + \tilde{h}_2(e_2 x, e_2\hat{x})\} \tag{5.11}$$

where $\tilde{h}_i(e_i x, e_i\hat{x}) = h_i(e_i x) - h_i(e_i\hat{x})$. We can write $\tilde{h}_i(e_i x, e_i\hat{x})$ as:

$$\tilde{h}_1 = (\psi_1)(e_1\tilde{x}) \tag{5.12}$$
$$\tilde{h}_2 = (\psi_2)(e_2\tilde{x})$$

by using the definitions

$$\psi_i = \begin{cases} \dfrac{h_i(e_i x) - h_i(e_i\hat{x})}{e_i\tilde{x}} & for\ e_i\tilde{x} \neq 0 \\ 0 \qquad for\ e_i\tilde{x} = 0 \end{cases} \tag{5.13}$$

Since $h_i(e_i x)$ is a Lipschitz function of $e_i x$, it is easy to show that the following constant bounds exist on each ψ_i:

$$\underline{\gamma}_i \leq \psi_i \leq \overline{\gamma}_i \tag{5.14}$$

where $\underline{\gamma}_i$ and $\overline{\gamma}_i$ are constants related to the one-sided Lipschitz constants of $h_i(e_i x)$. Hence $\psi_1(e_1 x)$ and $\psi_2(e_2 x)$ are bounded by constants and belong to a convex set with vertices [9]:

$$\mathcal{V} = \left\{v \in R^{1\,x\,2} : v = [\underline{\gamma}_i, \overline{\gamma}_j], i, j = 1,2\right\} \tag{5.15}$$

The *innovative use of the functions* ψ_1 and ψ_2 defined in (5.13) enables the design of a

globally stable observer by using the vertices of these functions which belong to a convex set.

Theorem 5.1. The observer (5.10) is asymptotically stable if there exists a positive definite matrix $\mathcal{P}$ and an observer gain L such that the following LMI-transformable inequality is satisfied for ψ_i at each vertex of the convex set $\mathcal{V}$:

$$(A-LC)^T\mathcal{P}+\mathcal{P}(A-LC)-\mathcal{P}Le_1\psi_1-\psi_1e_1^TL^T\mathcal{P}-\mathcal{P}Le_2\psi_2 \\ -\psi_2e_2^TL^T\mathcal{P}<0, \qquad \forall v\in\mathcal{V} \tag{5.16}$$

where $v\in\left\{\underline{\gamma}_i,\overline{\gamma}_j\right\}$ with $\underline{\gamma}_i$ and $\overline{\gamma}_i$ being the lower and upper Lipschitz bounds of ψ_i.

Proof: Consider the Lyapunov function candidate:

$$V=\tilde{x}^T\mathcal{P}\tilde{x} \tag{5.17}$$

Then its derivative can be calculated as:

$$\dot{V}=\tilde{x}^T\mathcal{P}\dot{\tilde{x}}+\dot{\tilde{x}}^T\mathcal{P}\tilde{x}$$

$$=\tilde{x}^T[(A-LC)^T\mathcal{P}\ +\mathcal{P}(A-LC)]\tilde{x}-\tilde{x}^T\mathcal{P}L\tilde{h}_1-\ \tilde{h}_1^TL^T\mathcal{P}\tilde{x}-$$

$$\tilde{x}^T\mathcal{P}L\tilde{h}_2-\tilde{h}_2^TL^T\mathcal{P}\tilde{x}$$

$$=\tilde{x}^T[(A-LC)^T\mathcal{P}+\mathcal{P}(A-LC)]\tilde{x}-\tilde{x}^T\mathcal{P}Le_1\tilde{x}\psi_1-$$

$$\psi_1\tilde{x}^Te_1^TL^T\mathcal{P}\tilde{x}-\tilde{x}^T\mathcal{P}Le_2\tilde{x}\psi_2-\psi_2\tilde{x}^Te_2^TL^T\mathcal{P}\tilde{x}$$

$$\dot{V}=\tilde{x}^T[(A-LC)^T\mathcal{P}+\mathcal{P}(A-LC)-\mathcal{P}Le_1\psi_1-\psi_1e_1^TL^T\mathcal{P} \\ -\mathcal{P}Le_2\psi_2-\psi_2e_2^TL^T\mathcal{P}]\tilde{x} \tag{5.18}$$

$\dot{V}<0$ holds if

$$(A-LC)^T\mathcal{P}+\mathcal{P}(A-LC)-\mathcal{P}Le_1\psi_1-\psi_1e_1^TL^T\mathcal{P}-\mathcal{P}Le_2\psi_2-\psi_2e_2^TL^T\mathcal{P}<0 \tag{5.19}$$

which will be satisfied in the convex set bounding ψ_1 and ψ_2 if it is satisfied on all vertices in $\mathcal{V}$. [23] ■

Note that observability is a necessary condition for a solution to exist for the observer design LMI (5.16).

5.4 Application of the Developed Nonlinear Observer to the Battery Model

The A matrix for the plant model (5.9) has been presented in (5.2). Here $C = [0, 0, -1]$, and since the current is known and gets multiplied by a constant coefficient R_0 in the output equation, it does not have any influence on the observer gain. Hence, this observer will be stable for any amount of current. Moreover:

$$h_1(e_1 x) = f(V_s)\,, h_2(e_2 x) = V_h(SoC) \tag{5.20}$$

where V_h represents the modified Preisach model. The bounds on ψ_1 are $\underline{\gamma_1} = 0.3, \overline{\gamma}_1 = 4.7$ and bounds on ψ_2 are $\underline{\gamma_2} = 0.05, \overline{\gamma}_2 = 2.1$ .The vertices, therefore, are calculated as:$v_1 = [0.3\,, 0.05], v_2 = [4.7\,, 0.05],\ v_3 = [0.3\,, 2.1], v_4 = [4.7\,, 2.1]$.

For the specific battery model under consideration, the nonlinear function $f(V_s)$ is given by

$$f(V_s) = \ 3.20 + 4.69V_s - 20.49V_s^2 + 43.71V_s^3 - 41.50V_s^4 + 14.54V_s^5 \tag{5.21}$$

which is a monotonic function. Solving the LMIs numerically using YALMIP [86], a feasible solution and globally stabilizing observer gain is obtained as:

$$L = [0.0085\,,\ 0.0098,\ -0.0028]^T.$$

5.4.1 Experimental Results

All the experimental data in this chapter was gathered by conducting tests on a Samsung INR18650-25R lithium-ion battery cell (cathode: LiNiMnCoO2, anode: carbon) using a PEC SBT4050 battery tester at the University of Kansas (see Figure 5-8). The battery nominal capacity was 2.5 Ah and it was set to operate between 3.2 V and 4.2 V. Three data sets were used to examine the performance of observer.

For the tests, a pre-determined profile of input current was applied to the battery and the output terminal voltage was measured. For the first data set, it can be seen in Figure 5-9(a) that the experiment includes discharging the battery from full capacity to lower cut-off voltage of 3.2 V using a constant current of 0.125 A. The corresponding output terminal voltage is seen in Figure 5-9(b).

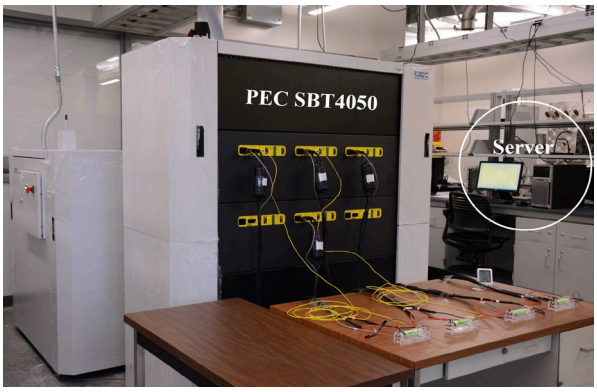

Figure 5-8. Experimental setup

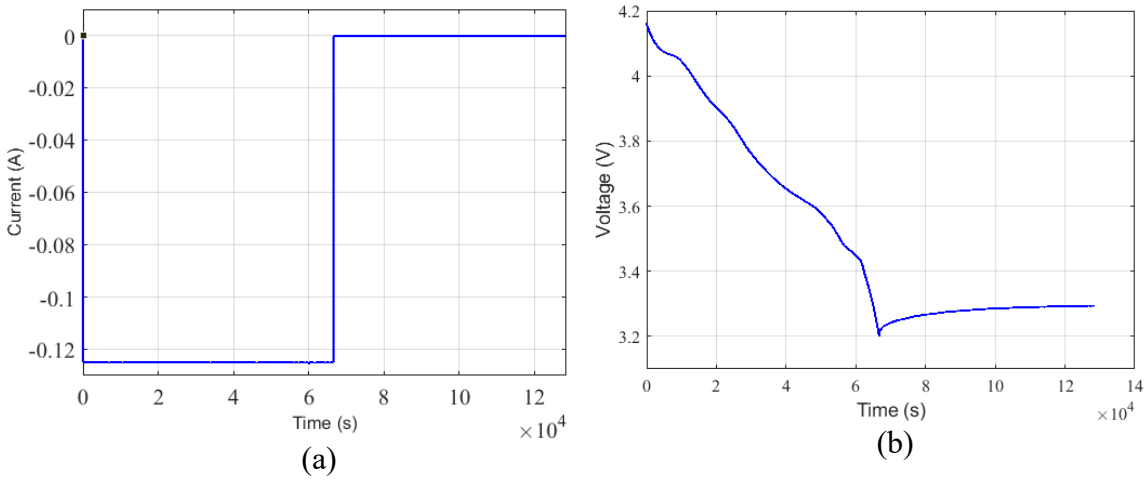

Figure 5-9. Current profile and output of battery for the first test set

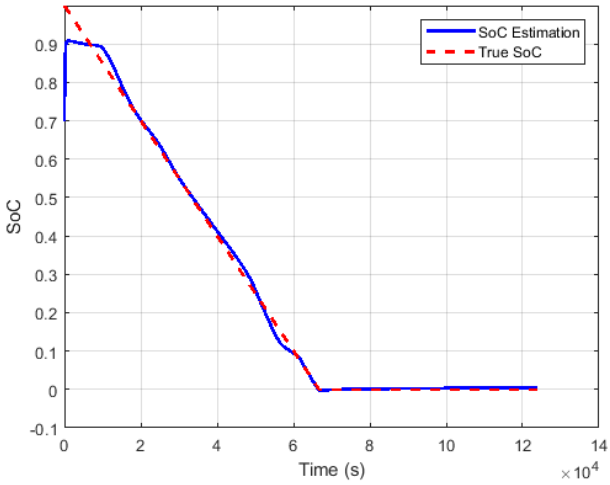

Figure 5-10. Observer estimation result for the first set

The experimental results in [80] have validated that the NDC model can deal with up to 1.2 C or even slightly higher charging/discharging rates. The max current used in the experiments in this chapter is about 1.2 C, so the NDC model is accurate for the experimental results reported.

A 30% error for initial condition was assumed to examine the convergence time of the observer. The results of the observer showing the estimated SoC, along with real SoC, are presented in Figure 5-10. As can be seen in the figure, the estimation follows the true SoC values closely. It is to be mentioned that even though the measured voltage drifts at the end of the data set, the estimation does not show a large amount of error at the end, and that is because the output function $f(V_s)$ is very steep near zero SoC. Therefore, the drift at zero SoC at the end translates to a small error in SOC estimation.

The estimation error, defined as the difference between the estimated and actual SoC values, is presented in Figure 5-11. The rms value of the error, calculated after the initial convergence from initial condition offsets, is computed to be equal to 0.0124 (or 1.24%).

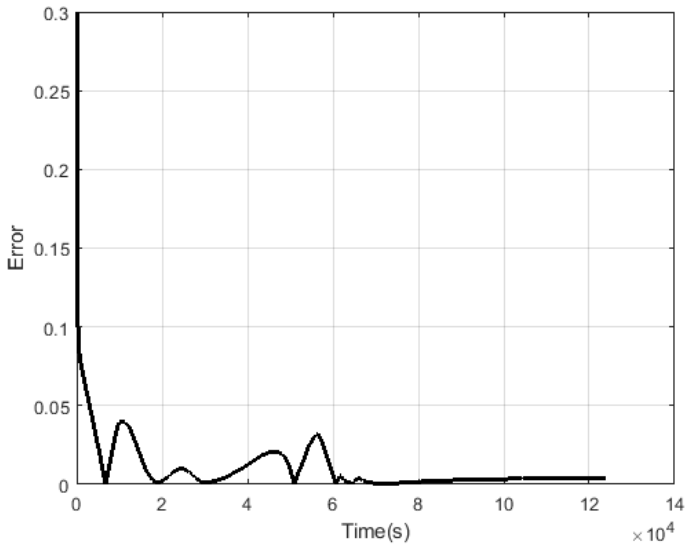

Figure 5-11. Observer Estimation Error

For the second data set, the battery is charged to the upper cut-off voltage of 4.2 V under a constant current of 0.125 A, as shown in Figure 5-12.

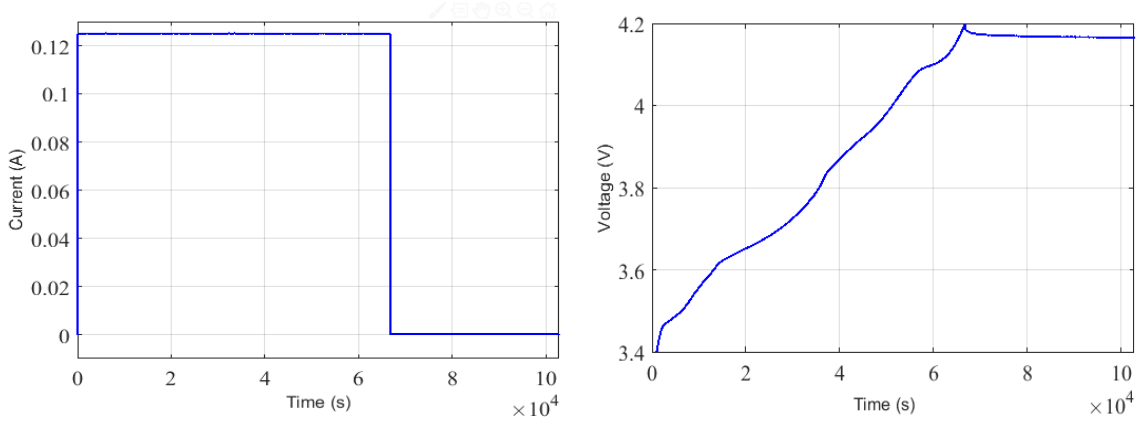

(a) (b)

Figure 5-12. Current profile and output voltage of the second set

The estimation result is presented in Figure 5-13. As seen, the observer corrects most of the initial condition error in the first step of estimation. There are two spots (small regions) that the estimation deviates from the true value and those spots correspond to the regions of maximum mismatch between the model and measured voltage.

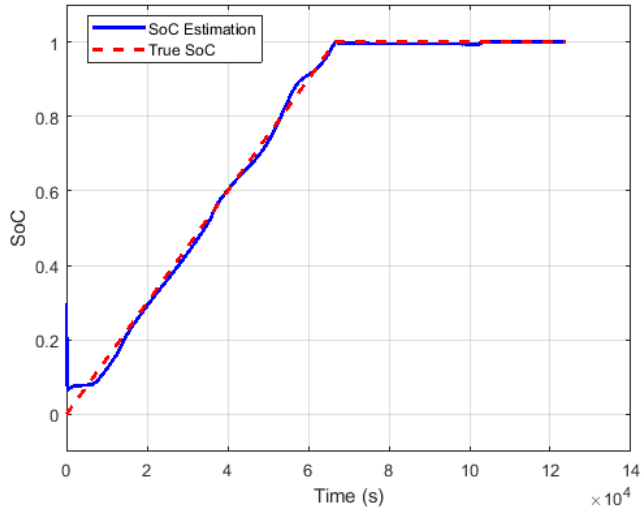

Figure 5-13. Observer estimation result for the second set

The estimation error for the second experiment is shown in Figure 5-14. The rms error for this experiment after convergence is equal to 0.0115(1.15%).

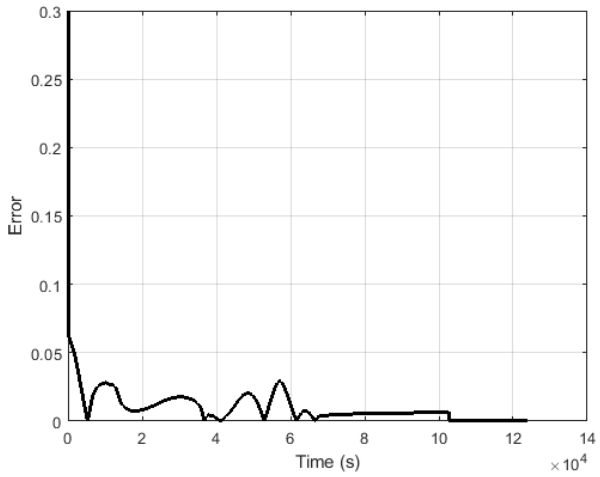

Figure 5-14. Estimation error for the second data set

For the third data set, the battery starts from a fully charged state and a profile of different currents is applied to the battery to discharge and charge the battery as shown in Figure 5-15(a). The third data set has never been used in training of the hysteresis model, and thus constitutes a completely new test for the estimation system. The observer estimation results along with true SoC are shown in Figure 5-16.

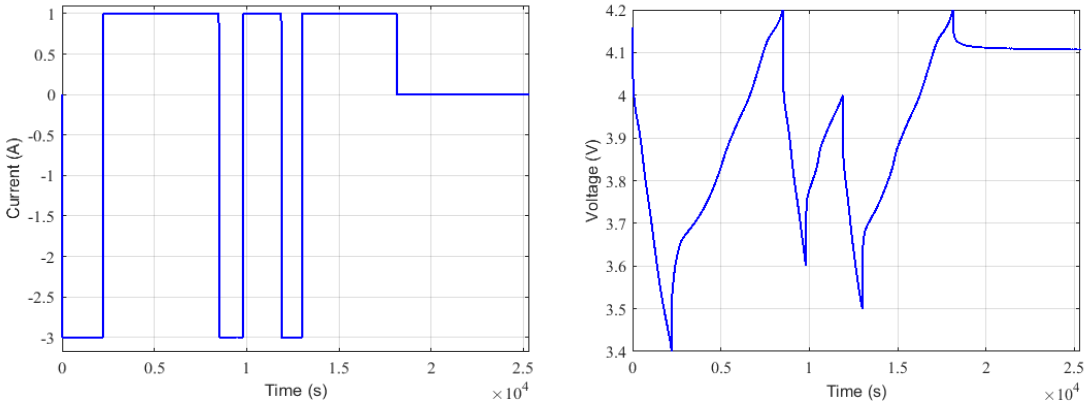

(a) (b)

Figure 5-15. Current profile and output voltage of the third set

The estimation error for the third experiment is shown in Figure 5-17. The rms error for this experiment after convergence is equal to 0.0138(1.38%).

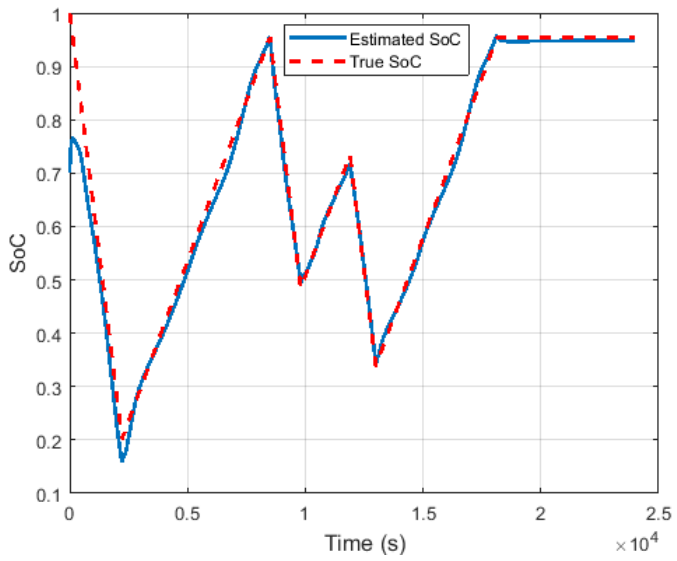

Figure 5-16. Observer estimation result for the third set

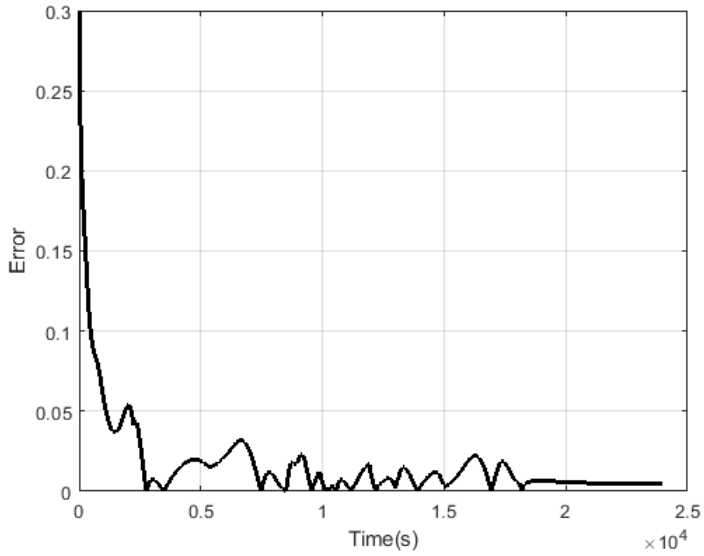

Figure 5-17. Estimation error for the third data set

5.4.2 Extended Kalman Filter and Unscented Kalman Filter

The extended Kalman filter (EKF) is an estimation method that is especially popular for nonlinear dynamic systems and could be utilized for this type of estimation problem. First, the Q and R matrices (process and sensor covariance values) were extensively tuned to get the best performance possible with the EKF. The covariance element for each state in the process dynamics was gradually and separately changed to find the best performance

for EKF; the same procedure was done to find the best measurement covariance in the sensor equations. The initial state covariance matrix P_0 was picked based on the maximum possible initial condition error, i.e. the diagonal elements of $((\hat{x}_0 - x_0)(\hat{x}_0 - x_0)^T)$. The results of EKF estimation using the well-tuned input variance value of $Q = \text{diag}([1\ , 1\ , 0.01\ ])$, a sensor variance value of $R = 10^{-2}$ and $P_0 = \text{diag}([0.3\ , 0.3\ , 0.1])$ are shown in Figure 5-18.

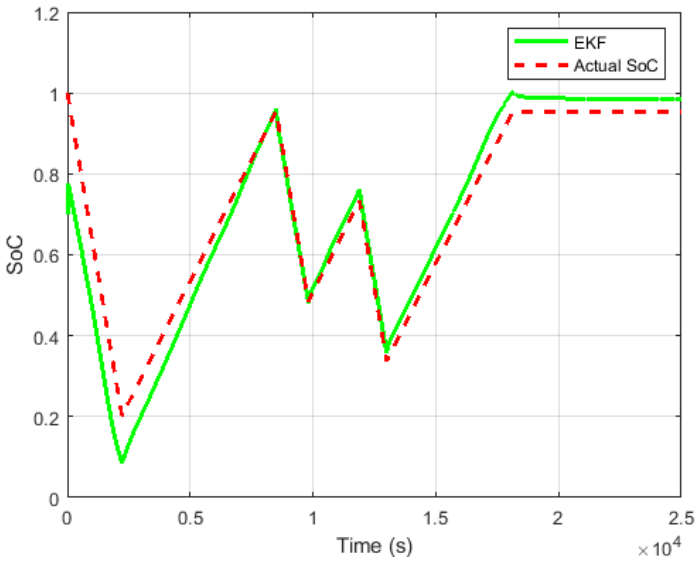

Figure 5-18. EKF estimation

The EKF estimation error and the nonlinear observer estimation error are compared with each other in Figure 5-19. As can be seen in the figure, the EKF, compared to the nonlinear observer, is more prone to slowly converge from the offset in initial condition and does not recover quickly from it. Increasing the dependency on output functions, by reducing R matrix, does not influence the convergence time much either. Therefore, we can conclude that the nonlinear observer is a more suitable estimation method compared to the EKF for the problem in hand.

The poor convergence performance of the EKF from the initial condition error can be understood from the difference in sensitivity values $\frac{\partial h}{\partial y}$ at different values of SoC. Due to the incorrect initial value of the sensitivity, an observer with poor selection of local observer gain can result and lead to slow convergence. The nonlinear observer, on the other

hand, has a constant observer gain, with a guaranteed global convergence rate.

Furthermore, EKF suffers from steady state error. This could be due to the fact that hysteresis could not be modeled adequately for the EKF using the modified Preisach model, since this model is just Lipschitz and not continuously differentiable.

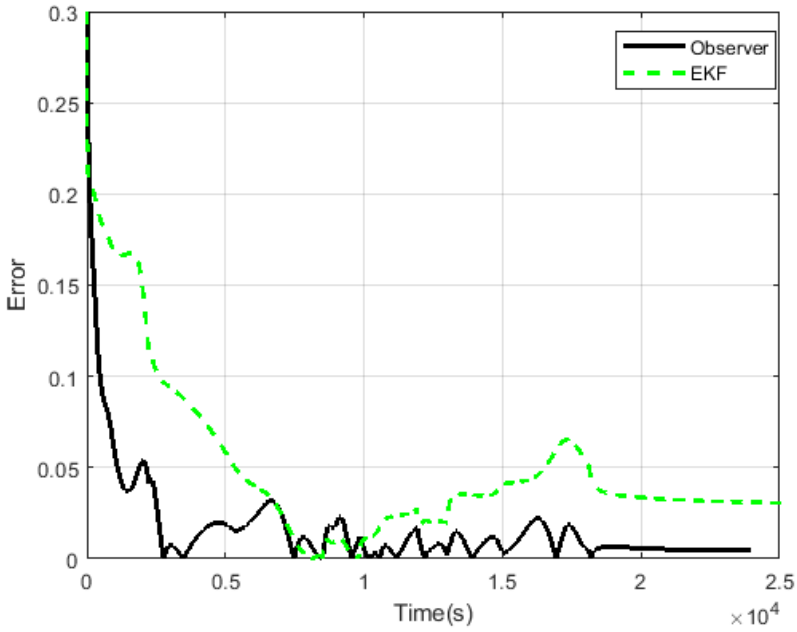

Figure 5-19. EKF and observer estimation error

Another more recent and powerful estimation method for dealing with highly nonlinear systems is the UKF. In this method [87], instead of linearizing the nonlinearities at each operating point, a set of sigma points with the desired mean and covariance are picked and then transformed with nonlinear mappings of the dynamic system. Then the mean and covariance of the transformed sigma points are estimated to provide state estimates.

This method provides up to a third order estimation for the nonlinear function [87], as opposed to a linear approximation by the EKF, and hence suffers from less estimation error compared to the EKF. Another advantage of UKF is that it does not need the calculation of Jacobian of the nonlinearities and hence, in our case, can be combined well with the proposed modified Preisach model.

State estimation with the UKF was implemented using $Q = \mathrm{diag}([10^{-4}, 10^{-4}, 10^{-6}])$, $R = 10^{-2}$. It is customary to use the range of maximum possible initial conditions to calculate the initial covariance. However, the range of the

third state is not easily accessible and that can cause some initial error in estimation larger than the nonlinear observer, as shown in Figure 5-20.

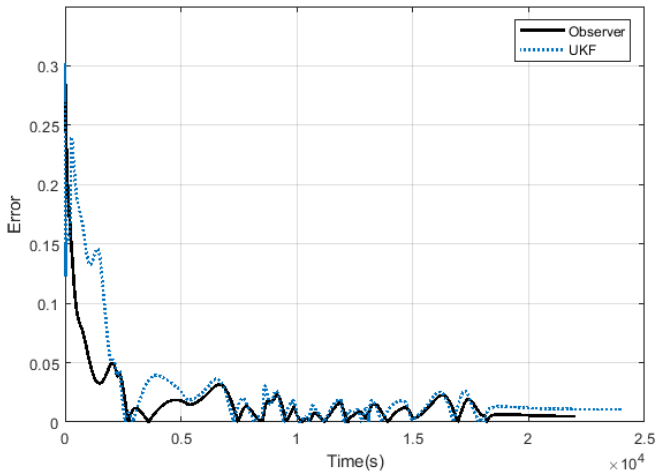

Figure 5-20. Estimation error of UKF with P_0 not properly tuned.

If we further fine tune for initial covariance and use $P_0 = \text{diag}([0.3\,, 0.3\,, 0.1])$, the estimation error will improve as shown in Figure 5-21.

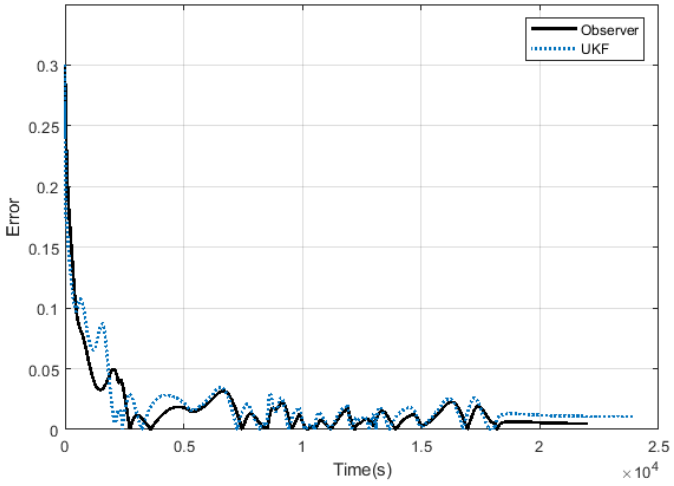

Figure 5-21. UKF and observer estimation error

As can be seen in Figure 5-21, the UKF estimation error is much better than EKF and on par with that of the designed nonlinear observer. However, it performs slightly poorer than the nonlinear observer for initial convergence. It should be noted that an additional advantage of the nonlinear observer is that it has guaranteed global stability and

convergence rate, while the stochastic methods lack such assurances. Further, it is computationally efficient since no online computation of gain is required.

5.5 Conclusions

This chapter developed an observer for SoC estimation using an improved NDC model with the inclusion of hysteresis for representing the dynamics of a lithium-ion battery. The hysteresis in the battery was modeled using a modified Preisach model which had advantages of being Lipschitz continuous compared to the traditional Preisach model. A nonlinear observer for Lipschitz continuous nonlinear measurement equations was developed using Lyapunov analysis to guarantee global asymptotic stability. The design of the observer gain was based on solving an LMI-convertible inequality over the vertices of the involved convex functions.

The parameters of the modified Preisach model were determined from experimental data using a constrained least square method. The performance of the developed nonlinear observer was evaluated using three sets of experimental data. The observer performed well with the maximum SOC estimation errors typically being in the 2% range after the initial transient from initial condition errors. Since the initial SoC value can be stored in memory from previous history, the initial transient errors are not very important. The performance of the observer was also compared with that of EKF and UKF whose gains vary continuously with operating conditions. The constant gain nonlinear observer provided significantly better performance than the varying-gain EKF and also a little better compared to the UKF, in addition to having advantages of guaranteed global convergence properties and lower computational effort.

The contributions of this chapter are the development of a widely applicable nonlinear observer design method that is especially useful for SoC estimation, since nonlinear output equations and the presence of hysteresis are both often encountered in lithium-ion batteries.

Chapter 6
Estimation of the Basic Reproduction Number for the COVID-19 Pandemic in Minnesota

6.1 Introduction

The COVID-19 infections were first reported in December 2019 in Wuhan, China and subsequently spread rapidly around the world. The successful development of vaccines in recent months promises an eventual recovery for the world from the disease. However, mutations of the involved SARS-Cov-2 virus still present an unknown danger. Furthermore, the world has experienced a significant number of other infectious viral outbreaks during the last 20 years, including the SARS, MERS, and Ebola epidemics [88]. Hence, there is significant motivation to understand the dynamics of how these diseases spread in populations and to develop techniques to control their spread [89], [90].

A number of research articles have recently explored development of mathematical models to represent the dynamics of different agents involved in the spread of the COVID-19 disease. The models attempt to describe the evolution of infected numbers of the population, as well as hospitalized, recovered and susceptible numbers. Most models are compartmental models, also known as *SIR* models, based on an assumption that the population size is constant [91]. Members of the population are classified into three compartments, namely *S*-susceptible, *I*-infected and *R*-removed. Susceptible people are

those lacking immunity and therefore susceptible but not yet infected. An individual in group S can move to group I by infection possibly caused by proximity to an infected individual. Finally, an infected individual fully recovered from the disease or deceased will be moved from the group I to the group R. The summation of these three compartments in the SIR model remains constant and equals the total population N. An improvement on the SIR model is the SEIR model [92]. In the SEIR model a fourth group denoted as Exposed (E) is added as a transition group between the groups S and I. The E group is the population that has been infected with the virus but is not yet in an infectious stage capable of transmitting the virus to others. The addition of the compartment E has been shown to improve model accuracy in data from a number of epidemics [93], [94].

Recently, authors from the control systems community have proposed the use of feedback control to mitigate the spread of the COVID-19 epidemic [95]. In that work, the authors use the SEIR model to show that a simple feedback law can manage the response to the pandemic for maximum survival while containing the damage to the economy. One approach to mitigate the spread of the disease while also trying to reduce economic shutdown is to control the numbers of hospitalized people to a desired number based on available hospital capacity. This ensures that the hospital system is not overwhelmed while avoiding unnecessary shutdowns [95], [96]. Another approach to mitigation is through the recognition of a parameter R_0 called the basic reproduction parameter [97]. It has been shown in multiple papers using the SEIR dynamics that a value of $R_0 < 1$ ensures that the disease decreases in the population and in fact reduces exponentially fast [94], [96], [97]. Recent papers have proposed the control of R_0 to a value below 1 as the approach to modulate disease spread prevention measures [95].

This chapter develops an observer to estimate the value of R_0 in real-time. Previous papers had assumed that the value of R_0 was available for feedback [95], while in fact the typically available measured variables are only the number of diagnosed infections, number of hospitalizations and number of deaths. The importance of this work is that an ability to estimate the real-time value of the reproduction parameter R_0 can assist both the analysis of the disease spread numbers as well as the modulation of mitigation measures to bring the disease evolution dynamics into a stable reducing region.

The outline of the rest of this chapter is as follows. Section 6.2 develops a dynamic model for the COVID-19 disease spread dynamics. A cascaded observer design to estimate both the states and the basic reproduction number is introduced in Section 6.3. The estimated results using the observer for the disease spread dynamics in Minnesota are then presented in Section 6.4. Section 6.5 presents the conclusions.

6.2 Infectious Disease Dynamic Model

6.2.1 Proposed Model

A generalized SEIR model enhanced with additional states is used to describe the dynamic system governing the infectious disease spread dynamics. The system equations can be expressed as

$$\frac{dS}{dt} = -\frac{\beta S(t)\mu I(t)}{N} \tag{6.1}$$

$$\frac{dE}{dt} = \frac{\beta S(t)\mu I(t)}{N} - \alpha E(t) \tag{6.2}$$

$$\frac{dI}{dt} = \frac{\alpha E(t)}{\mu} - \gamma I(t) - \epsilon I(t) \tag{6.3}$$

$$\frac{dH}{dt} = \epsilon\mu I(t) - \rho_{rec} H(t) - \rho_{ICU} H(t) + q_{imp} Z(t) \tag{6.4}$$

$$\frac{dZ}{dt} = \rho_{ICU} H(t) - q_{imp} Z(t) - q_{death} Z(t) \tag{6.5}$$

$$\frac{dR}{dt} = \gamma\mu I(t) + \rho_{rec} H(t) \tag{6.6}$$

$$\frac{dD}{dt} = q_{death} Z(t) \tag{6.7}$$

This generalized model includes seven states: Susceptible population (*S*), Exposed population (*E*), detected Infected population (*I*), number of patients in Hospital but not in ICU (*H*), number of patients in ICU (*Z*), infected population who have recovered (*R*), and infected population who have passed away (*D*). It is assumed that the summation of these

states will be equal to the total population (N).

$$S + E + I + H + Z + R + D = N \tag{6.8}$$

This generalized model, since it has more states and measurements compared to traditional SEIR models, will result in a more accurate and reliable estimation of the system [98]. Note that, this model is nonlinear and requires more than simple linear observer design schemes for estimating its states.

The model parameters which determine the epidemic dynamics include the infection rate (β), inverse of average latent time (α), cure rate (γ), hospitalization rate (ϵ), recovery rate (ρ_{rec}), ICU rate (ρ_{ICU}), and mortality rate (q_{death}). Our generalized SEIR model also proposes a new parameter (μ) which signifies the ratio between the real and detected infected population.

$$I_{true} = \mu\, I \tag{6.9}$$

This relationship accounts for the difference between the total infected and the diagnosed population.

Assumptions: Though the current model is more sophisticated than the traditional SEIR model, some simplifying assumptions are still made. These include:

- The studied population is isolated from neighboring populations.
- The insusceptible population (the patients who have recovered from the disease) is considerably smaller than the total population.
- The number of patients in need of hospitalization or ICU beds does not exceed the capacity of the healthcare system.

6.2.2 Minnesota Data

To train the model and determine its parameters, a six-month data set [99] was considered. This data includes numbers of infected, hospitalized, ICU admissions, recovered, and deaths. In other words, we have five of the seven states as measurements. The publicly reported date starts from March 21st of 2020 and ends on August 27th of 2020.[1]

[1] It is to be noted that after this date the style of the reported data changed, and the new style was not compatible with the model used in this chapter.

6.2.3 Least-Squares Parameter Determination

To find the model parameters, it is necessary to notice that some parameters change over time and we cannot fit constant parameters for the whole time period. Specifically, the infection rate β changes due to social distancing orders and the parameters ϵ and μ vary due to increase in testing. Hence, we adopted the approach to divide the time domain into piecewise periods of time and keep these three parameters constant in each piecewise period to achieve an acceptable fitted model.

To this end, the second derivative of the infected population state *I* was used to split the time domain into piecewise intervals. The reasoning behind this strategy is that, as can be inferred from (6.2) and (6.3), the parameter β is related to the second derivative of *I*. Specifically, by combining (6.2) and (6.3) we have:

$$\frac{\partial^2 I}{\partial t^2} = \beta\left(\frac{\alpha SI}{N}\right) + other\ terms$$

Hence, a considerable change in $\frac{\partial^2 I}{\partial t^2}$ can be equivalent to a significant change in β. Accordingly, to find the numerical value of $\frac{\partial^2 I}{\partial t^2}$, the following filtered derivative equation was used:

$$\frac{d}{dt}\begin{bmatrix} I_f \\ \dot{I}_f \\ \ddot{I}_f \end{bmatrix} = \begin{bmatrix} 0 & 1 & 0 \\ 0 & 0 & 1 \\ -\frac{1}{\tau^3} & -\frac{3}{\tau^2} & -\frac{3}{\tau} \end{bmatrix}\begin{bmatrix} I_f \\ \dot{I}_f \\ \ddot{I}_f \end{bmatrix} + \begin{bmatrix} 0 \\ 0 \\ \frac{1}{\tau^3} \end{bmatrix} I \tag{6.10}$$

where $\ddot{I}_f$ is the filtered second derivative of infected population. Note that equation (6.10) is the state space representation of the filter $I_f = \frac{I}{(1+\tau s)^3}$. By picking $\tau = 0.3$ and utilizing forward finite difference method to find the initial condition, $\ddot{I}_f$ was calculated and the result is shown in Figure 6-1.

As can be seen in this figure, the time domain is roughly divided into regions with positive and negative signs (as a measure for classifying large changes) of $\frac{\partial^2 I}{\partial t^2}$. The piecewise time periods with constant parameters, hence, were chosen as [0-35], [35-70], [70-105], and [105-160] days after March 21st.

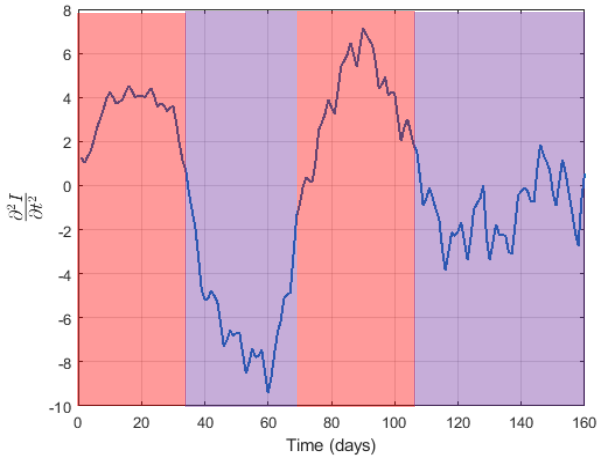

Figure 6-1. The time domain is divided based on the sign of the second derivative of infected population.

To fit the model using all of the existing data set, a least- squares method was utilized [100]. To improve the fitting, different weights were used for the different variables. Since the values of H and Z are much smaller than the other states, a higher weight was given to them ($W_i = 10$). Additionally, since R is not going to be utilized in the observer design, a smaller weight was chosen for it ($W_i = 0.01$).

Furthermore, since the incubation period has been reported to be between 2 to 14 days [101], it was assumed that the average latent time is within the interval of $\alpha^{-1} \in [0.1,0.2]$. The resulting model along with the actual data is presented in Figure 6-2, Figure 6-3,Figure 6-4, and Figure 6-5. As can be seen, the generalized SEIR model accurately reconstructs the data. The susceptible state is also presented in Figure 6-6. As can be seen in the figure, as more of the population gets infected, the susceptible population decreases.

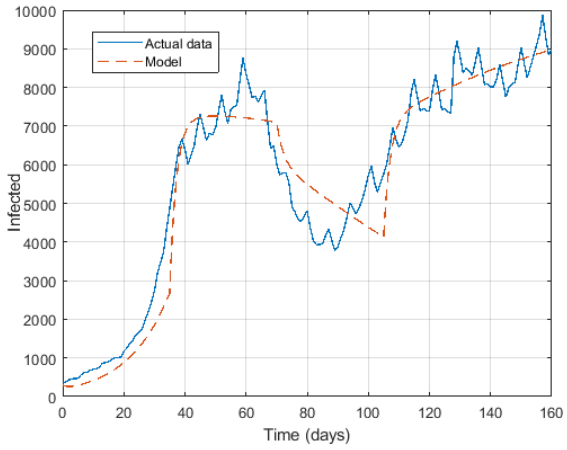

Figure 6-2. The fitted model of the infected population and infected numbers from the data

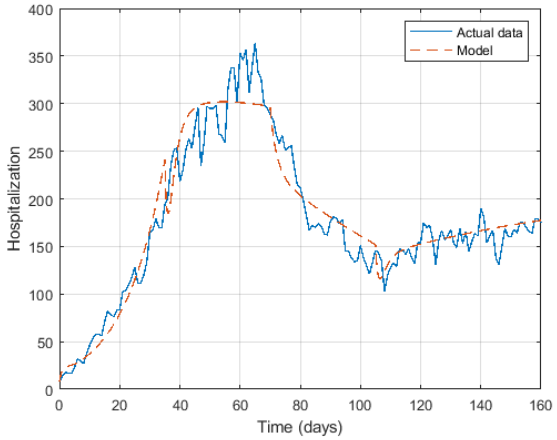

Figure 6-3. The fitted model of the hospital patients and actual hospitalization numbers

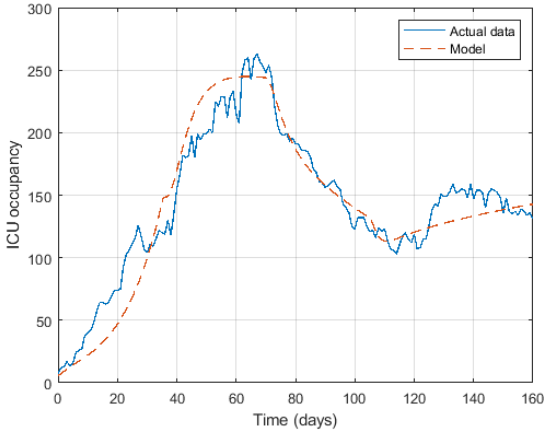

Figure 6-4. The fitted model of ICU patients and actual patients admitted to ICU

The resulting parameters of the model are presented in Table 6-1. CVID-19 spread system parameters. As was stated, all the parameters are kept constant for the whole time except for parameters $\beta, \epsilon,$ and, μ which were constant in each piecewise interval. As can be seen, the infection rate β decreases after the first time period due to the Minnesota's stay-at-home order on March 27th. The effect of increase in prevalence of COVID testing also can be seen in reduction of μ after the first 35 days.

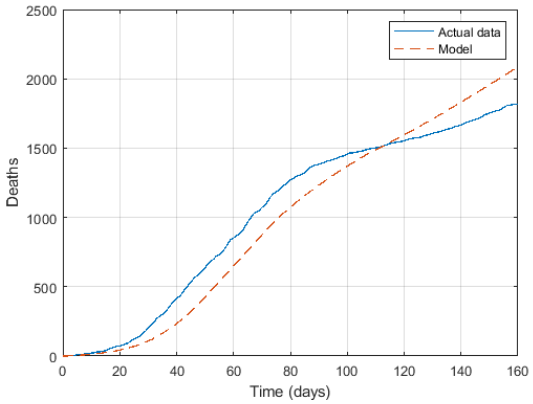

Figure 6-5. The fitted model of dead population and actual number of deaths

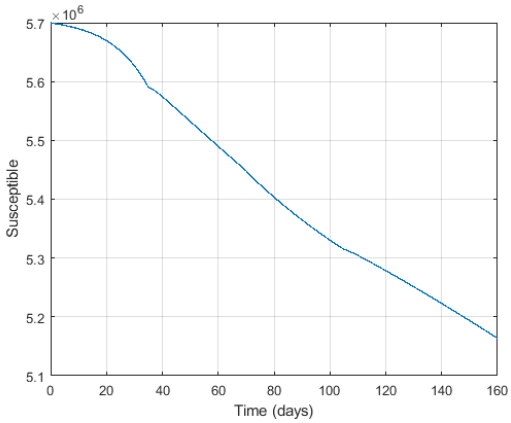

Figure 6-6. Susceptible population according to the model

6.3 Cascaded Observer Design

The design of the overall estimation system is motivated by the following aspects of the dynamic system:

i) Since *H, Z,* and *D* are measured, equations (6.4), (6.5), and (6.7) can be used to estimate μ.

ii) Once μ is known, with a known I_{true} , the infection rate β can be estimated using (6.1) and (6.2). In consequence, a cascaded observer is used to estimate the infection rate and eventually R_0. The first observer uses the measurements of $H, Z,$and D as states and I as input to create an estimate for μ. Then by utilizing μ, the true infected population number is calculated, and the infection rate β is estimated. A schematic of the cascaded observer is presented in Figure 6-7.

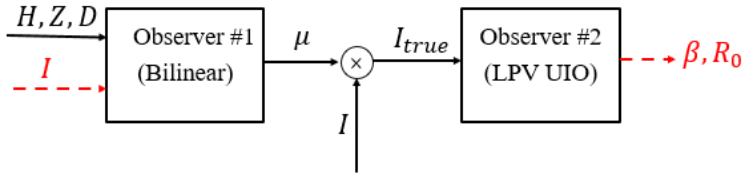

Figure 6-7. Schematic of cascaded observer

Table 6-1. CVID-19 spread system parameters

Parameters	0-35 days	35-70 days	70-105 days	105-160 days
γ	0.2388	same	same	same
β	0.4534	0.2619	0.2378	0.2846
ϵ	0.0125	0.0166	0.0100	0.0139
ρ_{rec}	0.8409	same	same	same
ρ_{ICU}	0.1666	same	same	same
q_{imp}	0.1116	same	same	same
q_{death}	0.0925	same	same	same
α	0.1969	same	same	same
μ	7.2959	2.3050	3.3045	1.3081

6.3.1 Bilinear Observer

To estimate the ratio μ between actual and detected infected population, we consider it to be a state and assume its derivative to be zero.

$$\frac{d\mu}{dt} = 0 \tag{6.11}$$

Using (6.4), (6.5), (6.7), and (6.11), the system for observer #1 is in the following bilinear form [102]:

$$\dot{x} = Ax + Bxu \tag{6.12}$$
$$y = Cx$$

where the states are $x = [H, Z, D, \mu]^T$, the input $u = I$,

$A = \begin{bmatrix} -\rho_{ICU} - \rho_{rec} & q_{imp} & 0 & 0 \\ \rho_{ICU} & -q_{imp} - q_{death} & 0 & 0 \\ 0 & q_{death} & 0 & 0 \\ 0 & 0 & 0 & 0 \end{bmatrix}$, $B = \begin{bmatrix} 0 & 0 & 0 & \epsilon \\ 0 & 0 & 0 & 0 \\ 0 & 0 & 0 & 0 \\ 0 & 0 & 0 & 0 \end{bmatrix}$, and $C = \begin{bmatrix} 1 & 0 & 0 & 0 \\ 0 & 1 & 0 & 0 \\ 0 & 0 & 1 & 0 \end{bmatrix}$.

Let the state observer be given by:

$$\dot{\hat{x}} = A\hat{x} + B\hat{x}u + L(y - C\hat{x}) \tag{6.13}$$

Let the estimation error be $\tilde{x} = x - \hat{x}$. The estimation error dynamics then can be found by subtracting (6.13) from (6.12):

$$\dot{\tilde{x}} = (A + Bu - LC)\tilde{x} \tag{6.14}$$

Note that due to the bilinear nature of the system, the closed-loop matrix in (6.14) is a function of the known input u.

Theorem 6.1. If the Linear Matrix Inequalities (6.15) have a feasible solution, the resulting observer gain L guarantees that the observer (6.13) is globally exponentially stable. Here $P > 0$ is a positive definite matrix and u_{min} and u_{max} are the lower and upper bound on the input ($u_{min} < u < u_{max}$), and σ is a diagonal matrix that determines the convergence rate.

$$(A + Bu_{max} - LC)^T P + P(A + Bu_{max} - LC) + \sigma P \sigma \leq 0 \tag{6.15}$$
$$(A + Bu_{min} - LC)^T P + P(A + Bu_{min} - LC) + \sigma P \sigma \leq 0$$

Proof: Consider $V = \frac{1}{2} x^T P x$ as the candidate for the Lyapunov function, with $P > 0$. By utilizing (6.14) the derivative of Lyapunov function will be:

$$\dot{V} = \dot{\tilde{x}}^T P\tilde{x} + \tilde{x}^T P\dot{\tilde{x}} = \tilde{x}^T(A + Bu - LC)^T P\tilde{x} + \tilde{x}^T P(A + Bu - LC)\tilde{x}$$

To guarantee stability, $\dot{V} \leq 0$ could be ensured. To achieve exponential stability $\dot{V} + \tilde{x}^T \sigma P \sigma \tilde{x} \leq 0$ can be used instead, where $\sigma > 0$ and is defined as:

$$\sigma = \begin{bmatrix} \sigma_1 & 0 & 0 & 0 \\ 0 & \sigma_2 & 0 & 0 \\ 0 & 0 & \sigma_3 & 0 \\ 0 & 0 & 0 & \sigma_4 \end{bmatrix} \tag{6.16}$$

The convergence rate in this case will be at least equal to $\frac{\min(\sigma_i^2)\lambda_{min}(P)}{2}$ where $\lambda_{min}(.)$ denotes the minimum eigenvalue of the matrix.

Hence, the LMI to be satisfied will be:

$$(A + Bu - LC)^T P + P(A + Bu - LC) + \sigma P \sigma \leq 0 \tag{6.17}$$

Any control input $u(t)$, $u_{min} \leq u(t) \leq u_{max}$, can be expressed as

$$u(t) = \delta u_{min} + (1 - \delta)u_{max}, \qquad 0 \leq \delta \leq 1 \tag{6.18}$$

with time-varying δ.

Using (6.18), LMI (6.17) can be written as:

δ [$(A + Bu_{min} - LC)^T P + P(A + Bu_{min} - LC) + \sigma P \sigma] + (1 - \delta)[(A + Bu_{max} - LC)^T P + P(A + Bu_{max} - LC) + \sigma P \sigma] \leq 0$

Hence, if both LMIs in (6.15) are satisfied, the constant solution *P* and the resulting gain *L* will ensure that the observer (6.13) is globally exponentially stable.

6.3.2 Unknown Input Observer for a Linear Parameter Varying system

To estimate the infection rate, we start with (6.2) and (6.3). If it is assumed that $S \approx N$ (the susceptible population is very large compared to the other states), then using (6.9) the system will be:

$$\begin{aligned} \frac{dE}{dt} &= \beta I_{true} - \alpha E \\ \frac{d\, I_{true}}{dt} &= \alpha E - \gamma I_{true} - \epsilon I_{true} \end{aligned} \tag{6.19}$$

The system, therefore, can be expressed as

$$\dot{x} = Ax + D_\rho\, d \tag{6.20}$$
$$y = Cx$$

where $x = [\, E\ I_{true}]^T, A = \begin{bmatrix} 0 & -\alpha \\ \alpha & \gamma + \epsilon \end{bmatrix}, C = [0\ \ 1],\ \ D_\rho = \begin{bmatrix} y \\ 0 \end{bmatrix}$, and $d = \beta$ is an unknown input.

Theorem 6.2. The observer in the form of

$$\dot{\hat{x}} = \left(A - LC - Q_\rho M_{r\rho}\right)\hat{x} + Q_\rho y^{(r)} + Ly \tag{6.21}$$

is asymptotically stable and the estimate of the unknown input

$$\hat{d} = \left(M_{(r-1)\rho} D_\rho\right)^{-1} (y^{(r)} - M_{r\rho}\hat{x}) \tag{6.22}$$

converges toward the true value if the eigenvalues of the matrix $(A - LC - Q_\rho M_{r\rho})$ are all negative. Here *r* is the relative degree of the system, $y^{(n)}$is the n^{th} derivative of the output, $Q_\rho = D_\rho\left(M_{(r-1)\rho} D_\rho\right)^{-1}$, and $M_{i\rho}$can be calculated from

$$y^{(i)} = M_{i\rho} x, \qquad 1 \le i < r \tag{6.23}$$
$$y^{(r)} = M_{r\rho} x + M_{(r-1)\rho} D_\rho d\,, \qquad i = r$$

Proof: [103], [104]

6.4 Estimation Results

To use the first observer for the bilinear system and find μ, the convergence rate in (6.16) is chosen as $\sigma^2 = 10^{-3}\begin{bmatrix} 5 & 0 & 0 & 0 \\ 0 & 1000 & 0 & 0 \\ 0 & 0 & 100 & 0 \\ 0 & 0 & 0 & 10 \end{bmatrix}$. By solving the LMIs (6.15) numerically using the YALMIP toolbox [86] the observer gain is found to be $L = \begin{bmatrix} 20.26 & 35.11 & 49.34 \\ 1.38 & 1.93 & 2.85 \\ 1.51 & 2.54 & 3.49 \\ 0.046 & 0.076 & 0.11 \end{bmatrix}$.

It is to be mentioned that the matrix B is dependent on ϵ, but ϵ changes in each piecewise interval. To deal with this problem, the gain is designed for one interval and is checked for other intervals to satisfy the feasibility of LMIs (6.15). The estimated value of the ratio between the actual and detected infected population along with its previous constant values

from the least-squares method is presented in Figure 6-8.

The relative degree of the system (6.19) with regard to unknown input is $r = 2$. Hence, the observer (6.21) will be:

$$\dot{\hat{x}} = \left(A - LC - Q_\rho CA^2\right)\hat{x} + Q_\rho \ddot{y} + Ly \tag{6.24}$$

From equations in (6.23) and since matrix A is not parameter varying, we have $M_{1\rho} = CA$ and $M_{2\rho} = CA^2$. Hence, resulting from (6.22), the estimate of infection rate can be calculated from:

$$\hat{\beta} = \left(CA\begin{bmatrix} I_{true} \\ 0 \end{bmatrix}\right)^{-1}(\ddot{I}_{true} - CA^2\hat{x}) \tag{6.25}$$

where $\ddot{I}_{true}$ is calculated numerically using (6.10) with the assumption of small rate of change in μ. The gain $L = \begin{bmatrix} 1.5 \\ 1 \end{bmatrix}$ satisfies the Theorem 6.1 for all the piecewise time intervals. The estimated infection rate β along with its constant values from the least-squares method is presented in Figure 6-9.

In general, as can be seen in Figure 6-9 and Figure 6-10, the estimated real-time values μ and β match well with the least-squares values obtained from the complete data set. However, the observer estimates do vary more with time than the least-squares results. To find the basic production number, the following equation is used.

$$R_0 = \frac{\beta}{\epsilon + \gamma} \tag{6.26}$$

The resulting estimate of R_0 is presented in Figure 6-10. As can be seen in Figure 6-10, not only the result of social distancing order from March 27th is visible[2], but also the increase of R_0 as a result of loosening of the restrictions on May 18th (day 58 in the figure) [3] by "Safely Reopening Minnesota's Economy" is also detectable. The mass demonstrations during the summer of 2020 could also have had an effect in increase of R_0 between May 26th and June 7th (days 66-78 of Figure 6-10). The decline in R_0 around the day 90 could be a result of decrease in the protests [105]. It needs to be mentioned that the correlation between the social protests and the rise in COVID-19 spread is questioned in

[2] State of Minnesota Executive Department. (2020, March 25). Emergency executive order 20–20.
[3] State of Minnesota Executive Department. (2020, May 13). Emergency executive order 20–56.

multiple works [106], [107] and is not a specific claim that this work makes.

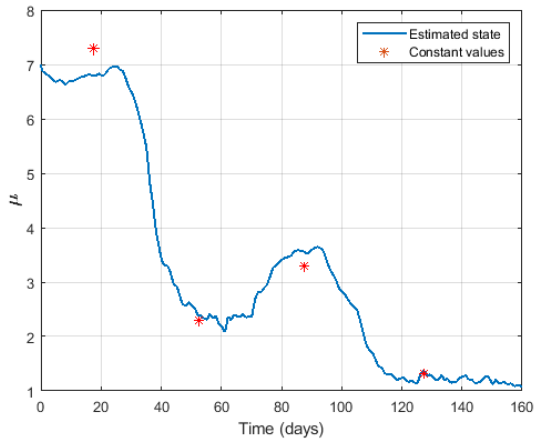

Figure 6-8. Ratio between the actual and detected infected population.

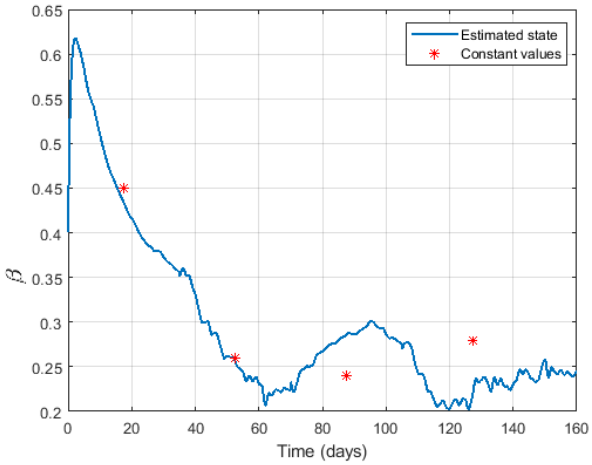

Figure 6-9. Infection rate parameter β

6.5 Conclusions

This chapter considered the dynamics of the COVID-19 pandemic and real-time estimation of the basic reproduction number as a key variable for controlling the spread of the disease. By adding variables on hospitalizations, ICU admissions, and number of deaths, a nonlinear generalized SEIR model was developed. A least-squares method was utilized

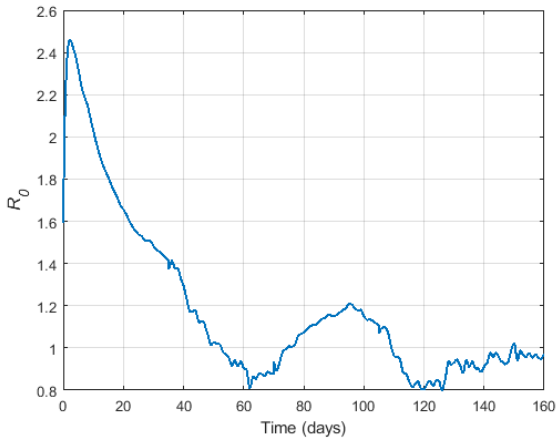

Figure 6-10. Basic reproduction number

to find the parameters of the system based on the complete data set of 6-month statistics published by the Minnesota Department of Health.

A cascaded observer system, consisting of a bilinear observer and an unknown input observer, was used to estimate the real-time values of the true infected population, the infection rate, and the basic reproduction number.

The resulting real-time estimates matched well with the least-squares values obtained from the whole data set. The real-time estimates provide timely information and could be utilized to control the spread of the disease. For instance, the reproduction number could be controlled to a value below 1 by fine-tuning social distancing measures and lock-downs, so that economic pain is minimized while the disease dynamics are still maintained to be in a stable region.

Chapter 7
Analysis of the Performance of a H_∞ Nonlinear Observer and Nonlinear Kalman Filters in Presence of Non-Gaussian Disturbances

7.1 Introduction

Accurate state estimation is necessary for a gamut of applications involving dynamic systems. This need could be due to the requirements for feedback control, fault detection, or state of health estimation [108].

Model-based state estimation methods can be divided into two major categories: probabilistic and deterministic. In this work, we refer to the former as filters and the latter as observers.

Many popular probabilistic methods are based on the Kalman Filter (KF) and its extensions. In the KF method [109], which is designed for linear systems, expected value and covariance of the states get propagated through time. It has been shown that in the case of linear dynamic systems with Gaussian zero-mean disturbances, the KF provides the estimation with the lowest mean square error [110].

The Extended Kalman Filter (EKF) is a modification of the linear KF with the goal to

make it applicable to nonlinear systems [111]. Consider a nonlinear system in the form:

$$\dot{x} = f(x,u,t) + Bw(t) \tag{7.1}$$
$$y = h(x,t) + Dv(t)$$

where $w(t) \sim \mathcal{N}(0,Q)$ and $v(t) \sim \mathcal{N}(0,R)$ are the Gaussian noise inputs to the system. The estimated states are calculated as:

$$\dot{\hat{x}} = f(\hat{x},u,t) + L\big(y - h(\hat{x},t)\big)$$
$$L = \mathcal{P}\mathcal{H}^T(DRD^T)^{-1} \tag{7.2}$$
$$\dot{\mathcal{P}} = \mathcal{F}\mathcal{P} + \mathcal{P}\mathcal{F}^T + BQB^T - \mathcal{P}\mathcal{H}^T(DRD^T)^{-1}\,\mathcal{H}\mathcal{P}$$

where $\mathcal{P}$ is the covariance of the states, and

$$\mathcal{F} = \frac{\partial f}{\partial x}\Big|_{\hat{x}} \quad ,\mathcal{H} = \frac{\partial h}{\partial x}\Big|_{\hat{x}} \tag{7.3}$$

As can be seen in (7.3), the partial derivatives of the nonlinear functions are calculated using the estimated states in order to obtain the linear system at the operating points. Due to the consequent inaccuracies, this has been shown to cause major errors and sometimes even instability [112] [113]. Furthermore, the assumption for Gaussian noise disturbance still prevails in EKF.

In the Unscented Kalman Filter (UKF), instead of linearly approximating the nonlinear functions, the mean and covariance of the states are directly approximated when a nonlinear function is applied to them [16]. This is achieved by selecting a few representative sample states around the estimate, commonly known as sigma points:

$$\hat{x}_\sigma^{(i)} = \hat{x} \pm (\sqrt{n\mathcal{P}})_i^T \quad i = 1, \dots, n \tag{7.4}$$

where n is the order of the system, $\mathcal{P}$ is the covariance matrix, and $(.)_i$ signifies the ith row of a matrix. These sigma points, then, are mapped using the nonlinear functions and the mean and covariance of the mapped points are approximated.

While this method increases the accuracy of the estimation in highly nonlinear systems, the amount of this improvement wanes in the presence of non-Gaussian disturbances [15]. Furthermore, as (7.4) shows the represented sigma points are still chosen around the estimated state, and even though the covariance matrix takes the reliability of the estimate into account, a sharp non-Gaussian disturbance can be quite detrimental to this method.

In the deterministic framework, observers for state estimation have been a major topic of research. While designing an observer for a linear system mostly focuses on the stability of the poles of the linear estimation error dynamics, designing a nonlinear observer requires Lyapunov based techniques. High-gain observers [4] and LMI observer designs based on Lipschitz [114] and Jacobian bounds [47] have been investigated for different forms of nonlinearities.

The goal of H_∞ control is to minimize the worst-case effect of the disturbances on the tracking error signal of dynamic systems [115]. This is done by minimizing this effect in Hardy space, or choosing the control gain to minimize the H_∞norm of the transfer function between error signal and the disturbance:

$$\left\|\frac{e}{w}\right\|_\infty = \sup_\omega \bar{\sigma}\left\{\frac{e}{w}(j\omega)\right\} \tag{7.5}$$

where e is the error signal and w is the input disturbance.

Nonlinear observers can be combined with the H_∞ criterion to minimize the effect of disturbance on the estimation state error. The goal is to design an observer that guarantees the H_∞ criterion:

$$\|\tilde{x}\|_{\mathcal{L}_2} \leq \sqrt{\mu\|w\|^2{}_{\mathcal{L}_2} + \upsilon\|\tilde{x}_0\|_2{}^2} \tag{7.6}$$

where μ is the attenuation coefficient, $\nu > 0$, and $\tilde{x} = x - \hat{x}$ is the estimation error. Here, $\|.\|_{\mathcal{L}_2}$ represents the signal 2-norm and $\|.\|_2$ signifies the 2-norm of a vector. The only assumption for the disturbance signal is that it should be $\mathcal{L}_2$ bounded, i.e., $\int_0^{+\infty}\|w(t)\|_2^2\,dt < \infty$.

Using Lyapunov analysis, as will be shown later, it is possible to ensure asymptotic stability and to calculate a bound for 2-norm of the error vector prior to performing the estimation. This ability can be quite useful for guaranteeing stability for systems that are observable in a limited set.

The H_∞ concept has been combined by EKF [116]and UKF [117] to increase the robustness of these filters. While this modification has improved the performance of these filters, linearizing the system around the estimated states for EKF and choosing the sigma points around them for UKF still take place in these modified methods. Furthermore, even

though these filters try to bound the rms of estimation error by using the suboptimal formulation of H_∞, they cannot guarantee any bounds on maximum value for the estimation error.

In this work, we will use Lyapunov analysis to derive an LMI approach for designing a H_∞ observer and introduce a weight matrix to tune its performance. The maximum estimation error bound is then derived using the resulting Lyapunov function and its validity shown through simulations.

Additionally, we will compare the performance of the H_∞nonlinear observer with those of EKF and UKF in three different applications: Magnetic position estimation, State of charge estimation for Li-ion batteries, and Vehicle motion estimation. These applications will show that even though UKF generally performs equally well or slightly better in presence of Gaussian noise disturbances, the H_∞ observer offers superior estimation for $\mathcal{L}_2$ bounded pulse disturbances. This superior estimation can be shown in the maximum error and rms error.

The outline of this chapter is as follows. Section 7.2 describes the formulation of the H_∞ nonlinear observer, introduces a weighted version of this observer, and presents the bounds on the estimation error based on the bounds of unknown disturbance. Section 7.3 compares the performance of the designed observer with EKF and UKF in presence of Gaussian and pulse disturbances for two applications with linear dynamics and nonlinear output functions: magnetic position estimation, state of charge estimation of batteries. Section 7.4 does this for an application with nonlinear dynamics and linear output functions: vehicle motion estimation. Conclusions are presented in Section 7.5 .

7.2 H_∞Nonlinear Observer Formulation

Consider the nonlinear system in the form:

$$\dot{x} = Ax + Ff(Ex) + Bw + Gu \tag{7.7}$$
$$y = Cx + h(Jx) + Dw$$

with

$$f(Ex) = \begin{Bmatrix} f_1(E_1x) \\ \vdots \\ f_p(E_px) \end{Bmatrix}, f(Ex) = \begin{Bmatrix} h_1(J_1x) \\ \vdots \\ h_m(J_mx) \end{Bmatrix}$$

where $x \in \mathbb{R}^n, y \in \mathbb{R}^m, u \in \mathbb{R}^r$ are states, outputs, and inputs of the system respectively and $w \in \mathbb{R}^q$ is an unknown disturbance. Also, $f_i: \mathbb{R} \longrightarrow \mathbb{R}\ i = 1, \dots, p$ and $h_j: \mathbb{R} \longrightarrow \mathbb{R}\ i = 1, \dots, m$ are continuously differentiable functions and matrices $A, F, B, G, C,$ and D have the proper dimensions.

Furthermore, U_i and V_i are defined as lower and upper bounds of the $\frac{\partial f(E_ix)}{\partial (E_ix)}$ and $U = diag(U_i), V = diag(V_i)$ and likewise M and N are defined as bounds of $\frac{\partial h(J_ix)}{\partial (J_ix)}$ put on a diagonal of matrices. Furthermore, H_∞ criterion (7.6) can be satisfied in the Lyapunov analysis framework. In this section, the required linear matrix inequalities for this purpose are derived, and the case where different weights can be given to each state is analyzed. Furthermore, the bounds of estimation error as a function of the bounds on the unknown disturbance is calculated.

7.2.1 Design of H_∞ Nonlinear Observer

Theorem 7.1. Consider a system with nonlinear dynamics and nonlinear output functions in the form of (7.7) and an observer in the form:

$$\dot{\hat{x}} = A\hat{x} + Ff(E\hat{x}) + Gu + L(y - \hat{y}) \tag{7.8}$$
$$\hat{y} = C\hat{x} + h(J\hat{x})$$

If $L \in \mathbb{R}^{m \times n}, P \in \mathbb{R}^{n \times n} > 0, \mu > 0$ can be found that satisfies the following LMI, then the observer (7.8) is stable and the H_∞ criterion (7.6) will be satisfied.

- $\min \mu$

$$\begin{bmatrix} (A-LC)^T P + P(A-LC) + \frac{I}{\alpha} & * & * & * \\ F^T P & 0 & * & * \\ -L^T P & 0 & 0 & * \\ (-LD+B)^T P & 0 & 0 & -\mu I \end{bmatrix} - \begin{bmatrix} E^T UVE + J^T MNJ & * & * & * \\ -\frac{(V+E)E}{2} & I & * & * \\ -\frac{(M+N)J}{2} & 0 & I & * \\ 0 & 0 & 0 & 0 \end{bmatrix} < 0 \qquad (7.9)$$

$$P > 0$$

where $\alpha \in \mathbb{R} > 0$ can be picked arbitrarily.

Thus, by minimizing μ over all possible LMI solutions, disturbance rejection can be optimized.

Proof: Consider the Lyapunov candidate function:

$$V = \tilde{x}^T P \tilde{x} \qquad (7.10)$$

where P is a positive definite matrix. Subtracting (7.8)from (7.7) will result in:

$$\dot{\tilde{x}} = A\tilde{x} + F\tilde{f} + Bw - L\left(C\tilde{x} + \tilde{h} + Dw\right) \qquad (7.11)$$

Taking the derivative of the Lyapunov function will result in:

$$\dot{V} = \dot{\tilde{x}}^T P \tilde{x} + \tilde{x}^T P \dot{\tilde{x}} \qquad (7.12)$$

We can write the derivative of the Lyapunov function in matrix form as:

$$\dot{V} = \begin{bmatrix} \tilde{x} \\ \tilde{f} \\ \tilde{h} \\ w \end{bmatrix}^T \begin{bmatrix} (A-LC)^T P + P(A-LC) & * & * & * \\ F^T P & 0 & * & * \\ -L^T P & 0 & 0 & * \\ (-LD+B)^T P & 0 & 0 & 0 \end{bmatrix} \begin{bmatrix} \tilde{x} \\ \tilde{f} \\ \tilde{h} \\ w \end{bmatrix} \qquad (7.13)$$

where $\tilde{f}(Ex, E\hat{x}) = f(Ex) - f(E\hat{x})$ and $\tilde{h}(Jx, J\hat{x}) = h(Jx) - h(J\hat{x})$.

It can be shown that the following inequality satisfies both H_∞ criterion and negative definiteness of the Lyapunov function [118]:

$$\dot{V} + \|\tilde{x}\|^2 - \mu\|w\|^2 \leq 0 \qquad (7.14)$$

Furthermore, the inequality (7.14) can be written as:

$$\dot{V} + \|\tilde{x}\|^2 - \mu\|w\|^2 = \begin{bmatrix} \tilde{x} \\ \tilde{f} \\ \tilde{h} \\ w \end{bmatrix}^T \begin{bmatrix} (A-LC)^T P + P(A-LC) + I & * & * & * \\ F^T P & 0 & * & * \\ -L^T P & 0 & 0 & * \\ (-LD+B)^T P & 0 & 0 & -\mu I \end{bmatrix} \begin{bmatrix} \tilde{x} \\ \tilde{f} \\ \tilde{h} \\ w \end{bmatrix} \leq 0 \tag{7.15}$$

Using the differential mean value theorem [119], the following matrix inequality holds true:

$$V_1 = \begin{bmatrix} \tilde{x} \\ \tilde{f} \\ \tilde{h} \\ w \end{bmatrix}^T \begin{bmatrix} E^T U V E + J^T M N J & * & * & * \\ -\dfrac{(V+E)E}{2} & I & * & * \\ -\dfrac{(M+N)J}{2} & 0 & I & * \\ 0 & 0 & 0 & 0 \end{bmatrix} \begin{bmatrix} \tilde{x} \\ \tilde{f} \\ \tilde{h} \\ w \end{bmatrix} < 0 \tag{7.16}$$

Using S-Procedure [120], $\dot{V} + \|\tilde{x}\|^2 - \mu\|w\|^2 \leq \alpha V_1$ will guarantee inequality (7.14) if $\alpha > 0$ exists. So, we can write:

$$\begin{bmatrix} (A-LC)^T P + P(A-LC) & * & * & * \\ F^T P & 0 & * & * \\ -L^T P & 0 & 0 & * \\ (-LD+B)^T P & 0 & 0 & -\mu I \end{bmatrix} - \alpha \begin{bmatrix} E^T U V E + J^T M N J & * & * & * \\ -\dfrac{(V+E)E}{2} & I & * & * \\ -\dfrac{(M+N)J}{2} & 0 & I & * \\ 0 & 0 & 0 & 0 \end{bmatrix} < 0 \tag{7.17}$$

Dividing inequality (7.17) by α and absorbing it into the matrix P will result in (7.9).

7.2.2 Weighted H_∞ Criterion for Nonlinear Observer

Sometimes it is necessary to have different weights for each state in the H_∞ criterion. These weights might be necessitated due to different dimensions of the states or their relative priority in observer design. This can be done by multiplying a weight matrix to the

error vector and rederive the LMI. It is to be mentioned that this method, unlike the method proposed by [121] enables us to give different weights to all the states and not just the ones that show up in the Jacobian bound matrices.

Consider the system in (7.7). Defining the weighted error vector:

$$\varepsilon = \Delta\tilde{x} \tag{7.18}$$

where Δ is a positive definite diagonal matrix. Now define the H_∞ criterion as:

$$\|\varepsilon^T\varepsilon\|_{\mathcal{L}_2}^{1/2} = \|\tilde{x}^T\Delta^2\tilde{x}\|_{\mathcal{L}_2}^{1/2} \leq \sqrt{\mu\|w\|^2{}_{\mathcal{L}_2} + \upsilon\|\tilde{\varepsilon}_0\|^2} \tag{7.19}$$

Needless to say, $\varepsilon \to 0$ will result in $\tilde{x} \to 0$. But the weight matrix will manipulate the amount of error in each state.

To find the appropriate LMI, pick the Lyapunov function candidate $V = \varepsilon^T P\varepsilon$.

Since $\dot{\varepsilon} = \Delta\,\dot{\tilde{x}}$

$$\dot{\varepsilon} = \Delta\dot{\tilde{x}} = \Delta A\tilde{x} + \Delta F\tilde{f} - \Delta LC\tilde{x} - \Delta L\tilde{h} + \Delta Bw - \Delta LDw \tag{7.20}$$

By using $\tilde{x} = \Delta^{-1}\varepsilon$ we will have:

$$\dot{\varepsilon} = \Delta A\Delta^{-1}\varepsilon + \Delta F\tilde{f} - \Delta LC\Delta^{-1}\varepsilon - \Delta L\tilde{h} + \Delta Bw - \Delta LDw \tag{7.21}$$

The derivative of Lyapunov function in matrix form:

$$\dot{V} = \begin{bmatrix}\varepsilon\\ \tilde{f}\\ \tilde{h}\\ w\end{bmatrix}^T \begin{bmatrix} P\Delta(\mathrm{A} - LC)\Delta^{-1} - \Delta^{-1}C^TL^T\Delta P & P\Delta F & -P\Delta L & P\Delta(B - LD)\\ * & 0 & 0 & 0\\ * & * & 0 & 0\\ * & * & * & 0\end{bmatrix}\begin{bmatrix}\varepsilon\\ \tilde{f}\\ \tilde{h}\\ w\end{bmatrix} \tag{7.22}$$

Using the differential mean value theorem [119]:

$$V_1 = \begin{bmatrix}\varepsilon\\ \tilde{f}\\ \tilde{h}\\ w\end{bmatrix}^T \begin{bmatrix} \Delta^{-1}(E^TUVE + J^TMNJ)\Delta^{-1} & -\frac{\Delta^{-1}E^T(U+V)}{2} & -\frac{\Delta^{-1}J^T(M+N)}{2} & 0\\ * & \mathrm{I} & 0 & 0\\ * & * & I & 0\\ * & * & * & 0\end{bmatrix}\begin{bmatrix}\varepsilon\\ \tilde{f}\\ \tilde{h}\\ w\end{bmatrix} \tag{7.23}$$

Inequality (7.14) for weighted error can be written as:

$$\dot{V} + \|\tilde{\varepsilon}\|^2 - \mu\|w\|^2 \leq 0 \tag{7.24}$$

Using (7.24) and S-procedure, the observer gain can be found by using the following optimization problem.

- $\min \mu$

$$\begin{bmatrix} P\Delta(\mathrm{A}-LC)\Delta^{-1}-\Delta^{-1}C^{T}L^{T}\Delta P+\dfrac{I}{\alpha} & P\Delta F & -P\Delta L & P\Delta(B-LD) \\ * & 0 & 0 & 0 \\ * & * & 0 & 0 \\ * & * & * & -\mu I \end{bmatrix}$$
$$-\begin{bmatrix} \Delta^{-1}(E^{T}UVE+J^{T}MNJ)\Delta^{-1} & -\dfrac{\Delta^{-1}E^{T}(U+V)}{2} & -\dfrac{\Delta^{-1}J^{T}(M+N)}{2} & 0 \\ * & \mathrm{I} & 0 & 0 \\ * & * & I & 0 \\ * & * & * & 0 \end{bmatrix} \leq 0 \tag{7.25}$$
$$P>0$$

7.2.3 Bounds on Error Estimation

Theorem 7.2 . [122] If an observer is designed so as to satisfy the Lyapunov stability and disturbance rejection conditions and w is an unknown 2-norm bounded vector disturbance, i.e. $w(t) \in R \to R^{p}$ with $\|w(t)\|_2 \leq \eta \ \forall t$, then the following vector-norm bound on the estimation error in the presence of the disturbance is guaranteed:

$$\|\tilde{x}(t)\|_2 \leq \max\left\{\sqrt{\frac{\beta_1}{\beta_2}}\,\|\tilde{x}_0\|_2\, e^{\frac{\left(\frac{\mu}{\gamma}-1\right)t}{\beta_1}}, \sqrt{\gamma}\|w(t)\|_2\right\} \tag{7.26}$$

where $\beta_1 = \lambda_{max}(P),\ \beta_2 = \lambda_{min}(P)$, and $\gamma \geq \mu$.

Proof: At every point in time the vector norm $\|\tilde{x}(t)\|_2$ is either less than or equal to $\sqrt{\gamma}\|w(t)\|_2$ or greater.

- **Case i (greater):** Assume $\|\tilde{x}(t)\|_2 \geq \sqrt{\gamma}\|w(t)\|_2$. Which can be rewritten:

$$\|w\|_2^{\,2} \leq \frac{\|\tilde{x}\|_2^{\,2}}{\gamma} \tag{7.27}$$

Combining the H_∞ criterion (7.14) with (7.27):

$$\dot{V} \leq -\|\tilde{x}\|_2^{\,2} + \mu\|w\|_2^{\,2} \leq \left(\frac{\mu}{\gamma}-1\right)\|\tilde{x}\|_2^{\,2} \tag{7.28}$$

Using $\beta_1 = \lambda_{max}(P),\ \beta_2 = \lambda_{min}(P)$, we will have the bounds for Lyapunov function:

$$\beta_2 \|\tilde{x}\|_2^{\,2} \le V \le \beta_1 \|\tilde{x}\|_2^{\,2} \tag{7.29}$$

Using (7.28)and the right-hand side inequality of (7.29) we will have:

$$\dot{V} \le \left(\frac{\mu}{\gamma} - 1\right) \|\tilde{x}\|_2^{\,2} \le \frac{V}{\beta_1}\left(\frac{\mu}{\alpha} - 1\right) \tag{7.30}$$

After rearranging:

$$\frac{\dot{V}}{V} \le \frac{\left(\frac{\mu}{\gamma} - 1\right)}{\beta_1} \tag{7.31}$$

Taking the integral from 0 – t:

$$\ln V - \ln V_0 \le \frac{\left(\frac{\mu}{\gamma} - 1\right) t}{\beta_1} \tag{7.32}$$

Which can be rearranged as:

$$V \le e^{\frac{\left(\frac{\mu}{\gamma} - 1\right) t}{\beta_1}} V_0 \tag{7.33}$$

Using the bounds from (7.29):

$$\beta_2 \|\tilde{x}(t)\|_2^{\,2} \le e^{\frac{\left(\frac{\mu}{\gamma} - 1\right) t}{\beta_1}} \beta_1 \|\tilde{x}_0\|_2^{\,2} \tag{7.34}$$

which gives us the bound as:

$$\|\tilde{x}(t)\|_2 \le \sqrt{\frac{\beta_1}{\beta_2}}\, \|\tilde{x}_0\|_2\, e^{\frac{\left(\frac{\mu}{\gamma} - 1\right) t}{\beta_1}} \tag{7.35}$$

- **Case ii (smaller)**: $\|\tilde{x}(t)\|_2 < \sqrt{\gamma}\|w(t)\|_2$ [4]

Combining the bounds of these two cases will result in(7.26).

Remark 7.1. It has been known that the Lyapunov-related condition $\dot{V} + \|\tilde{x}\|^2 - \mu\|w\|^2 \le 0$ ensures the signal norm condition

$$\int_0^\infty \|\tilde{x}(t)\|_2^2 dt \le \mu \int_0^\infty \|w(t)\|_2^2 dt \tag{7.36}$$

[4] It is to be noted that this condition relates the vector norms of the estimation error and the disturbance; it should not be confused with (7.6) which relates the signal norms of them.

However, Theorem 7.2 shows that a real-time bound on the vector norm of the estimation error is also obtained from the same Lyapunov design condition.

Remark 7.2. The condition for H_∞ is that $\|w\|_{\mathcal{L}_2}$ is bounded, that does not guarantee the boundedness of $\|w\|_2$. Example: Impulse signal. So, we need to add the following condition as well:

$$\|w(t)\|_2 \leq \eta, \forall t \text{ or } \|\|w(t)\|_2\|_{\mathcal{L}_\infty} = \eta \tag{7.37}$$

Remark 7.3. In the absence of initial error $\tilde{x} = 0$ or at large values of time, the bound can reduced to:

$$\|\tilde{x}(t)\|_2 \leq \sqrt{\mu}\|w(t)\|_2 = \sqrt{\mu}\,\eta \tag{7.38}$$

Remark 7.4. The bound in Theorem 7.2 can be calculated in advance just by the knowledge of the bounds on disturbance vector, while EKF and UKF require solving to attain the covariance of estimated states. Furthermore, those techniques do not provide any bounds on $\|\tilde{x}(t)\|_2$ even after calculating the estimated states.

There are dynamic systems where the stability of observer can only be guaranteed within a limited domain. In such cases, the differential mean value theorem cannot be used to ensure inequality (7.16) if the estimation lies outside that limited domain. Using the bound of estimation error (7.26) can guarantee the stability.

Corollary 7.1. Let the observer (7.8) be designed using Jacobian bounds that are satisfied over the set Ω_2. By designing an H_∞ observer we can have the maximum 2-norm of the estimation error $\xi(t)$ from Theorem 7.2 as:

$$\xi(t) = \max\left\{\sqrt{\frac{\beta_1}{\beta_2}}\,\|\tilde{x}_0\|_2\, e^{\frac{\left(\frac{\mu}{\gamma}-1\right)t}{\beta_1}}, \gamma\|w(t)\|_2\right\}, \text{for } \mu \leq \gamma \tag{7.39}$$

We can define a 2-norm ball:

$$\Omega_\xi(t) = \{a \in \mathbb{R}^n |\ \|a\|_2 \leq \xi(t)\ \} \tag{7.40}$$

The designed observer is guaranteed to be asymptotically stable if the undisturbed states $x \in \Omega_1$ such that

$$\Omega_1 \oplus \Omega_\xi(t) \subset \Omega_2 \tag{7.41}$$

where $\oplus$ denotes the Minkowski sum: $A \oplus B = \{a + b \,|a \in A, b \in B\}$.

Proof: According to the Theorem 7.2 the error norm of the H_∞ observer will always be smaller than $\xi(t)$ and since we have

$$\|\hat{x}(t)\|_2 \leq \|x(t)\|_2 + \|\tilde{x}(t)\|_2 \tag{7.42}$$

we can deduce $\hat{x}(t) \subset \Omega_1 \oplus \Omega_\xi(t) \subset \Omega_2$. Now, since $\Omega_1 \subset \Omega_2$, the Jacobian bounds of $f(Ex)$ and $h(Jx)$ over Ω_2 hold for both x and $\hat{x}$. Hence, by designing an observer using the bounds of Ω_2 the inequality derived from mean value theorem (7.16) is maintained and the resulting LMI (7.17) guarantees asymptotic stability.

In the following two sections, the performance of H_∞ nonlinear observer will be compared with those of the Extended Kalman filter and Unscented Kalman filter in presence of Gaussian noise and pulse disturbances. For this purpose, three different applications are considered. The first two applications have linear dynamics and nonlinear output equations, while the third application has nonlinear dynamics and linear output functions.

7.3 Systems with Nonlinearity in the Output Functions

Magnetic position estimation and Li-ion battery state of charge estimation consist of nonlinear output functions and linear dynamic equations. For each of these applications, first the performance of H_∞ nonlinear observer and Kalman filters are compared only in presence of Gaussian noise, then their performance is analyzed when pulse disturbance is added to the noisy system.

7.3.1 Magnetic Position Estimation on a Pneumatic Actuator

Most hydraulic and pneumatic cylinders contain a permanent magnet attached to the piston. By measuring the magnetic field of this magnet, we can estimate the linear position of the piston with low cost [123]. As shown in Figure. 7-1, a set of spatially separated inexpensive magnetometers are used to measure the magnetic field and a much more expensive LVDT is used to find the true position. The dynamic equations of this system can be stated as:

$$\dot{x} = Ax + Bw$$
$$y = h(Jx) + Dw \tag{7.43}$$
$$x = \begin{bmatrix} z \\ v \\ a \end{bmatrix} A = \begin{bmatrix} 0 & 1 & 0 \\ 0 & 0 & 1 \\ 0 & 0 & 0 \end{bmatrix}, J = [1, 0, 0]$$

where z, v, a are the position, velocity and acceleration of the piston respectively.
In this system two monotonic magnetometer measurements are used (Figure. 7-1). This is achieved by utilizing the same direction measurements of two different magnetometers set up on one side of the actuator.

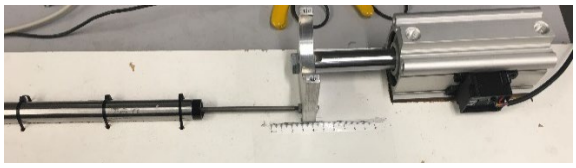

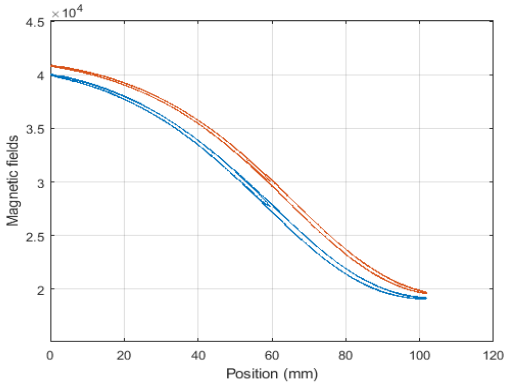

Figure. 7-1. Sensor configuration for magnetic position estimation and the magnetic field outputs

Estimation in the presence of Gaussian disturbances

In this case, experimental data was used and the true values of position was measured using an LVDT. The sdpt3 solver along with YALMIP toolbox [124] was used to solve the optimization problem (7.9) to find the observer gain and $\alpha = 1$. The $B$and D matrices and the resulting observer gain, and the attenuation coefficient was:

$$H_\infty: B = \begin{bmatrix} 0 \\ 0 \\ 10^{-4} \end{bmatrix},\ D = \begin{bmatrix} 0.01 \\ 0.01 \end{bmatrix},\quad L = \begin{bmatrix} -359.8 & -274.9 \\ -323.6 & -247.2 \\ -291.0 & -222.3 \end{bmatrix}, \mu = 3.1 * 10^{-4}$$

The best R and Q covariance matrices for EKF and UKF were found as follows:

$$\text{EKF: } Q = \begin{bmatrix} 0 & 0 & 0 \\ 0 & 0 & 0 \\ 0 & 0 & 1 \end{bmatrix}, R = 10^{-3} \begin{bmatrix} 1 & 0 \\ 0 & 5 \end{bmatrix}$$

$$\text{UKF: } Q = \begin{bmatrix} 0 & 0 & 0 \\ 0 & 0 & 0 \\ 0 & 0 & 1 \end{bmatrix}, R = 10^{-5}\begin{bmatrix} 1 & 0 \\ 0 & 5 \end{bmatrix}$$

To make the estimation results comparable, all three estimation techniques were solved within SIMULINK concurrently. The initial condition error was picked as $\tilde{x}_0 = [-50,0,0]$, and the experimental data was accessed by all the estimators at the same rate. The result of estimation techniques is presented in Figure. 7-2 along with the true position.

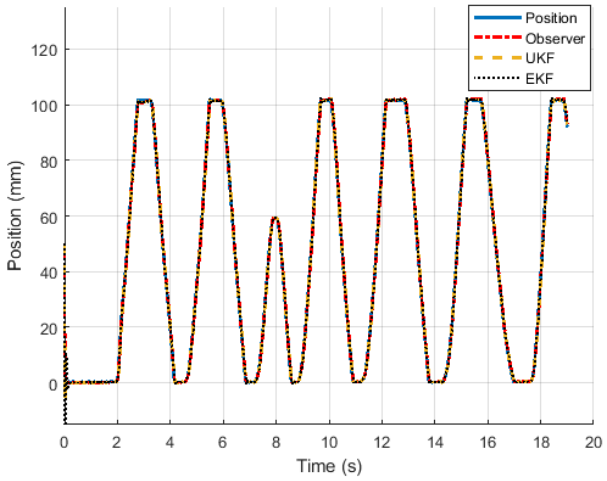

Figure. 7-2. Position estimation of observer, UKF, and EKF along with the actual position measured by LVDT

The maximum estimation error and its root mean square is presented in Table. 7-1.

Table. 7-1. Position estimation error for observer, EKF, and UKF

Estimation method	Max error (mm)	rms error (mm)
Observer	2.70	0.94
UKF	2.66	1.12
EKF	3.05	1.38

As can be seen from Table. 7-1, the nonlinear observer and UKF have relatively similar performances, and both outperform EKF.

Adding pulse disturbances to outputs

In this case, pulse shaped disturbances were artificially added to the outputs of the last section to compare the estimation results of each estimation method. The added disturbances are depicted in Figure. 7-3. Each disturbance was added to one of the outputs. As is apparent, the disturbance signals are $\mathcal{L}_2$ norm bounded and transient. In this particular

application, the disturbances can represent a magnetic field of an external ferromagnetic object.

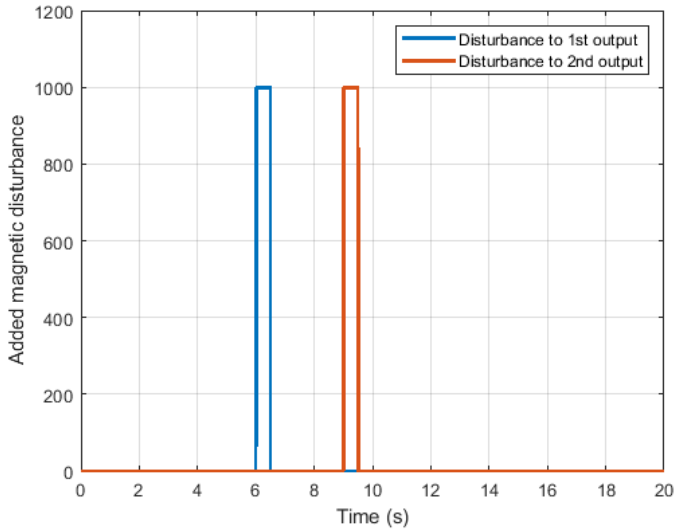

Figure. 7-3. Added pulse disturbances to the magnetic field measurements

It needs to be mentioned that the range of the magnetic outputs is between [20k-40k] and the disturbance is relatively small compared to the measurements as shown in Figure 7-4.

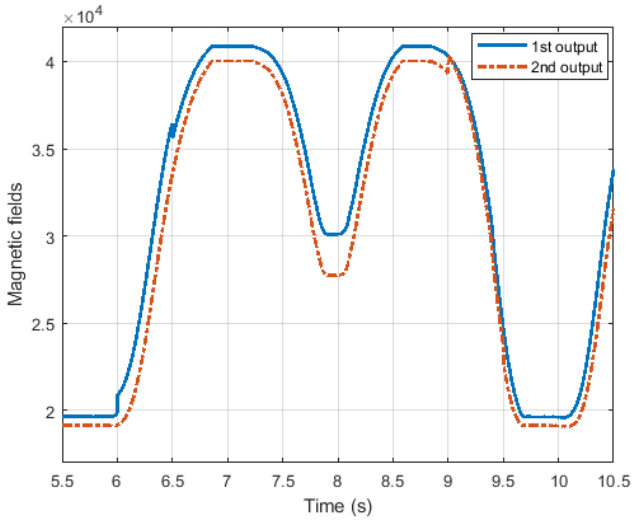

Figure 7-4. Magnetic measurements corrupted by pulse disturbances

Similar to the last section, the nonlinear observer gain was calculated and the best performance of EKF and UKF was found with following covariance matrices:

$$H_\infty: B = \begin{bmatrix} 0 \\ 0 \\ 10^{-4} \end{bmatrix}, \quad D = \begin{bmatrix} 1 \\ 1 \end{bmatrix}, \quad L = 10^3 \begin{bmatrix} -172.7 & -131.9 \\ -33.5 & -25.6 \\ -6.5 & -5.0 \end{bmatrix}, \mu = 3.10$$

$$\text{EKF: } Q = \begin{bmatrix} 0 & 0 & 0 \\ 0 & 0 & 0 \\ 0 & 0 & 1 \end{bmatrix}, R = \begin{bmatrix} 5 & 0 \\ 0 & 5 \end{bmatrix}$$

$$\text{UKF: } Q = \begin{bmatrix} 0 & 0 & 0 \\ 0 & 0 & 0 \\ 0 & 0 & 1 \end{bmatrix}, R = \begin{bmatrix} 1 & 0 \\ 0 & 1 \end{bmatrix}$$

The resulting estimation results is presented in Figure. 7-5.

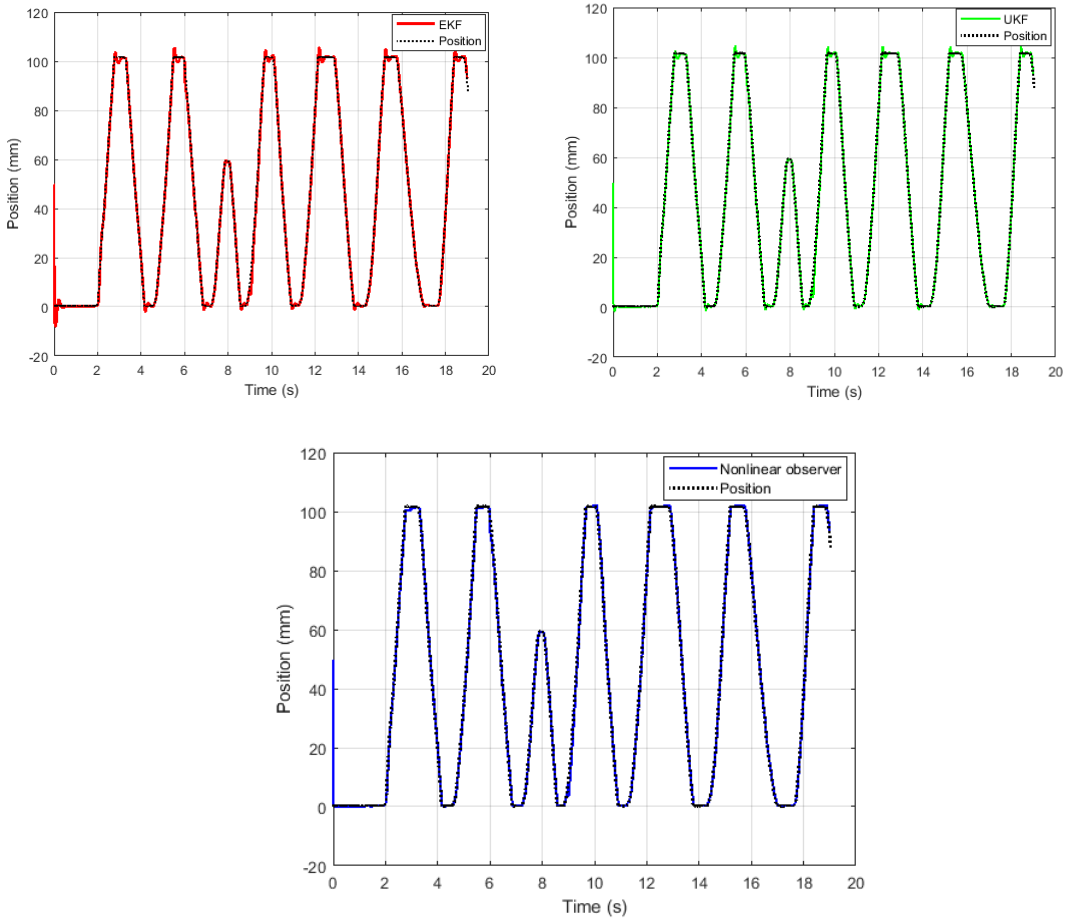

Figure. 7-5. Performance of EKF, UKF, and Observer in presence of pulse disturbances

The estimation error for each estimation technique is presented in Figure. 7-6. The summary of the estimation errors can be seen in Table. 7-2.

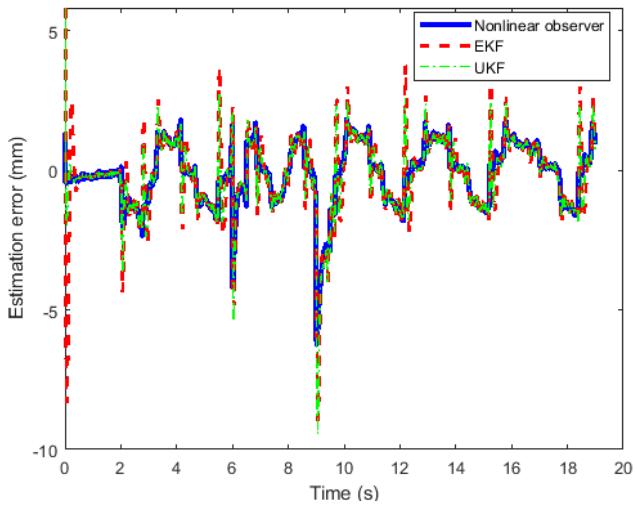

Figure. 7-6. Position estimation error for observer, EKF, and UKF in presence of pulse disturbances

Table. 7-2. Position estimation error for observer, EKF, and UKF in presence of pulse disturbances

Estimation method	Max error (mm)	rms error (mm)
Observer	6.45	1.12
UKF	9.73	1.49
EKF	9.27	1.70

As it can be seen from this table, the observer vastly outperforms EKF and UKF in respect to maximum and rms of the estimation error. This clearly shows that when challenged with pulse disturbances, the proposed H_∞ nonlinear observer is more suitable for this system.

Changing covariance matrices for Kalman filters

It can be argued that by changing the covariance matrices R and Q we can alter the result of the estimation in Kalman filters. However, this change presents a trade-off as can be seen in the figures below. By decreasing the R matrix we rely more on the accuracy of the outputs and that will make our estimation more susceptible to the added square disturbance. In other words, the maximum estimation error will increase. By increasing the R matrix, we rely more on the dynamics of the system and that will cause an increase in

estimation error at end of the course of the piston, since the acceleration is assumed to be constant in the model. This will increase the rms error of the estimation. To summarize:

$$R \uparrow \Longrightarrow \max error \downarrow, rms\ error \uparrow$$

EKF: Figure. 7-7 shows the effect of changing R matrix while keeping $Q = \begin{bmatrix} 0 & 0 & 0 \\ 0 & 0 & 0 \\ 0 & 0 & 1 \end{bmatrix}$.

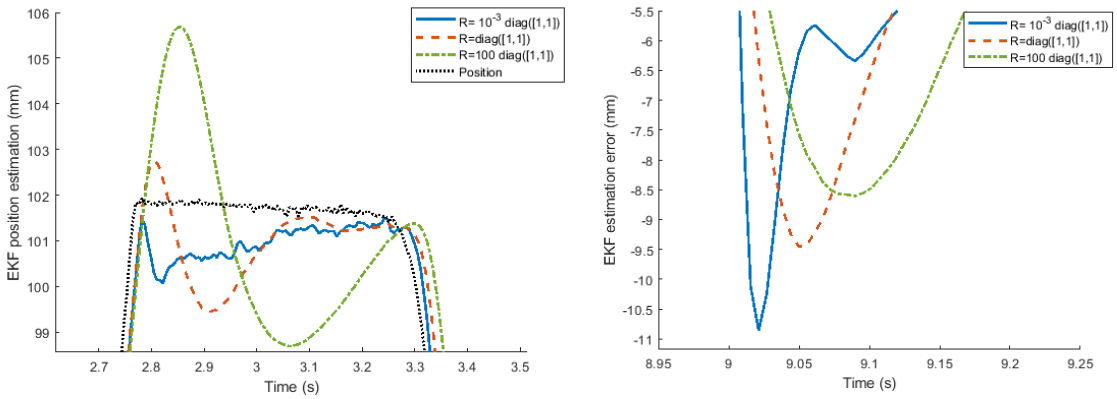

Figure. 7-7. Effect of changing the covariance matrices on EKF

Table. 7-3 summarizes this effect in terms of max and rms error.

Table. 7-3. Effect of changing the covariance matrices on EKF and comparison with observer error

R matrix	Max error (mm)	rms error (mm)
$10^{-3}\begin{bmatrix} 1 & 0 \\ 0 & 1 \end{bmatrix}$	10.85	1.53
$\begin{bmatrix} 1 & 0 \\ 0 & 1 \end{bmatrix}$	9.45	1.63
$100\begin{bmatrix} 1 & 0 \\ 0 & 1 \end{bmatrix}$	8.61	2.11
Observer	6.45	1.12

UKF: The same phenomenon can be seen in the UKF case. Figure. 7-8 and Table. 7-4 show the effect of changing R matrix while keeping $Q = \begin{bmatrix} 0 & 0 & 0 \\ 0 & 0 & 0 \\ 0 & 0 & 1 \end{bmatrix}$.

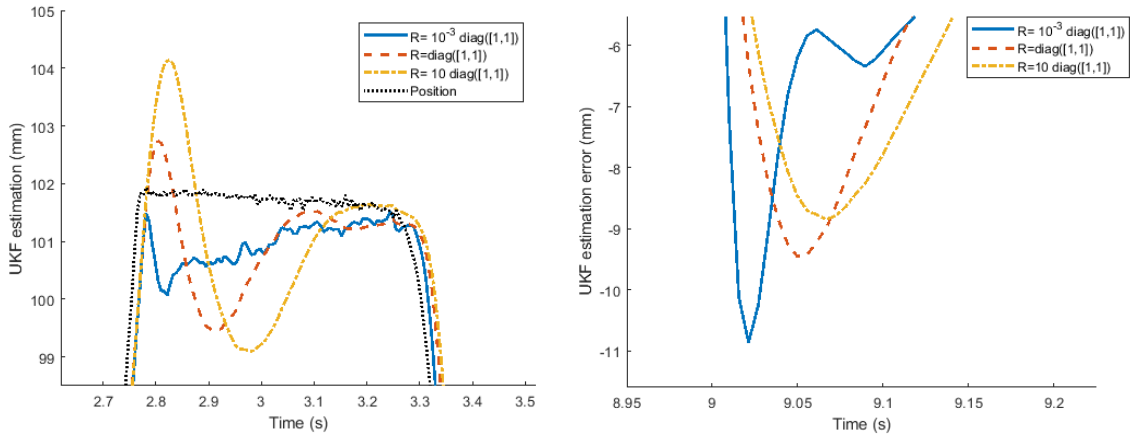

Figure. 7-8. Effect of changing the covariance matrices on UKF

Table. 7-4. Effect of changing the covariance matrices on UKF and comparison with observer error

R matrix	Max error (mm)	rms error (mm)
$10^{-3}\begin{bmatrix}1 & 0\\0 & 1\end{bmatrix}$	11.02	1.41
$\begin{bmatrix}1 & 0\\0 & 1\end{bmatrix}$	9.71	1.48
$10\begin{bmatrix}1 & 0\\0 & 1\end{bmatrix}$	9.14	1.61
Observer	6.45	1.12

7.3.2 Nonlinear Double Capacitor Li-ion Battery Model

Another application that requires the use of nonlinear estimation is state of charge (SoC) estimation in Li-ion batteries. SoC is one of the most important parameters needed in battery management systems for Li-ion batteries that are widely used due to their high energy density [80].

One of the most basic and yet accurate dynamic models for Li-ion batteries is the nonlinear double capacitor equivalent circuit model which is presented in (7.44) [125].

$$x = [V_b, V_s, V_1]^T, A = \begin{bmatrix} -\frac{1}{C_b(R_b+R_s)} & \frac{1}{C_b(R_b+R_s)} & 0 \\ \frac{1}{C_s(R_b+R_s)} & -\frac{1}{C_s(R_b+R_s)} & 0 \\ 0 & 0 & -\frac{1}{R_1C_1} \end{bmatrix}, B = \begin{bmatrix} \frac{R_s}{C_b(R_b+R_s)} \\ \frac{R_b}{C_s(R_b+R_s)} \\ -\frac{1}{C_1} \end{bmatrix} \quad (7.44)$$

$$V_T = f(V_s) + IR_0 - V_1$$

where V_T is the terminal voltage, V_b, V_s, V_1 are the voltages of the inner capacitor network of the battery, R_0 and I are constant resistance and input current respectively, and $f(.)$is a monotonic function given as

$$f(V_s) = 3.2 + 4.69V_s - 20.49V_s^2 + 43.71V_s^3 - 41.50V_s^4 + 14.54V_s^5 \quad (7.45)$$

Also, C_1, C_b, C_s, R_1, R_b, and R_s are the capacitance and resistance of equivalent circuit model of the battery.

As can be seen from (7.44) and (7.45) the dynamic of the system is linear while the only output of the system is nonlinear. Hence, the system dynamics can be written as (7.7), where

$$C = \begin{bmatrix} 0 & 0 & 0 \\ 0 & 0 & 0 \\ 0 & 0 & 1 \end{bmatrix}, J = [0, 1, 0]$$

Furthermore, state of charge of the battery (SoC) can be calculated as:

$$SoC = \frac{C_bV_b + C_sV_s}{C_b + C_s} \quad (7.46)$$

Estimation in the presence of a Gaussian disturbance

The model was simulated by giving a certain current profile as the input. The resulting SoC can be seen in Figure. 7-9 Random Gaussian noise was added to the terminal voltage and current, and since the system in (7.44) is marginally stable $0.1\ A$ of bias was added to the current to make sure of instability.

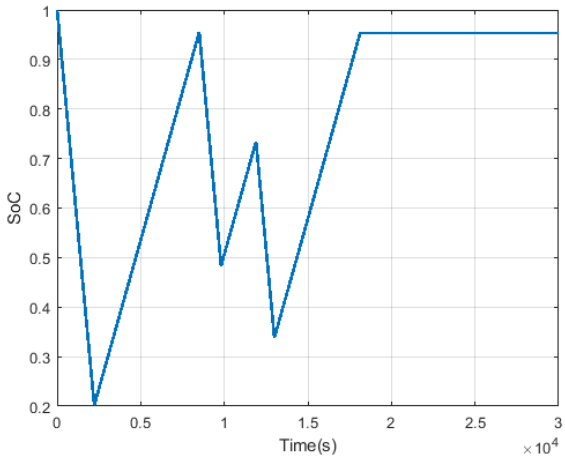

Figure. 7-9. State of charge of the battery

To design the observer, the optimization problem in (7.9) was used while having $\alpha = 0.6$ to make sure of feasibility of constraints. The $B$and D matrices and the resulting observer gain, and the attenuation coefficient was:

$$H_\infty: B = \begin{bmatrix} 0.2 & 0 \\ 2 & 0 \\ 0.01 & 0 \end{bmatrix},\ D = [24 \quad 1.5] \ \Rightarrow L = 10^{-3}\begin{bmatrix} 8.87 \\ 80.50 \\ 0.41 \end{bmatrix}, \mu = 83.6$$

It is to be noted that since two different disturbances will be added to the input current and voltage output in the next part, the disturbance vector $w = \begin{bmatrix} w_1 \\ w_2 \end{bmatrix}$ will have two elements and consequently B and D matrices have two columns.

The best performance of Kalman filters that could be found were the results of the following covariance matrices:

$$\text{EKF: } Q = \begin{bmatrix} 0.1 & 0 & 0 \\ 0 & 0.2 & 0 \\ 0 & 0 & 10^{-5} \end{bmatrix}, R = 50$$

$$\text{UKF: } Q = 10^{-6}\begin{bmatrix} 1 & 0 & 0 \\ 0 & 8 & 0 \\ 0 & 0 & 1 \times 10^{-4} \end{bmatrix}, R = 1 \times 10^{-4}$$

Initial condition for the simulation and estimation was chosen as:

$$x_0 = [1, 1, 0]^T, \qquad \hat{x}_0 = [0.7, 0.7, 0]^T$$

The resulting estimation error for each estimation technique is presented in Figure. 7-10 and Table. 7-5.

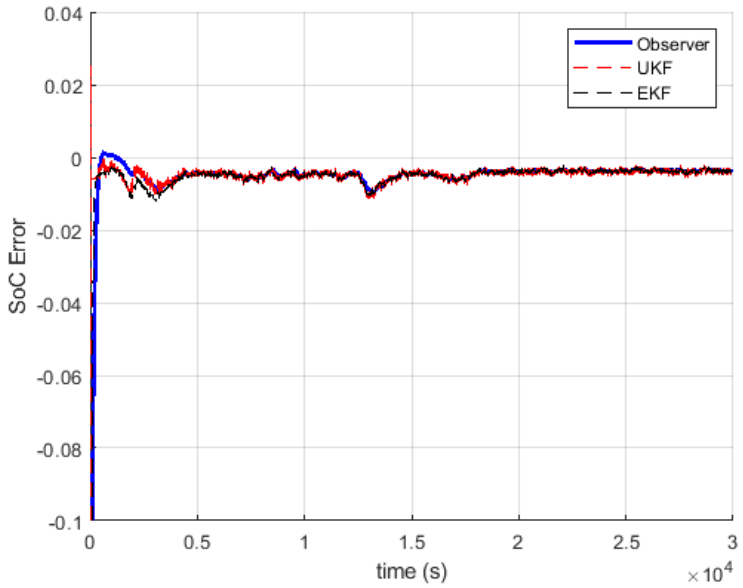

Figure. 7-10. SoC estimation error for observer, EKF, and UKF in presence of Gaussian noise

Table. 7-5. SoC estimation error for observer, EKF, and UKF in presence of Gaussian noise

Estimation method	Max error	rms error
Observer	0.0100	12.4×10^{-3}
UKF	0.0119	6.0×10^{-3}
EKF	0.0122	13.1×10^{-3}

As can be seen from Table. 7-5, the UKF performs somewhat better compared to the nonlinear H_∞observer and EKF.

Adding pulse disturbances

In this section, pulse disturbances to each state and the output voltage as shown in Figure. 7-11.

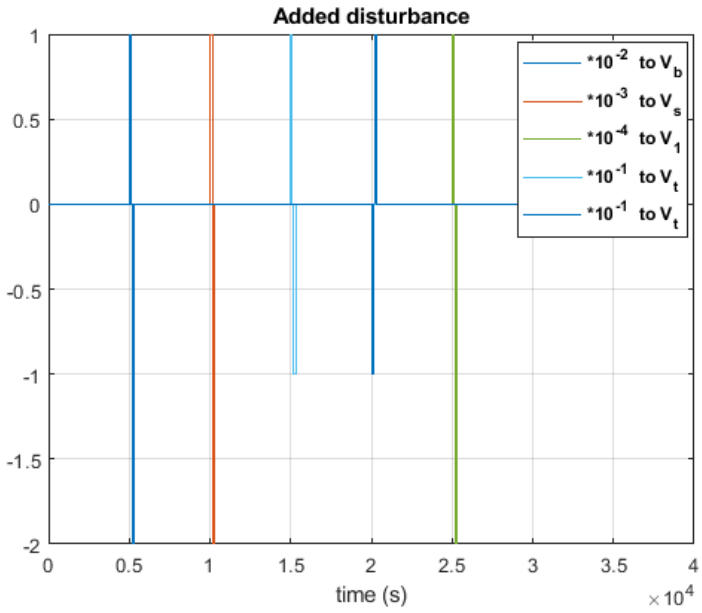

Figure. 7-11. Added pulse disturbances to the battery

The result of estimation is presented in Figure. 7-12 and Table. 7-6.

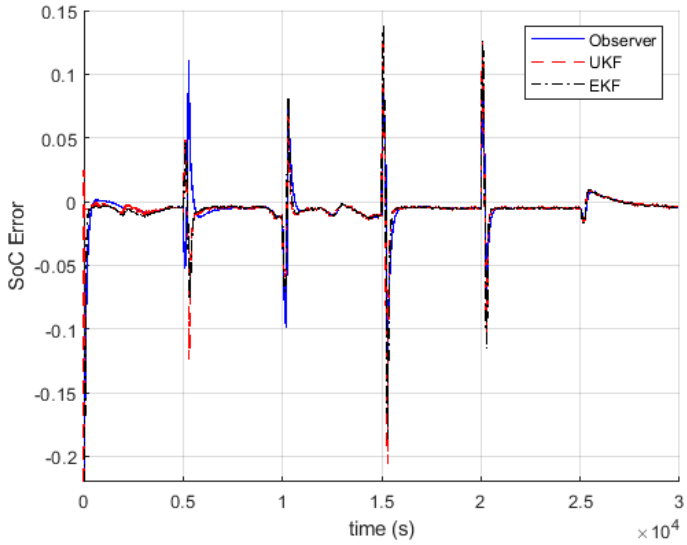

Figure. 7-12. SoC estimation error for observer, EKF, and UKF in presence of pulse disturbances

Table. 7-6. SoC estimation error for observer, EKF, and UKF in presence of pulse disturbances

Estimation method	Max error	rms error
Observer	0.119	19.0×10^{-3}
UKF	0.206	18.5×10^{-3}
EKF	0.187	21.4×10^{-3}

As can be seen from Table. 7-6, although the rms of the estimation error is similar between the three estimation techniques, the H_∞ observer results in a way lower maximum estimation error and can handle the pulse disturbances better.

It is to be mentioned that just like the previous application, the performance of Kalman filters can be improved in the presence of one kind of disturbance, but this comes with the price of terrible performance for the other kind. For example, by picking the following R and Q matrices for UKF:

$$Q = 10^{-8}\begin{bmatrix}1 & 0 & 0\\ 0 & 8 & 0\\ 0 & 0 & 1\times 10^{-4}\end{bmatrix}, R = 5 \times 10^{-3}$$

For the case where only gaussian disturbance exists, the maximum error will drop to 5×10^{-3} and the rms error will reach 4.3×10^{-3}. However, in the presence of pulse disturbances the maximum error and rms error will be respectively 0.248 and 34.2×10^{-3} which shows a considerable increase in estimation error.

Bounds of estimation error for H_∞ nonlinear observer

As was mentioned in Remark 7.3, after the disappearance of initial condition error, the bounds the L_2 norm of the error vector can be pre-calculated based on the bounds of the disturbance signal vector norm or $\|\|w(t)\|_2\|_{\mathcal{L}_\infty}$ using (7.38). In this system, the added disturbance satisfied $\|w(t)\|_2 \leq 0.1$ and by considering the calculated μ the upper bound for the norm of the error vector can be determined. Figure. 7-13 shows the error norm $\|\tilde{x}(t)\|_2$ along with this bound. As can be seen, the error is within the calculated bound. It is to be mentioned that since the magnitudes of the states are not of the same range, this bound is conservative.

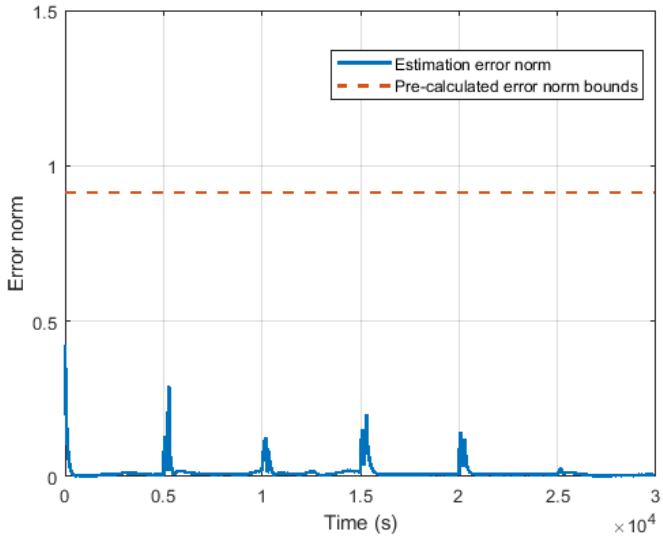

Figure. 7-13. Error norm of the observer estimation along with its pre-calculated bound

7.4 Systems with Nonlinearity in the Dynamic Equations

In this section the problem of vehicle tracking using radar measurements is considered. Similar to last section, first only Gaussian disturbances are added to the system then, pulse disturbances are added to the system already corrupted by Gaussian noise. For each part, performance of the H_∞ nonlinear observer and Kalman filters are compared.

7.4.1 Vehicle Motion Estimation

Using radar sensors, the motion states of a vehicle can be estimated. These radar sensors can be put on-board autonomous vehicles for self-driving purposes [126] or be used for collision prevention [119]. The dynamic model of the system can be presented as:

$$\dot{x} = Ff(Ex) + Bw \tag{7.47}$$

$$y = Cx + Dw$$

where

$$\dot{x} = \begin{bmatrix} \dot{X} \\ \dot{Y} \\ \dot{\psi} \\ \dot{\delta}_f \end{bmatrix} = \begin{bmatrix} V\cos(\psi) \\ V\,sin(\psi) \\ \frac{V}{l_f + l_r}\tan(\delta_f) \\ 0 \end{bmatrix} \tag{7.48}$$

$$C = \begin{bmatrix} 1 & 0 & 0 & 0 \\ 0 & 1 & 0 & 0 \end{bmatrix}$$

and X, Y, ψ, and δ_f are longitudinal position, lateral position, yaw angle of the vehicle, and the steering angle of the front wheels respectively.

The system was simulated by assuming initial condition $x_0 = [0.1, 0.2, 0.3\ , 0.01]^T$. Random Gaussian noise was added to the two position outputs. The resulting trajectory is shown in Figure. 7-14.

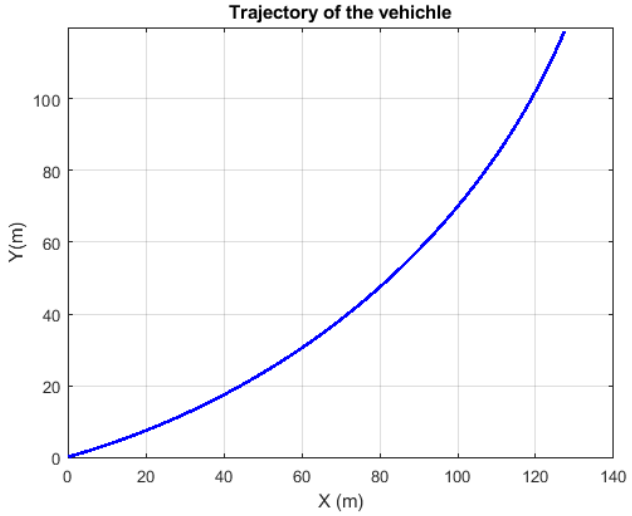

Figure. 7-14. Trajectory of the vehicle

Since the magnitude of states in this system vary considerably, we need to scale the errors:

$$rms\ error = \sqrt{\left(rms\left(\tilde{X}\right)^2 + rms\left(\tilde{Y}\right)^2 + \frac{rms\left(\tilde{\psi}\right)^2}{10^{-2}} + \frac{rms\left(\tilde{\delta_f}\right)^2}{10^{-4}}} \tag{7.49}$$

This parameter will be used to compare the performance of observer and Kalman filters.

Estimation in the presence of Gaussian disturbances

First the performance of estimation methods in presence of only random Gaussian noise

in the outputs is considered. As it will be stated in the next subsection, there is no disturbance in the dynamics in this problem, while pulse disturbances are exerted on each of the outputs. Since the pulse signals are disturbing the outputs at different times, we need to assume that those are two different disturbance signals. We also have IC error, which is practically a large disturbance at $t = 0$. This needs to be considered a separate disturbance by itself. So here $w = \begin{bmatrix} w_1 \\ w_2 \\ w_3 \end{bmatrix}$ and

$$B = 10^{-3}\begin{bmatrix} 0 & 0 & 20 \\ 0 & 0 & 20 \\ 0 & 0 & 0.4 \\ 0 & 0 & 0.1 \end{bmatrix},\ D = \begin{bmatrix} 1 & 0 & 0 \\ 0 & 1 & 0 \end{bmatrix}$$

$$\Delta = \begin{bmatrix} 5 & 0 & 0 & 0 \\ 0 & 5 & 0 & 0 \\ 0 & 0 & 0.2 & 0 \\ 0 & 0 & 0 & 0.04 \end{bmatrix} \Rightarrow L = 10^4 \begin{bmatrix} 4.42 & -5.27 \\ -5.27 & 6.36 \\ -4.32 & 5.18 \\ -0.12 & 0.14 \end{bmatrix}, \mu = 26.9$$

Kalman filters show the best performance with these covariance matrices.

$$\text{EKF:} Q = \begin{bmatrix} 50 & 0 & 0 & 0 \\ 0 & 50 & 0 & 0 \\ 0 & 0 & 20 & 0 \\ 0 & 0 & 0 & 0.5 \end{bmatrix}, R = \begin{bmatrix} 0.1 & 0 \\ 0 & 0.1 \end{bmatrix}, P_0 = \begin{bmatrix} 277.8 & 0 & 0 & 0 \\ 0 & 277.8 & 0 & 0 \\ 0 & 0 & 0.111 & 0 \\ 0 & 0 & 0 & 1.11 \times 10^{-3} \end{bmatrix}$$

$$\text{UKF:} Q = 10^{-7}\begin{bmatrix} 1 & 0 & 0 & 0 \\ 0 & 1 & 0 & 0 \\ 0 & 0 & 0.3 & 0 \\ 0 & 0 & 0 & 1.1 \times 10^{-2} \end{bmatrix}, R = \begin{bmatrix} 0.1 & 0 \\ 0 & 0.1 \end{bmatrix},$$

$$P_0 = \begin{bmatrix} 277.8 & 0 & 0 & 0 \\ 0 & 277.8 & 0 & 0 \\ 0 & 0 & 0.111 & 0 \\ 0 & 0 & 0 & 1.11 \times 10^{-3} \end{bmatrix}$$

The initial condition for estimation was picked as $\hat{x}_0 = [10, 10, 0.7, 0.02]$. The estimation error of yaw angle and steering angle for the observer, EKF, and UKF is shown in Figure. 7-15. Furthermore, the weighted maximum and rms error is presented in Table. 7-7.

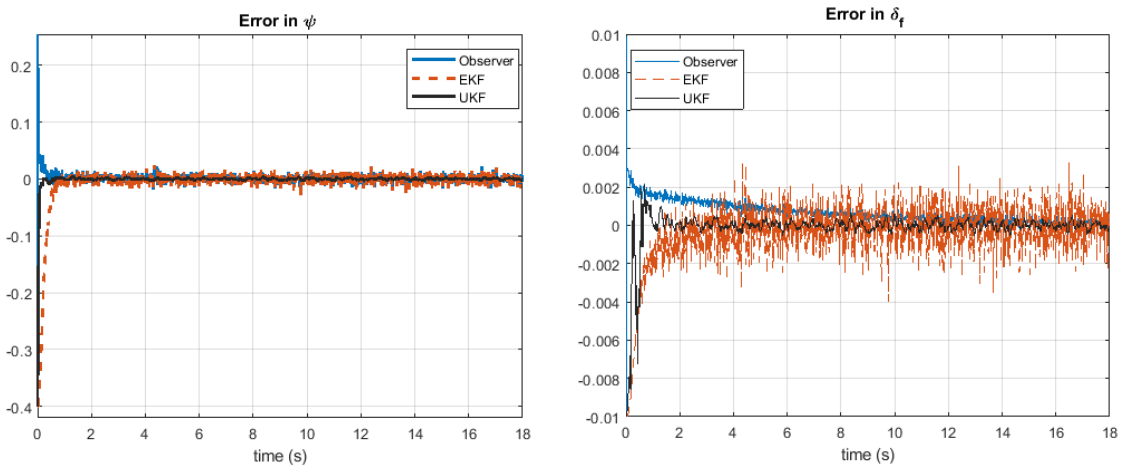

Figure. 7-15. Estimation error of the yaw and steering angles for observer, EKF, and UKF in presence of Gaussian noise

Table. 7-7. Estimation error vector observer, EKF, and UKF in presence of Gaussian noise

Estimation method	Weighted max error	Weighted rms error
Observer	0.927	0.166
UKF	1.475	0.117
EKF	1.611	0.205

where the weighted max error is defined as:

$$Weighted\ \max error = \max_{t>1s} \sqrt{\tilde{X}^2 + \tilde{Y}^2 + \frac{\tilde{\psi}^2}{10^{-2}} + \frac{\tilde{\delta_f}^2}{10^{-4}}} \tag{7.50}$$

As can be seen from Table. 7-7, The observer performs better in respect to the maximum error and UKF outperforms the other two techniques in regard to the weighted rms error.

Estimation in the presence of pulse disturbances in the output

To analyze the effect of the non-Gaussian disturbances on the estimation techniques in this system, a pulse signal is added to the X and Y outputs as shown in Figure. 7-16.

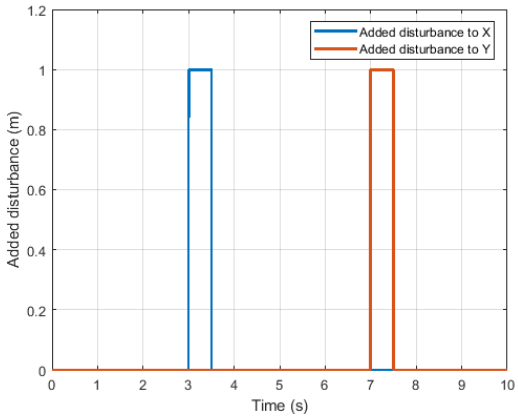

Figure. 7-16. Added pulse disturbances to the radar measurements

Since, as was mentioned before, the magnitude of the states is very different a weighted H_∞ nonlinear observer was utilized (7.25). The weight matrix is picked as $\Delta = \begin{bmatrix} 5 & 0 & 0 & 0 \\ 0 & 5 & 0 & 0 \\ 0 & 0 & 0.2 & 0 \\ 0 & 0 & 0 & 0.04 \end{bmatrix}$.

The estimation error for each state is presented in Figure. 7-17 for the observer, EKF, and UKF.

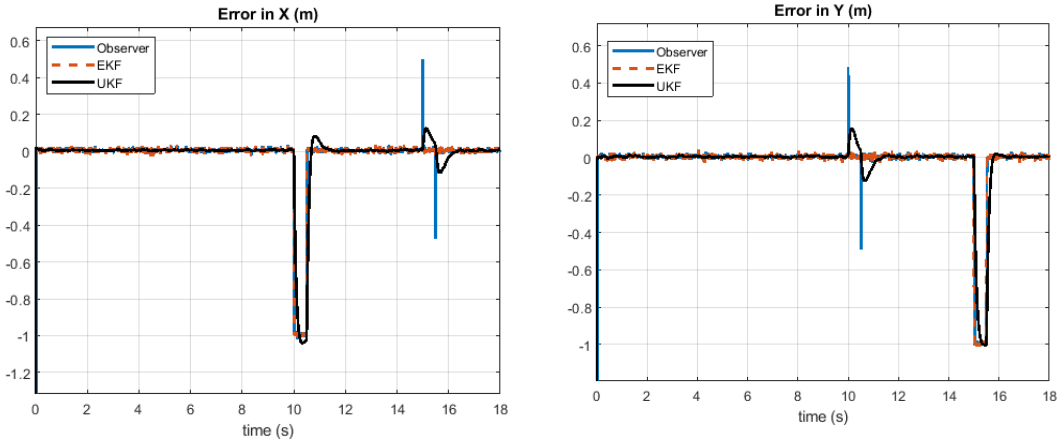

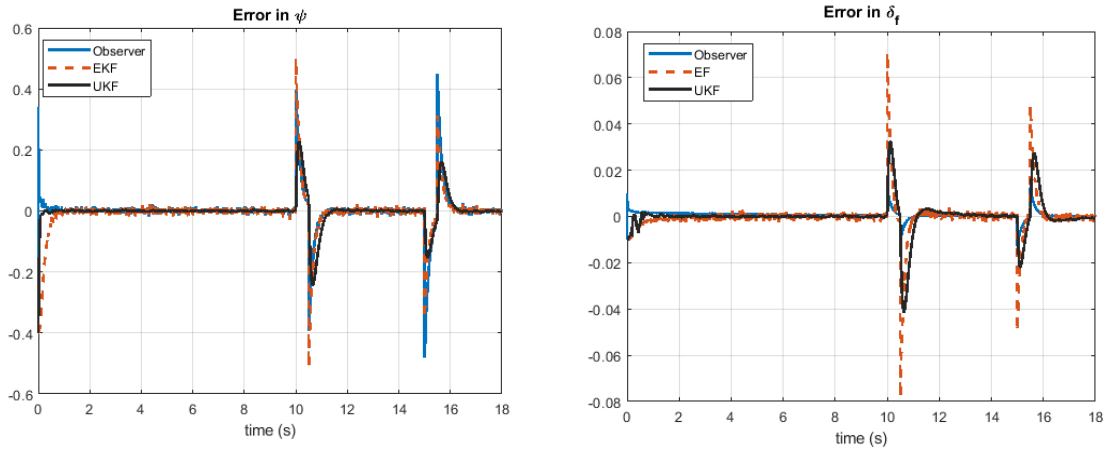

Figure. 7-17. Estimation error of the vehicle motion states for observer, EKF, and UKF in presence of pulse disturbances

The weighted maximum and rms error are also presented in Table. 7-8.

Table. 7-8. Weighted estimation error of the vehicle motion for observer, EKF, and UKF in presence of pulse disturbances

Estimation method	Weighted max error	Weighted rms error
Observer	2.125	0.379
UKF	4.208	0.761
EKF	7.979	0.872

As can be seen from Table. 7-8, the H_∞nonlinear observer vastly outperforms UKF in both criteria while UKF performs better than EKF. The estimation was repeated with a different initial condition for estimators $\hat{x}_0 = [0, 0, 0, 0]$. The result is shown in Table. 7-9 and the same trend is still visible.

Table. 7-9. Estimation error of the vehicle motion states for observer, EKF, and UKF in presence of pulse disturbances with $\hat{x}_0 = [0, 0, 0, 0]$

Estimation method	Weighted max error	Weighted rms error
Observer	2.248	0.362
UKF	4.209	0.765
EKF	8.981	0.873

Estimation error bounds for the nonlinear H_∞ observer

Using the same procedure that resulted in (7.38), the bounds for weighted error norm can be calculated.

$$\|\varepsilon(t)\|_2 \leq \sqrt{\mu}\|w(t)\|_2 = \sqrt{\mu}\,\eta \tag{7.51}$$

Here $\mu = 26.9$ and the added disturbance is bounded by $\eta = 1$. Figure. 7-18 shows the error norm $\|\tilde{\varepsilon}(t)\|_2$ along with this bound.

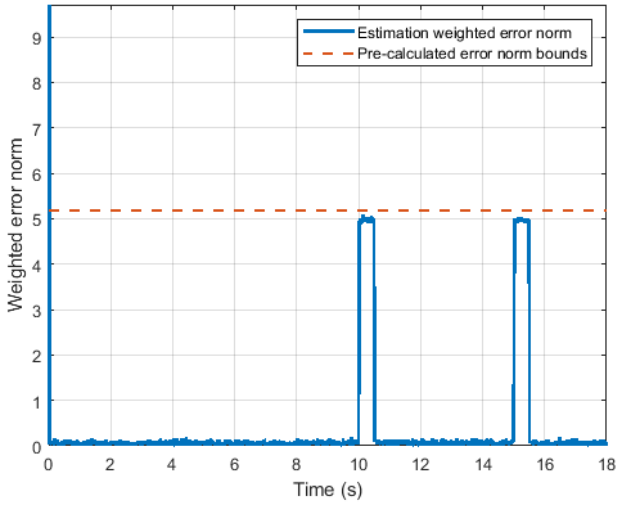

Figure. 7-18. Weighted error norm of the observer estimation along with its pre-calculated bound

As can be seen from Figure. 7-18 the weighted estimation error is within bounds after the disappearance of the initial condition error. The benefit of utilizing weighted observer can be deduced by comparing Figure. 7-18 and Figure. 7-13 (battery application); since the magnitude of elements of the weighted error vector is closer to each other, the calculated bound is less conservative.

7.5 Conclusions

In this chapter, Lyapunov analysis was used to design a H_∞ nonlinear observer and based on this analysis an upper bound on the estimation error vector was obtained. A method was devised to utilize this bound in order to guarantee the stability of observers in disturbed systems that are designed to be stable over a finite domain. Furthermore, the

estimation error of the designed H_∞ nonlinear observer was compared to that of the EKF and the UKF for magnetic position estimation and Li-ion battery SoC estimation. This comparison showed that the H_∞ nonlinear observer is superior when the dynamic systems are corrupted by pulse disturbances.

Additionally, a weighted form of this observer was developed to adjust the estimation performance in case of systems that have states with considerably different magnitudes. This observer was tested on a disturbed vehicle tracking dynamic system and its estimation was shown to be better than that of the EKF and the UKF.

A possible continuation of this work would lead to calculating the bounds of error for each individual state in the system as well as considering dynamic systems with nonmonotonic nonlinearities.

Chapter 8
Conclusions

This dissertation analyzed observer design for non-monotonic nonlinear systems and developed globally stable observer design techniques for such systems. Non-monotonic nonlinear systems are frequently encountered in many practical applications, including vehicle tracking, magnetic position estimation, robotics, state of charge (SoC) estimation in Li-ion batteries, and infectious disease spread dynamics. Very few papers in literature have recognized the special challenge that non-monotonic systems pose to the existing nonlinear observer design methods. This dissertation demonstrated that current LMI-based observer design methods often do not have feasible solutions for many non-monotonic systems. This motivated the need for new observer design techniques. Such techniques were used in three major applications in this thesis: state of charge estimation in Li-ion batteries, magnetic position estimation, and estimation in infectious disease spread dynamics.

First, a class of systems in which the process dynamics and output equations contain nonlinear functions of only scalar arguments was considered. A Lyapunov approach was utilized to develop an LMI-based observer design method for this class of nonlinear systems. Then, the failure of LMI-based methods to provide constant observer gains for non-monotonic systems was rigorously analyzed, and it was demonstrated that, no matter how small the Lipschitz constant or the Jacobian bounds of the involved nonlinear functions, these methods cannot provide a stabilizing constant observer gain if all the functions of the system are non-monotonic. Based on this theoretical result, a hybrid observer technique that switches between multiple constant observer gains was developed

that can provide global asymptotic stability for systems with non-monotonic nonlinear functions. The need for hybrid observers with switched gains becomes important for such non-monotonic systems. The global stability of the hybrid observer was established when there is sufficient dwell time in each locally stable constant gain observer region.

The developed observer design methodology was utilized to estimate the SoC in a lithium-ion battery, using measurements of terminal voltage and bulk force. The challenge in this application was that the bulk force applied to the casing of the battery, as a result of Lithium-ion intercalation and deintercalation, is a non-monotonic function of the SoC. Hence, a switched gain observer was devised and applied. The performance of the observer was evaluated first through simulations using a high-fidelity battery model and then through experiments. The performance of the nonlinear observer was compared with that of an extended Kalman Filter, and its superiority was shown. The nonlinear observer shone when model error was introduced into the system. In the presence of model error in slope change points, the EKF became unstable for even very small errors in the output curves. The nonlinear observer, on the other hand, continued to perform very well, providing accurate estimates and never becoming unstable. The experimental results verified the observations from simulations and the EKF was found to become unstable due to model errors even in the experimental data, while the hybrid nonlinear observer continued to work reliably for this SOC estimation problem.

Position estimation in electro-hydraulic actuators using non-contacting magnetic sensors was another subject that was considered. Magnetic measurements in this application were all non-monotonic, hence based on the theoretical findings of this dissertation it was clear that more than one magnetic sensor was needed for this estimation problem. Subsequently, the minimum singular values of the observability matrix were utilized as a metric for minimizing the number of sensors and optimizing sensor locations. Extensive experimental results were provided to demonstrate the optimality of the sensor locations and the accuracy of the switched gain observer designed for this application.

Next, the hysteresis in Li-ion batteries was analyzed. A nonlinear double capacitor model was used for this problem that contains a measurement equation with two nonlinear functions, one of them being significant hysteresis in voltage of the battery as a function

of the SoC. Previously, researchers in this field used a differential equation to model the hysteresis. In this dissertation, it was shown that this popular method loses observability and a modified Preisach method was suggested as an alternative. The parameters of the modified Preisach model were determined from experimental data using a constrained least square method. Then a nonlinear observer for Lipschitz continuous nonlinear measurement equations was developed using Lyapunov analysis to guarantee global asymptotic stability. The design of the observer gain was based on solving an LMI-convertible inequality over the vertices of the involved convex functions. It was shown that the observer provides accurate SoC estimates based on experimental data in the presence of hysteresis.

Another research application explored in this dissertation was centered around infectious disease spread dynamics and the real-time estimation problem of variables characterizing disease spread. The COVID-19 epidemic was studied for this purpose, and a new nonlinear dynamic model was developed to enhance the traditional SEIR epidemic model to include additional variables. By adding variables on hospitalizations, ICU admissions, and number of deaths, a nonlinear generalized SEIR model was developed. A least-squares method was utilized to find the parameters of the system based on the complete data set of 6-month statistics published by the Minnesota Department of Health. Subsequently, a cascaded observer system, consisting of a bilinear observer and an unknown input observer, was used to estimate the real-time values of the true infected population, the infection rate and the basic reproduction number. The resulting real-time estimates matched well with the least-squares values obtained from the whole data set.

Finally, the use of the nonlinear observer design techniques for handling sensor noise and process disturbances was considered. A H_∞-based globally stable nonlinear observer design technique was explored to provide design flexibility equivalent to the popular locally stable extended Kalman filter which is based on linearization of plant dynamics. Additionally, a weighted form of this observer was developed to adjust the estimation performance in case of systems that have states with considerably different magnitudes. Furthermore, comparing with the performance of the extended and unscented Kalman filters in the presence of non-Gaussian pulse disturbances and through detailed simulations, it was shown that the H_∞ nonlinear observer performs better and can provide a guaranteed

upper bound on the estimation error.

The contributions of this dissertation included showing the non-existence of constant gain LMI-based observers for systems with non-monotonic nonlinear outputs, designing a switched gain globally asymptotically stable nonlinear observer for nonmonotonic systems and utilizing it for Li-ion battery and magnetic position estimation problems. Furthermore, the nonlinear problems of hysteresis modeling and infectious disease spread estimation was tackled and the advantage of H_∞ nonlinear observers compared to Kalman filters in the presence of pulse disturbances was demonstrated.

Bibliography

[1] H. Khalil and J. Ahrens, "High-gain observers in the presence of measurement noise: a switched-gain approach," *Automatica,* vol. 45, no. 4, pp. 936-943, 2009.

[2] A. Zemouche, R. Rajamani, G. Phanomchoeng, B. Boulkroune, H. Rafaralahy and M. Zasadzinski, "Circle Criterion based H-Infinity Observer design for Lipschitz and Monotonic Nonlinear Systems - Enhanced LMI Conditions and Constructive Discussions," *Automatica,* vol. 85, pp. 412-425, Nov 2017.

[3] J.-P. Gauthier and I. A. Kupka, "Observability and observers for nonlinear systems," *SIAM journal on control and optimization,* vol. 32, no. 4, pp. 975-994, 1994.

[4] H. K. Khalil and L. Praly, "High-gain observers in nonlinear feedback control," *International Journal of Robust and Nonlinear Control ,* vol. 24, no. 6, pp. 993-1015, 2014.

[5] H. K. Khalil, "High-gain observers in nonlinear feedback control," in *International conference on control, automation and systems*, 2008.

[6] A. Adil, A. Hamza, I. N'Doye, A. Zemouch, T.-M. Laleg-Kirati and FaziaBedouhe, "On high-gain observer design for nonlinear systems with delayed output measurement," *Automatica,* vol. 141, p. Automatica, 2022.

[7] F. Esfandiari and H. K. Khalil, "Output feedback stabilization of fully linearizable systems," *International Journal of control,* vol. 56, no. 5, pp. 1007-1037, 1992.

[8] R. Rajamani, "Observers for Lipschitz Nonlinear Systems," *IEEE Transactions on Automatic Control,* vol. 43, no. 3, pp. 397-401, 1998.

[9] A. Zemouche and M. Boutayeb, "On LMI conditions to design observers for Lipschitz nonlinear systems," *Automatica,* vol. 49, no. 2, pp. 585-591, 2013.

[10] Y. Wang, R. Rajamani and D. M. Bevly, "Observer Design for Parameter Varying Differentiable Nonlinear Systems, with Application to Slip Angle Estimation," *IEEE Transactions on Automatic Control,* vol. 62, no. 4, pp. 1940-1945, April 2017.

[11] A. Acikmese and M.Corless, "Observers for Systems with Nonlinearities Satisfying an incremental Quadratic Nonlinearity," in *Proceedings of the 2005 American Control Conference*, Portland, Oregon, USA, 2005.

[12] M. Arcak and P. Kokotovic, "Nonlinear Observers: A Circle Criterion Design and Robustness Analysis," *Automatica,* vol. 37, pp. 1923-1930, 2001.

[13] Y. Wang, R. Madson and R. Rajamani, "Nonlinear Observer Design for," in *IEEE Conference on Decision and Control (CDC)*, 2015.

[14] J. L. Crassidis and J. L. Junkins, Optimal estimation of dynamic systems, Chapman and Hall/CRC, 2004.

[15] E. A. Wan and R. V. D. Merwe, "The unscented Kalman filter for nonlinear estimation," in *IEEE 2000 Adaptive Systems for Signal Processing, Communications, and Control Symposium*, 2000.

[16] S. Julier, J. Uhlmann and H. F. Durrant-Whyte, "A new approach for filtering nonlinear systems," *IEEE Transactions on automatic control,* vol. 45, no. 3, pp. 477-482, 2000.

[17] H. K. Khalil, Nonlinear Control, ISBN-13: 978-0-13-349926-1: Pearson Education, 2015.

[18] N. Boizot, E. Busvelle and J. Gauthier, "An adaptive high-gain observer for nonlinear systems," *Automatica,* vol. 46, no. 9, pp. 1483-1488, 2010.

[19] V. Andrieu, L. Praly and A. Astolfi, "High gain observers with updated gain and homogeneous correction terms," *Automatica,* vol. 45, no. 2, pp. 422-428, 2009.

[20] M. Oueder, M. Farza, R. Abdennour and M. M'Saad, "A high gain observer with updated gain for a class of MIMO non-triangular systems," *Systems and Control Letters,* vol. 61, no. 2, pp. 298-308, 2012.

[21] A. Zemouche, F. Zhang, F. Mazenc and R. Rajamani, "High Gain Nonlinear Observer with Lower Tuning Parameter," *IEEE Tranactions on Automatic Control,* p. to appear, August 2019.

[22] H. Khalil, Nonlinear Systems, 3rd ed., Upper Saddle River, New Jersey 07458: Pearson, 2001, p. 768.

[23] S. Boyd, L. Ghaoui, E. Feron and V. Balakrishnan, "Linear Matrix Inequalities in Systems and Control Theory," *Society for Industrial and Applied Mathematics, SIAM Studies in Applied Mathematics,* 1994.

[24] G. Phanomchoeng, R. Rajamani and D. Piyabongkarn, "Nonlinear Observer for Bounded Jacobian Systems, with Applications to Automotive Slip Angle Estimation," *IEEE Transactions on Automotive Control,* vol. 56, no. 5, pp. 1163-1170, May 2011.

[25] R. Goebel, R.G.Sanfelice and A.R.Teel, Hybrid Dynamical Systems - Modeling, Stability, and Robustness, New Jersey: Princeton University Press, 2012.

[26] A. Alessandri and P. Coletta, "Switching Observers for Continuous-Time and Discrete-Time Linear Systems," in *Proceedings of the 2001 American Control Conference*, Arlington, VA, USA, 2001.

[27] A. Alessandri, M. Baglietto and G. Battistelli, "Receding-Horizon Estimation for Switching Discrete-Time Linear Systems," *IEEE Transactions on Automatic Control,* vol. 50, no. 11, pp. 1736-1748, November 2005.

[28] D. Angeli, N. Athanasopoulos, R. Jungers and M. Phileppe, "Path-Complete Graphs and Common Lyapunov Functions," in *Proceedings of the 20th International Conference on Hybrid Systems: Computation and Control*, Pittsburgh, Pennsylvania, USA, 2017.

[29] H. Movahedi, A. Zemouche and R. Rajamani, "Linear Position Estimationon Smart Actuators Using a Nonlinear Observer," in *2019 American Control Conference*, Philadelphia, PA, USA, 2019.

[30] D. Chung, E. Elgqvist and S. Santhanagopalan, "Automotive Lithium-ion Battery Supply Chain and U.S. Competitiveness Considerations," Clean Energy Manufacturing Analysis Center (CEMAC), Golden, CO (United States), 2015.

[31] M. A. Hannan, M. H. Lipu, A. Hussain and A. Mohamed, "A review of lithium-ion battery state of charge estimation and management system in electric vehicle applications: Challenges and recommendations," *Renewable and Sustainable Energy Reviews,* vol. 78, pp. 834-854, 2017.

[32] T. Polóni, M. A. Figueroa-Santos, J. B. Siegel and A. G. Stefanopoulou, "Integration of non-monotonic cell swelling characteristic for state-of-charge estimation," in *American Control Conference (ACC)*, 2018.

[33] Z. Chen, Y. Fu and C. Mi, "State of Charge Estimation of Lithium Ion Batteries in Electric Drive Vehicles Using Extended Kalman Filtering," *Vehicular Technology, IEEE Transactions on,* vol. 62, no. 3, pp. 1020-1030, 2013.

[34] R. Xiong, H. He, F. Sun and K. Zhao, "Evaluation on state of charge estimation of batteries with adaptive extended Kalman filter by experiment approach," *IEEE Transactions on Vehicular Technology,* vol. 62, no. 1, pp. 108-117, 2012.

[35] Y. Wang, H. Fang, L. Zhou and T. Wada, "Revisiting the State-of-Charge Estimation for Lithium-Ion Batteries: A Methodical Investigation of the Extended Kalman Filter Approach," *IEEE Control Systems,* vol. 37, no. 4, pp. 73-96, 2017.

[36] S. Mohan, Y. Kim, J. B. Siegel, N. A. Samad and A. G. Stefanopoulou, "A

phenomenological model of bulk force in a li-ion battery pack and its application to state of charge estimation," *Journal of the Electrochemical Society,* vol. 161, no. 14, p. A2222, 2014.

[37] S. Mohan, Y. Kim and A. G. Stefanopoulou, "On improving battery state of charge estimation using bulk force measurements," in *Dynamic Systems and Control Conference*, 2015.

[38] K.-Y. Oh, J. B. Siegel, L. Secondo, S. U. Kim, N. A. Samad, J. Qin, D. Anderson, K. Garikipati, A. Knobloch, B. I. Epureanu, C. W. Monroe and A. Stefanopoulou, "Rate dependence of swelling in lithium-ion cells," *Journal of Power Sources,* vol. 267, pp. 197-202, 2014.

[39] N. A. Samad, Y. Kim, J. B. Siegel and A. G. Stefanopoulou, "Battery capacity fading estimation using a force-based incremental capacity analysis," *Journal of The Electrochemical Society,* vol. 163, no. 8, p. A1584, 2016.

[40] R. Malik, A. Abdellahi and G. Ceder, "A critical review of the Li insertion mechanisms in LiFePO4 electrodes," *Journal of the electrochemical society,* vol. 160, no. 5, p. A3179, 2013.

[41] X. Hu, S. Li and H. Peng, "A comparative study of equivalent circuit models for Li-ion batteries," *Journal of Power Sources,* vol. 198, pp. 359-367, 2012.

[42] H. E. Perez, J. B. Siegel, X. Lin, A. G. Stefanopoulou, Y. Ding and M. P. Castanier, "Parameterization and validation of an integrated electro-thermal cylindrical lfp battery model," in *Dynamic Systems and Control Conference*, 2012.

[43] C. Zou, C. Manzie and D. Nešić, "Model Predictive Control for Lithium-Ion Battery Optimal Charging," *IEEE/ASME Transactions on Mechatronics,* vol. 23, no. 2, pp. 947-957, 2018.

[44] G. L. Plett, Battery management systems, Volume I: Battery modeling, Artech House, 2015.

[45] "USABC electric vehicle battery test procedures manual, appendix j - detailed

procedure," Report of the United States Council for Automotive Research LLC, 1995.

[46] H. Wang, Y. Huang and A. Khajepour, "Cyber-Physical Control for Energy Management of Off-Road Vehicles with Hybrid Energy Storage Systems," *IEEE/ASME transactions on mechatronics,* vol. 23, no. 6, pp. 2609-2618, 2018.

[47] Y. Wang, R. Madson and R. Rajamani, "Magnetic sensor-based simultaneous state and parameter estimation using a nonlinear observer," *International Journal of Control,* vol. 92, no. 11, pp. 2639-2646, 2019.

[48] P. Colaneri, J. C. Geromel and A. Astolfi, "Stabilization of continuous-time switched nonlinear systems," *Systems & Control Letters,* vol. 57, no. 1, pp. 95-103, 2008.

[49] S. Lee, P. Mohtat, J. B. Siegel and A. G. Stefanopoulou, "Beyond estimating battery state of health: Identifiability of individual electrode capacity and utilization," in *American Control Conference (ACC)*, 2018.

[50] X. Hu, D. Cao and B. Egardt, "Condition Monitoring in Advanced Battery Management Systems: Moving Horizon Estimation Using a Reduced Electrochemical Model," *IEEE/ASME Transactions on Mechatronics,* vol. 23, no. 1, pp. 167-178, 2017.

[51] B. M. Kreutz, "Mediterranean Contributions to the Medieval Mariner's Compass," *Technology and Culture,* vol. 14, no. 3, pp. 367-383, 1973.

[52] B. Allotta, L. Pugi, F. Bartolini, A. Ridolfi, R. Costanzi, N. Monni and J. Gelli, "An Attitude Estimation Algorithm for Mobile Robots Under Unknown Magnetic Disturbances," *Proceedings of the Institution of Mechanical Engineers, Part M: Journal of Engineering for the Maritime Environment,* vol. 229, no. 3, pp. 248-272, 2015.

[53] A. Makni, H. Fourati and A. Y. Kibangou, "Energy-aware adaptive attitude estimation under external acceleration for pedestrian navigation," *IEEE/ASME Transactions On Mechatronics,* vol. 21, no. 3, pp. 1366-1375, 2015.

[54] X. Zhang, M. Mehrtash and M. B. Khamesee, "Dual-axial motion control of a magnetic levitation system using Hall-effect sensors," *IEEE/ASME Transactions on Mechatronics,* vol. 21, no. 2, pp. 1-11, 2016.

[55] D. J. Sadler and C. H. Ahn, "On-chip eddy current sensor for proximity sensing and crack detection," *Sensors and Actuators A: Physical,* vol. 91, no. 3, pp. 340-345, 2001.

[56] R. Madson and R. Rajamani, "Magnetic Position Estimation in Ferromagnetic Systems Involving Significant Hysteresis," *IEEE/ASME Transactions on Mechatronics,* vol. 23, no. 4, pp. 1555-1563, 2018.

[57] A. Zemouche, M. Boutayeb and G. I. Bara, "Observers for a class of Lipschitz systems with extension to H∞ performance analysis," *Systems & Control Letters,* vol. 57, no. 1, pp. 18-27, 2008.

[58] W. Jeon, A. Zemouche and R. Rajamani, "Nonlinear Observer for Vehicle Motion Tracking," in *American Control Conference (ACC)*, 2018.

[59] S. Martínez and F. Bullo, "Optimal sensor placement and motion coordination for target tracking," *Automatica,* vol. 42, no. 4, pp. 661-668, 2006.

[60] C. Papadimitriou, "Optimal sensor placement methodology for parametric identification of structural systems," *Journal of sound and vibration,* vol. 278, no. 4-5, pp. 923-947, 2004.

[61] B. T. Hinson and K. A. Morgansen, "Observability-based optimal sensor placement for flapping airfoil wake estimation," *Journal of Guidance, Control, and Dynamics,* vol. 37, no. 5, pp. 1477-1486, 2014.

[62] A. J. Krener and K. Ide, "Measures of unobservability," in *IEEE Conference on Decision and Control (CDC)*, 2009.

[63] S. P. Chepuri and G. Leus, "Sparsity-promoting sensor selection for non-linear measurement models," *IEEE Transactions on Signal Processing,* vol. 63, no. 3, pp. 684-698, 2014.

[64] D. D. Domenico, A. Stefanopoulou and G. Fiengo, "Lithium-ion battery state of

charge and critical surface charge estimation using an electrochemical model-based extended Kalman filter," *Journal of dynamic systems, measurement, and control,* vol. 132, no. 6, p. 061302, 2010.

[65] K. A. Smith, C. D. Rahn and C.-Y. Wang, "Model-based electrochemical estimation and constraint management for pulse operation of lithium ion batteries," *IEEE Transactions on Control Systems Technology,* vol. 18, no. 3, pp. 654-663, 2009.

[66] A. Bizeray, S. Zhao, S. Duncan and D. Howey, "Lithium-ion battery thermal-electrochemical model-based state estimation using orthogonal collocation and a modified extended Kalman filter," *Journal of Power Sources,* vol. 296, pp. 400-412, 2015.

[67] G. L. Plett, "Sigma-point Kalman filtering for battery management systems of LiPB-based HEV battery packs: Part 2: Simultaneous state and parameter estimation," *Journal of power sources,* vol. 161, no. 2, pp. 1369-1384, 2006.

[68] C. Weng, J. Sun and H. Peng, "A unified open-circuit-voltage model of lithium-ion batteries for state-of-charge estimation and state-of-health monitoring," *Journal of power Sources,* vol. 258, pp. 228-237, 2014.

[69] X. Lin, "Theoretical analysis of battery SOC estimation errors under sensor bias and variance," *IEEE Transactions on Industrial Electronics,* vol. 65, no. 9, pp. 7138-7148, 2018.

[70] J. Meng, D.-I. Stroe, M. Ricco, G. Luo and R. Teodorescu, "A simplified model-based state-of-charge estimation approach for lithium-ion battery with dynamic linear model," *IEEE Transactions on Industrial Electronics,* vol. 66, no. 10, pp. 7717-7727, 2018.

[71] W. Li, F. R. Yue Fan, D. Jöst, X. Han, M. Ouyang and D. U. Sauer, "Electrochemical model-based state estimation for lithium-ion batteries with adaptive unscented Kalman filter," *Journal of Power Sources,* vol. 476, p. 228534, 2020.

[72] S. Dey, B. Ayalew and P. Pisu, "Nonlinear adaptive observer for a lithium-ion battery cell based on coupled electrochemical-thermal model," *Journal of Dynamic Systems, Measurement, and Control,* vol. 137, no. 11, p. 111005, 2015.

[73] D. Zhang, L. D. Couto and S. J. Moura, "Electrode-Level State Estimation in Lithium-Ion Batteries via Kalman Decomposition," *IEEE Control Systems Letters,* vol. 5, no. 5, pp. 1657-1662, 2020.

[74] C. Zhang, Y. Zhang and Y. Li, "A novel battery state-of-health estimation method for hybrid electric vehicles," *IEEE/ASME Transactions On Mechatronics,* vol. 20, no. 5, pp. 2604-2612, 2015.

[75] H. Dreef, H. Beelen and M. Donkers, "LMI-Based Robust Observer Design for Battery State-of-Charge Estimation," in *IEEE Conference on Decision and Control (CDC)*, 2018.

[76] I.-S. Kim, "The novel state of charge estimation method for lithium battery using sliding mode observer," *Journal of Power Sources ,* vol. 163, no. 1, pp. 584-590, 2006.

[77] A. Allam and S. Onori, "An Interconnected Observer for Concurrent Estimation of Bulk and Surface Concentration in the Cathode and Anode of a Lithium-ion Battery," *IEEE Transactions on Industrial Electronics,* vol. 65, no. 9, pp. 7311-7321, 2018.

[78] H. Perez and S. Moura, "Sensitivity-based interval PDE observer for battery SoC estimation," in *American Control Conference (ACC)*, 2015.

[79] R. Klein, N. A. Chaturvedi, J. Christensen, J. Ahmed, R. Findeisen and A. Kojic, "Electrochemical model based observer design for a Lithium-ion battery," *IEEE Transactions on Control Systems Technology,* vol. 21, no. 2, pp. 289-301, 2012.

[80] N. Tian, H. Fang, J. Chen and Y. Wang, "Nonlinear Double-Capacitor Model for Rechargeable Batteries: Modeling, Identification and Validation," IEEE Transactions on Control Systems Technology," *IEEE Transactions on Control Systems Technology,* vol. 29, no. 1, pp. 370-384, 2020.

[81] N. Tian, H. Fang and J. Chen, "A New Nonlinear Double-Capacitor Model for Rechargeable Batteries," in *Annual Conference of the IEEE Industrial Electronics Society*, 2018.

[82] M. Kwak, B. P. J. Lkhagvasuren and J. You, "Parameter identification and SoC estimation of a battery under the hysteresis effect," *IEEE Transactions on Industrial Electronics,* vol. 67, no. 11, pp. 9758-9767, 2019.

[83] I. D. Mayergoyz, Isaak D Mayergoyz, Springer New York, 1991.

[84] H. Banks, A. J. Kurdila and G. Webb, "Identification of hysteretic control influence operators representing smart actuators Part I: Formulation," *Mathematical Problems in Engineering,* vol. 3, 1997.

[85] H. Movahedi, N. Tian, H. Fang and R. Rajamani, "Hysteresis Compensation in State-of-Charge Estimation with a Nonlinear Double-Capacitor Li-Ion Battery Model," in *American Control Conference (ACC)*, 2021.

[86] J. Löfberg, "YALMIP: A toolbox for modeling and optimization in MATLAB," in *the CACSD Conference*, 2004.

[87] D. Simon, Optimal state estimation: Kalman, H infinity, and nonlinear approaches., John Wiley & Sons, 2006.

[88] E. De Wit, N. v. Doremalen, D. Falzarano and V. J. Munster, "SARS and MERS: recent insights into emerging coronaviruses," *Nature Reviews Microbiology,* vol. 14, no. 8, p. pages523–534, 2016.

[89] L. Chen and J. Sun, "Global stability of an SI epidemic model with feedback controls," *Applied Mathematics Letters,* vol. 28, pp. 53-55, 2014.

[90] M. De la Sen, A. Ibeas, S. Alonso-Quesada and R. Nistal, "On a new epidemic model with asymptomatic and dead-infective subpopulations with feedback controls useful for Ebola disease," *Discrete dynamics in Nature and society,* vol. 2017, 2017.

[91] L. Zhong, L. Mu, J. Li, J. Wang, Z. Yin and D. Liu, "Early Prediction of the 2019 Novel Coronavirus Outbreak in the Mainland China Based on Simple

Mathematical Model," *IEEE Access,* vol. 8, pp. 51761-51769, 2020.

[92] H. W. Hethcote and P. V. d. Driessche, "Some epidemiological models with nonlinear incidence," *Journal of Mathematical Biology,* vol. 29, no. 3, pp. 271-287, 1991.

[93] B. Lopman, C. Y. Liu, A. L. Guillou, A. Handel, T. L. Lash, A. P. Isakov and S. M. Jenness, "A modeling study to inform screening and testing interventions for the control of SARS-CoV-2 on university campuses," *Scientific reports,* vol. 11, no. 1, pp. 1-11, 2021.

[94] A. L. Bertozzi, E. Franco, G. Mohler, M. B. Short and D. Sledge, "The challenges of modeling and forecasting the spread of COVID19," *Proceedings of the National Academy of Sciences,* vol. 117, no. 29, pp. 16732-16738, 2020.

[95] G. Stewart, K. Heusden and G. A. Dumont, "How control theory can help us control COVID-19," *IEEE Spectrum,* vol. 57, no. 6, pp. 22-29, 2020.

[96] F. Pazos and F. Felicioni, "A control approach to the Covid-19 disease using a SEIHRD dynamical model," *Medrxiv,* 2020.

[97] J. Dolbeault and G. Turinici, "Heterogeneous social interactions and the COVID-19 lockdown outcome in a multi-group SEIR model," *Mathematical Modelling of Natural Phenomena,* vol. 15, p. 36, 2020.

[98] L. Peng, W. Yang, D. Zhang, C. Zhuge and L. Hong, "Epidemic analysis of COVID-19 in China by dynamical modeling," *arXiv ,* 2020.

[99] "Situation Update for COVID-19," Minnesota Department of Health, 2020. [Online].Available: https://www.health.state.mn.us/diseases/coronavirus/situation.html. [Accessed 09 2020].

[100] J. D'Errico, "fminsearchbnd, fminsearchcon," MATLAB Central File Exchange, 2012.

[101] Z. Yang, Z. Zeng, K. Wang, S.-S. Wong, W. Liang, M. Zanin, P. Liu, X. Cao, Z. Gao, Z. Mai, J. Liang, X. Liu, S. Li, Y. Li, F. Ye, W. Guan, Y. Yang and F.

Li, "Modified SEIR and AI prediction of the epidemics trend of COVID-19 in China under public health interventions," *Journal of Thoracic Disease,* vol. 12, no. 3, p. 165, 2020.

[102] D. Elliott, Bilinear control systems: matrices in action, Springer Science & Business Media, 2009.

[103] D. Ichalal and S. Mammar, "On Unknown Input Observers for LPV Systems," *IEEE Transactions on Industrial Electronics,* vol. 62, no. 9, pp. 5870-5880, 2015.

[104] K. Vijayaraghavan, R. Rajamani and J. Bokor, "Quantitative fault estimation for a class of nonlinear systems," in *American Control Conference*, 2006.

[105] J. Ran, S. Zhao, L. Han, M. Chong, Y. Qiu, Y. Yang, J. Wang, Y. Wu, M. Javanbakht, M. Wang and D. He, "The changing patterns of COVID-19 transmissibility during the social unrest in the United States: A nationwide ecological study with a before-and-after comparison," *One Health,* vol. 12, p. 100201, 2021.

[106] G. Gonsalves and G. Yamey, "Political interference in public health science during covid-19," *bmj,* vol. 371, 2020.

[107] D. Lazer, M. Santillana, R. H. Perlis, K. Ognyanova, M. Baum, J. Druckman, A. Quintana, J. D. Volpe, H. Chwe and M. D. Simonson, "The COVID States Project #10: The pandemic and the protests," OSF Preprints, 2021.

[108] D. Simon, Optimal State Estimation: Kalman, H Infinity, and Nonlinear Approaches, John Wiley & Sons, 2006 .

[109] R. E. Kalman and R. S. Bucy, "New results in linear filtering and prediction theory," *ASME Journal of Basic Engineering,* vol. 83, no. 1, pp. 95-108, 1961.

[110] R. E. Kalman, "A new approach to linear filtering and prediction problems," *ASME Journal of Basic Engineering,* vol. 82, no. 1, pp. 35-45, 1960.

[111] L. Ljung, "Asymptotic behavior of the extended Kalman filter as a parameter estimator for linear systems," *IEEE Transactions on Automatic Control,* vol. 24,

no. 1, pp. 36-50, 1979.

[112] H. Movahedi, N. Tian, H. Fang and R. Rajamani, "Hysteresis compensation and nonlinear observer design for state-of-charge estimation using a nonlinear double-capacitor Li-ion battery model," *IEEE/ASME Transactions on Mechatronics,* vol. 27, no. 1, pp. 594-604, 2021.

[113] H. Movahedi, M. A. Figueroa-Santos, J. B. Siegel, A. G. Stefanopoulou and R. Rajamani, "Hybrid nonlinear observer for battery s tate-of-charge estimation using nonmonotonic force measurements," *Advanced Control for Applications: Engineering and Industrial Systems,* vol. 2, no. 3, p. e38, 2020.

[114] R. Rajamani, "Observers for Lipschitz nonlinear systems," *IEEE transactions on Automatic Control,* vol. 43, no. 3, pp. 397-401, 1998.

[115] K. Zhou and J. C. Doyle, Essentials of robust control, Prentice Hall, 1998.

[116] G. A. Einicke and L. B. White, "Robust extended Kalman filtering," *IEEE Transactions on Signal Processing,* vol. 47, no. 9, pp. 2596-2599, 1999.

[117] W. Lia and Y. Jia, "H-infinity filtering for a class of nonlinear discrete-time systems based on unscented transform," *Signal Processing,* vol. 90, no. 12, pp. 3301-3307, 2010.

[118] A. Zemouche and M. Boutayeb, "A unified H∞ adaptive observer synthesis method for a class of systems with both Lipschitz and monotone nonlinearities," *Systems & Control Letters,* vol. 58, no. 4, pp. 282-288, 2009.

[119] R. Rajamani, W. Jeon, H. Movahed and A. Zemouche, "On the need for switched-gain observers for non-monotonic nonlinear systems," *Automatica,* vol. 114, p. 108814, 2020.

[120] S. Boyd, L. E. Ghaoui, E. Feron and V. Balakrishnan, Linear matrix inequalities in system and control theory, Philadelphia: SIAM, 1994.

[121] H. Movahedi, A. Zemouche and R. Rajamani, "Magnetic position estimation using optimal sensor placement and nonlinear observer for smart actuators," *Control Engineering Practice,* vol. 112, p. 104817, 2021.

[122] K. C. Draa, A. Zemouche, M. Alma, H. Voos and M. Darouach, "A Nonlinear observer-based trajectory tracking method applied to an," *Journal of Process Control,* vol. 75, pp. 120-135, 2019.

[123] R. Madson and R. Rajamani, "Magnetic position estimation in ferromagnetic systems involving significant hysteresis," *IEEE/ASME Transactions on Mechatronics,* vol. 3, no. 4, pp. 1555-1563, 2018.

[124] J. Löfberg, "YALMIP: A toolbox for modeling and optimization in MATLAB," in *IEEE International Symposium on Computer Aided Control System Design*, 2004.

[125] N. Tian, H. Fang, J. Chen and Y. Wang, "Nonlinear Double-Capacitor Model for Rechargeable Batteries: Modeling, Identification, and Validation," *IEEE Transactions on Control Systems Technology,* vol. 29, no. 1, pp. 370-384, 2020.

[126] R. Rajamani, Vehicle dynamics and control, Springer Science & Business Media, 2011.